CAPITAL UNIVERSITY OF SCIENCE AND TECHNOLOGY, ISLAMABAD

A Computational Analysis of Unsteady Radiative Chemical Reactive Hybrid Nanofluid Flow within Porous Media

by

Qandeel Tajamal

A thesis submitted in partial fulfillment for the degree of Master of Philosophy

in the

Faculty of Computing
Department of Mathematics

2026

CERTIFICATE OF APPROVAL

A Computational Analysis of Unsteady Radiative Chemical Reactive Hybrid Nanofluid Flow within Porous Media

by

Qandeel Tajamal

(MMT241008)

THESIS EXAMINING COMMITTEE

(a)	External Examiner	Dr. Tanvir Akbar	CU, Islamabad
(b)	Internal Examiner	Dr. Rashid Ali	CUST, Islamabad

Dr. Muhammad Sagheer
Thesis Supervisor
April, 2026

Dr. Muhammad Sagheer
Head
Dept. of Mathematics
April, 2026

Dr. M. Abdul Qadir
Dean
Faculty of Computing
April, 2026

Author's Declaration

I, **Qandeel Tajamal** hereby state that my M.Phil thesis titled "**A Computational Analysis of Unsteady Radiative Chemical Reactive Hybrid Nanofluid Flow within Porous Media**" is my own work and has not been submitted previously by me for taking any degree from Capital University of Science and Technology, Islamabad or anywhere else in the country/abroad.

At any time if my statement is found to be incorrect even after my graduation, the University has the right to withdraw my M.Phil Degree.

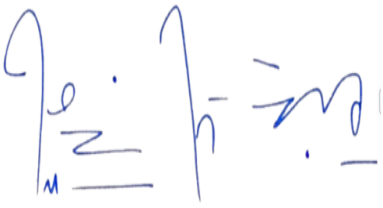

(Qandeel Tajamal)

Registration No: MMT241008

Plagiarism Undertaking

I solemnly declare that research work presented in this thesis titled "A Computational Analysis of Unsteady Radiative Chemical Reactive Hybrid Nanofluid Flow within Porous Media" is solely my research work with no significant contribution from any other person. Small contribution/help whenever taken has been duly acknowledged and that complete thesis has been written by me.

I am aware of Capital University of Science and Technology's and HEC's zero-tolerance policy for plagiarism. As a result, I, the author of the thesis with the same title, hereby declare that no part of my thesis has been copied and that all references have been correctly referenced.I agree that the University reserves the right to withdraw or revoke my M.Phil degree and that HEC and the University may post my name on the website that lists the names of students who have turned in plagiarized work if I am found to have engaged in any formal plagiarism in the thesis mentioned above, even after I have received my degree.

(Qandeel Tajamal)

Registration No: MMT241008

Acknowledgement

In the name of **ALLAH**, the most beneficent and the most merciful, who created the mankind, blessed with intelligence and wisdom to explore the universe and its secrets. Countless respect and love for **Prophet Muhammad (Peace Be Upon Him)**, the fortune of knowledge, who took the humanity out of ignorance and showed the right path. I whole-heartedly dedicate this work to my **Parents Mr. and Mrs. Tajamal Hussain**. I would like to pay great tribute to my beloved **family**, specially my brother **Meraj Tajamal** and respected **teachers** who encouraged and helped me during this work.

Abstract

This thesis numerically investigates the influence of aligned magnetic field, heat generation and chemical reaction of the flow of a hybrid nanofluid past a non linear stretching sheet through a porous medium. The partial differential equations governing the flow problem, are converted to ordinary differential equations by using suitable similarity transformations. The dimensionless equations are then solved numerically with the aid of shooting method. The influence of physical parameters such as magnetic field strength M, porous media effect k_1, angle of inclination γ, suction parameter S, velocity slip parameter L, unsteadiness parameter U_P, thermal radiation parameter N, Prandtl number Pr, heat sink parameter A_1, heat source parameter B_1, Eckert number Ec, activation energy E, Schmidt number Sc, chemical reaction parameter Cr, temperature difference parameter δ on velocity profile, thermal field, concentration distribution, skin friction, Nusselt number and Sherwood number, is studied and presented in graphical and tabular forms.

Contents

List of Figures

List of Tables

Abbreviations

BCs	Boundary conditions
IVPs	Initial value problem
MHD	Magnetohydrodynamics
ODEs	Ordinary differential equation
PDEs	Partial differential equation
RK-4	Range-Kutta order 4
WEG	Water and Ethylene Glycol

Symbols

E_a	Activation energy
k^*	Absorption coefficient
C_∞	Ambient concentration of the hybrid nanofluid
T_∞	Ambient temperature of the nanofluid
Bi	Biot number
K_r	Chemical reaction parameter
σ	Cauchy stress tensor
k_2	Concentration slip parameter
χ	Characteristic length
C_w	Concentration of nanoparticles at the stretching surface
C	Concentration of the fluid
h_f	Convective heat transfer coefficient
f	Dimensionless velocity
θ	Dimensionless temperature
ϕ	Dimensionless concentration
C_r	Dimensionless chemical reaction parameter
ρ_{hnf}	Density of the hybrid nanofluid
$\otimes$	Dyadic tensor
L	Dimensionless velocity slip parameter
ρ_f	Density of the fluid
E	Dimensionless activation energy
ρ_{nf}	Density of the nanofluid
λ	Dimensionless heat source parameter

Ec	Eckert number
σ_{hnf}	Electrical conductivity of the hybrid nanofluid
σ_f	Electrical conductivity of the fluid
$(\rho C_P)_f$	Heat capacitance of fluid
Q_0	Heat source
A_1	Heat sink parameter
B_1	Heat source parameter
$(\rho C_P)_{hnf}$	Heat capacitance of hybrid nanofluid
Q'	Internal heat generation
e	Internal energy
γ	Inclination angle
ν_f	Kinematic viscosity of the fluid
Nu_x	Local Nusselt number
Sh_x	Local Sherwood number
Re_x	Local Reynolds number
τ_w	Local wall shear stress
M	Magnetic field strength
D_B	Mass diffusivity
ϕ	Nanoparticle volume fraction
Nu	Nusselt number
Pr	Prandtl number
k_1	Porous media effect
Re	Reynolds number
q_r	Rosseland radiative heat flux
u_w	Stretching velocity
v_w	Suction velocity
ψ	Stream function
C_f	Skin friction coefficient
Sh	Sherwood number
B_0	Strength of the magnetic field
S	Suction parameter

Sc	Schmidt number
C_P	Specific heat
K	Thermal conductivity
α	Thermal diffisuitivity
T_w	Temperature of the wall
T	Temperature of the fluid
N	Thermal radiation parameter
δ	Temperature difference parameter
K_{hnf}	Thermal conductivity of the hybrid nanofluid
K_f	Thermal conductivity of the fluid
U_P	Unsteadiness parameter
u	Velocity component along x direction
v	Velocity component along y direction
l	Velocity slip parameter
μ_f	Viscosity of the fluid
μ_{nf}	Viscosity of the nanofluid
μ_{hnf}	Viscosity of the hybrid nanofluid

Subscripts

f	Base fluid
nf	Nanofluid
hnf	Hybrid nanofluid

Chapter 1

Introduction

This chapter presents a comprehensive review of research on fluids, nanofluids and hybrid nanofluids, tracing developments from the pioneering work in 1995 to the most recent studies. It highlights the evolution of experimental and numerical investigations on thermal transport, stability and flow characteristics. Both single-component nanofluids and hybrid combinations are discussed, emphasizing enhancements in heat transfer and momentum exchange.

1.1 Historical Background

The efficient transfer of heat plays a vital role in numerous industrial and engineering applications, such as cooling of microelectronic devices, energy systems, heat exchangers and biomedical processes. Commonly used heat transfer fluids, including water, ethylene glycol and engine oil possess inherently poor thermal conductivity which limits their performance in advanced thermal management systems.

To cover this limitation, researchers have explored the development of nanofluids, an emerging class of heat transfer fluids is formed through the uniform dispersion of nanoparticles in a conventional base fluid to increase their thermophysical characteristics.

The concept of nanofluid was first introduced by Choi [1] in 1995, whose work concluded that the addition of nanoparticles with sizes typically ranging 1-100 nm is capable of markedly increasing the thermal conductivity of base fluids. Nanoparticles are commonly utilized due to their high thermal conductivity and stability. When these particles are uniformly dispersed, they enhance energy transport within the fluid through mechanisms like Brownian motion, micro-convection and particle–fluid interactions.

Consequently, nanofluids exhibit superior heat transfer performance, reduced thermal resistance and improved energy efficiency compared to conventional fluids. The study of nanofluids has thus emerged as a key area in modern heat transfer research, offering potential solutions for challenges in thermal systems, electronics cooling and renewable energy applications.

The study of Eastman et al. [2] showed that low thermal conductivity limits the performance of conventional heat transfer fluids. Nanofluids containing dispersed nanocrystalline particles were developed, showing significantly higher thermal conductivities. Adding five percent `CuO` nanoparticles to water enhanced its conductivity by about sixty percent, with excellent suspension stability and minimal particle settling over time. Xuan et al. [3] outlined a method for preparing nanofluids suspensions of nanophase powders in a base liquid and verified their stability via TEM imaging. Using a hot-wire apparatus, the thermal conductivity of nanofluids was analysed, while the effects of particle volume fraction, size, shape and properties were analyzed.

Yang et al. [4] compared the thermal performance of nanofluids with and without additives or surfactants, revealing that suitable additives greatly enhance nanoparticle dispersion stability, resulting in improved thermal conductivity and more uniform heat transfer behavior. It was also observed that an excessive amount of additives can negatively affect viscosity and overall thermal efficiency. Therefore, achieving an optimal balance between nanoparticle type and additive concentration is crucial for maintaining stability and maximizing thermal performance in nanofluid systems. Nanofluids have gained considerable attention as effective

coolants for modern thermal management systems due to their superior heat transfer capabilities.

Tao et al. [5] reviewed recent advancements in this field and highlighted that the enhanced thermal performance of nanofluids stems from improved thermal conductivity, enhanced surface area of nanoparticles and intensified micro-convection effects. The study also emphasized that selecting appropriate nanoparticle materials and optimizing concentration levels are crucial for achieving stable and efficient cooling performance in practical applications [6].

Despite the remarkable thermal improvement offered by nanofluids, researchers have observed that the enhancement may be limited by particle aggregation, sedimentation or saturation effects at higher concentrations. To further improve thermal characteristics, the concept of hybrid nanofluids was proposed.

A hybrid nanofluid is a suspension containing a combination of different nanoparticles dispersed in a base fluid, combining the advantageous properties of each constituent material. For instance, metallic nanoparticles (e.g. Cu and Ag) offer high thermal conductivity, while metal oxide nanoparticles (such as Al_2O_3 and TiO_2) provide better chemical stability and dispersion capability.

The interaction between different nanoparticles in hybrid nanofluids results in enhanced heat transfer, better stability and tunable viscosity compared to mono nanofluids. Consequently, hybrid nanofluids are gaining increasing attention for use in modern thermal systems, including solar collectors, automotive cooling and energy conversion devices.

Zhang et al. [7] experimentally and numerically investigated Al_2O_3-CuO /water hybrid nanofluid flow in a circular tube, showing 2–35 percent enhancement in heat transfer and up to twelve percent rise in pressure drop with higher nanoparticle concentration. CFD models (Eulerian, mixture, DPM) accurately predicted heat transfer, with the Eulerian model showing the best agreement.

Alabdulhadi et al. [8] investigated the effect of hybrid nanoparticles and magnetic fields on mixed convection–driven flow behavior and thermal transport over an

inclined stretching or shrinking surface. An Ag–MgO/water hybrid nanofluid model was solved numerically using the MATLAB bvp4c method after applying similarity transformations.

Results revealed that higher magnetic parameters enhance heat transfer and skin friction while increasing Ag nanoparticle concentration raised skin friction but lowered heat transfer. Dual (non-unique) solutions existed, with only the first being stable based on temporal stability analysis.

Alawi et al. [9] analyzed turbulent flow and heat transfer over a triangularly modulated surface using MWCNT–TiO_2 hybrid nanofluids, validated through ANSYS-FLUENT simulations. Results showed up to a twenty six percent increment in heat transfer with rising nanoparticle concentration, confirming strong thermal performance improvements.

Wohld et al. [10] proposed and validated a thermal conductivity model that works for hybrid nanofluids with any number of distinct nanoparticles, then compared it with experiments and showed good accuracy over various concentrations and temperatures. Alqahtani et al. [11] studied hybrid nanofluids flowing over a stretchable surface in porous media it includes effects like thermal radiation, surface convection and micropolarity. It showed enhanced heat transfer.

Kumar and Shaik [12] focused on Cu-MXene hybrids, examining their stability and thermal conductivity enhancements (e.g., twelve to fourteen percent depending on the volume fraction) using surfactants and other methods. Al Mezrakchi [13] compared several hybrid nanofluids (CuO–ZnO/Water, SiO_2–EG /Water, Al_2O_3–EG/Water, etc.) across different inlet velocities and tube materials. The study demonstrated how the choice of fluid, velocity and material combinations affects both heat transfer and pressure drop. Das et al. [14] surveyed the preparation and stabilization of single and hybrid nanofluids, highlighting their applications, remaining challenges and detailed methodologies such as sonication, the use of surfactants and characterization techniques. The unsteadiness parameter is a dimensionless quantity that characterizes the time-dependent nature of a flow or thermal field. In boundary-layer and stretching-sheet problems, it typically

arises when the surface velocity or external flow varies with time. Physically, an increase in this parameter indicates stronger variations, which can significantly alter momentum and thermal boundary-layer thicknesses. Depending on the system configuration, higher unsteadiness may either enhance or suppress heat and mass transfer rates by modifying velocity gradients and temperature distributions within the fluid domain. Ali et al. [15] analyzed unsteady MHD nanofluid flow over a nonlinear stretching sheet considering temperature dependent viscosity, radiation and thermo diffusion using the Buongiorno model. Numerical results via the finite element method revealed that increasing the viscosity parameter reduces velocity but enhances thermal and concentration profiles.

Sedki et al. [16] investigated unsteady mixed convection nanofluid flow along thermal radiation and heat generation over a permeable surface in a porous medium. The governing equations were solved numerically using the implicit finite difference method, revealing the effects of key parameters such as unsteadiness, radiation, porous medium and heat source on flow and heat transfer, showing strong agreement with previous results. Kumar et al. [17] placed the unsteadiness parameter in the momentum equation and reported that higher unsteadiness reduces surface drag but can increase local heat transfer rates in some parameter range. Abbas et al. [18] included unsteadiness to contrast stretching sheet and cylinder geometries in this comparative study. The authors found that the unsteadiness parameter strongly influences skin friction and heat-transfer rates and its effect depend on the non-Newtonian model used. Naseer et al. [19] using analytic techniques, elaborated that solution existence depends on the unsteadiness parameter (with certain thresholds required) and that film thickness/heat transfer scale predictably with unsteadiness parameter U_P. Diwate et al. [20] quantified how the unsteadiness parameter U_P decreases velocity profiles and heat flux in the boundary layer and provides numerical maps showing where unsteady effects are most impactful.

Hayat et al. in their recent study [21] worked on an unsteadiness parameter in porous, non-Darcy flow models and reported that unsteadiness interacts with Darcy–Forchheimer resistance to alter both velocity and temperature distributions.

Afridi et al. [22] numerically explored entropy generation in unsteady oscillatory nanofluid flow with variable electric conductivity and magnetic heating over an oscillating stretching sheet. Using the Gear–GDQ method, the coupled nonlinear equations were solved, revealing that stronger magnetic and electric conductivity effects reduce velocity but enhance temperature fields. Results showed that parameters e.g. the Eckert number, Strouhal number and nanoparticle volume fraction significantly influence skin friction, Nusselt number and Bejan number offering insights for advanced thermal management system optimization.

The porous media effect refers to the influence of a permeable medium, composed of interconnected voids or pores on the transport of momentum, heat and mass within a fluid. When a fluid passes through a porous structure, flow resistance increases due to resistance at the fluid–solid interface, which is commonly modeled through Darcy or Darcy–Forchheimer laws.

This effect alters velocity profiles, reduces convective heat transfer rates and modifies boundary-layer behavior compared to flows over non-porous surfaces. In nanofluid and hybrid nanofluid systems, the porous medium also impacts nanoparticle motion and energy transport, making permeability a critical parameter in optimizing thermal performance for engineering and energy applications.

The review of [23] pointed out that porous media introduce multi scale transport complexity (pore-scale vs continuum) that complicates classical correlations for Nusselt number. Data driven models are increasingly used to predict porous media nanofluid behaviour because empirical formulas often fail across porosity/permeability ranges.

Nabwey et al. [24] reviewed unsteady porous media studies and highlighted that transient porous flows exhibit qualitatively different boundary-layer responses to time-dependence, with permeability and Forchheimer inertia terms governing whether unsteadiness enhances or damps heat transfer. Numerical results in [25] concluded that increasing porous resistance (lower permeability) suppresses convective cells and reduces overall heat transfer rates, while hybrid nanoparticle mixtures can partially recover thermal performance highlighting porosity as a key

design variable. Venkateswarlu et al. [26] addressing Darcy–Forchheimer porous models for multi-component nanofluids reported that the Forchheimer inertial term becomes important at higher flow rates and can invert trends of heat-transfer enhancement vs. nanoparticle loading compared with pure-Darcy assumptions. Harsha et al. [27] considered Jeffrey nanofluid flowing through a porous medium under mixed convection. They analyzed stability of the flow i.e. how perturbations evolve in a porous setup. This study introduced resistance to flow, dampened velocity changes and modified the Buoyancy effects.

The magnetic field effect refers to the influence of an applied magnetic force on the motion and thermal behavior of electrically conducting fluids, often modeled through the Lorentz force term in magnetohydrodynamics (MHD). When the field is inclined, its orientation relative to the flow direction introduces an additional component of magnetic resistance, modifying velocity, pressure gradients and properties of heat transfer.

The strength and inclination angle of the magnetic field jointly determine how momentum and energy are redistributed within the fluid domain. Khazayinejad et al. [28] found that an inclined magnetic field strongly affects peristaltic pumping and thermal patterns in porous or biomedical channels by introducing cross-stream Lorentz components that reshape velocity and temperature fields. Sarwar et al. [29] reported that increasing inclination reduces axial velocity and thickens thermal boundary layer. The magnetic inclination interacts with variable viscosity to alter skin friction and Nusselt number. Arshad et al. [30] observed that inclination modifies three-dimensional Lorentz components, which strongly affect secondary flows and the combined thermal or radiative transport. Elmhedy et al. [31] explained that inclination modifies pressure-flow relations and can be used to tune thermal transport in inclined conduits useful for biomedical or physiological MHD applications. Adem et al. [32] showed that the field's tilt strongly affects velocity profiles and suction/injection effectiveness. In porous/Darcy flows tilt can either strengthen or weaken mixed convection depending on Hartmann number and permeability. The least amount of energy required for reacting molecules to overcome the energy barrier and form products is called activation energy. It governs the

rate at which a reaction proceeds. In non-dimensional reactive models, it appears in an exponential Arrhenius factor, modulating the reaction rate as a function of temperature. Higher activation energy tends to suppress reaction rates at lower temperatures, while increased temperature reduces the barrier effect and accelerates the reaction. Zafar et al. [33] numerically examined the mixed convective magnetohydrodynamic (MHD) flow of a Prandtl nanofluid influenced by activation energy, chemical reaction and gyrotactic microorganisms.

Ullah et al. [34] analyzed the impact of activation energy and chemical reactions on nanofluid boundary-layer flow over a moving wedge. The governing nonlinear PDEs were transformed into coupled ODEs via similarity based reductions and computed numerical solution using the Keller Box method in MATLAB. Vijaya et al. [35] examined the combined effects of activation energy, chemical reactions, no-slip conditions and radiation on the Maxwell fluid flow over a Riga plate in a porous medium. The governing PDEs were coverted into ODEs via similarity based reductions and solved numerically in MATLAB. Results revealed that higher activation energy and no-slip effects enhanced concentration, while chemical reactions reduced it, offering valuable insights for engineering and industrial heat–mass transfer applications. Nihaal et al. [36] explored heat transfer in hybrid nanofluid flow over a rotating cone and stretching disk system under the effects of a magnetic field, activation energy and non-uniform heat absorption/generation. The governing equations were transformed into ODEs using similarity based reductions and solved via the RKF-45 and shooting methods. Results showed that disk stretching enhances flow and heat transfer, while higher activation energy increases concentration, highlighting the significant influence of hybrid nanoparticles and surface deformation on thermal performance.

1.2 Thesis Contribution

The results of Reddy et al. [37] are reproduced using shooting method. Building on this foundation, the model presented in [37] is extended by considering

unsteady flow, porosity of surface, thermal radiation, inclined magnetic field and concentration dynamics, the scope is expanded to include time-dependent flow effect, porous surface interactions, radiative heat transfer magnetic field influence and enhanced concentration profiling. This synthesis informed a comprehensive extension of the original work. The base fluid water has been changed by mixture of water and ethylene glycol, with CuO and Ag nanoparticles forming the hybrid nanofluid.

The extended model is solved numerically via shooting method, yielding graphical and computational results accurate upto ten decimal places. The impact of unsteadiness, porous media parameter, radiation parameter and magnetic field strength on flow, heat and mass transfer is deeply investigated. The key metrics skin friction, Nusselt number and Sherwood number are quantified to characterize the flow, heat and mass transfer behavior. These results provide valuable insights into the complex interplay of factors influencing hybrid nanofluid dynamics.

1.3 Thesis Structure

Chapter 1 includes a survey of the relevant literature.

Chapter 2 serves as an introduction to the thesis and provides essential definitions and terminologies that are crucial for understanding the concepts discussed in subsequent chapters. This chapter aims to establish a foundational understanding of the key terms and concepts that will be used throughout the thesis.

In Chapter 3, a comprehensive numerical analysis of heat transfer and sensitivity effects in CuO–Ag/H_2O nanofluid radiative flow under hydromagnetic influence over an elongating convectively heated plate using the RSM-CCD model is presented. In Chapter 4, the model discussed in Chapter 3 is extended by considering the impact of porous medium effect in the momentum equation along with other additional effects, such as unsteadiness into the energy equation of the proposed model. Additionally, the unsteady concentration equation of the hybrid nanofluid in the

proposed model is included, considering the chemical reaction effect.

Chapter 5 presents the concluding remarks and highlights the significant findings obtained through the research conducted in this thesis.

The Bibliography section includes a comprehensive list of all the references and sources used in the thesis.

Chapter 2

Preliminaries

In this chapter, the basic laws, core definitions, terminologies and principal concepts required for studying partial differential equations are introduced. They serve as the foundation for understanding the material in the chapters that follow.

2.1 Foundational Concepts

2.1.1 Fluid

A fluid is any material existing in either the liquid or gaseous phase. The distinction between solids and fluids is determined by their capacity to withstand shear (tangential) stress. Solids resist applied shear through a finite deformation, whereas fluids undergo continuous deformation under any level of shear stress. Consequently, in solids, the stress–strain relationship is proportional, while in fluids the stress is directly proportional to the strain rate.

2.1.2 Fluid Dynamics

Fluid dynamics is the discipline concerned with analyzing the transport and motion of liquids, gases and plasma across spatial domains.

2.1.3 Fluid Mechanics

Fluid mechanics refers to the field of study concerned with fluids in the state of rest or during the motion.

2.1.4 Viscosity

Viscosity refers to the fluid's property that opposes the motion of one layer of fluid sliding over another.

If two layers separated by dy move with velocities u and $u + du$, the relative motion produces a shear stress because of viscosity. Each layer exerts an equal and opposite shear stress on the other.

This stress, denoted by τ varies proportionally with the velocity gradient du/dy. Mathematically,

$$\begin{aligned} \tau &\propto \frac{du}{dy}. \\ \Rightarrow \quad \tau &= \mu \frac{du}{dy}. \\ \Rightarrow \quad \mu &= \frac{\tau}{\frac{\partial u}{\partial y}}, \end{aligned} \tag{2.1}$$

where μ represents viscosity coefficient, τ is shear stress and $\frac{\partial u}{\partial y}$ is the velocity gradient or rate of shear strain.

2.1.5 Kinematic Viscosity

Kinematic viscosity is the ratio of a fluid's dynamic viscosity to its density. It is represented by the Greek symbol ν. Mathematically,

$$\nu = \frac{\text{Viscosity}}{\text{Density}} = \frac{\mu}{\rho},$$

where the unit of kinematic viscosity is m^2/s.

2.1.6 Nanofluids

Nanofluids are formed by adding nanoparticles, typically smaller than 100 nm, to traditional heat-transfer fluids like water, oil or ethylene glycol.

When these particles are uniformly and stably suspended, even in small quantities, they can greatly improve the thermal behavior of the host fluid.

2.1.7 Hybrid Nanofluid

Hybrid nanofluids, a recent advancement in nanofluid technology, are formulated by incorporating two or more kinds of nano-particles into a base fluid.

This approach leverages the combined physical and chemical attributes of the distinct nano-particles to achieve superior enhancement of the base fluid properties.

2.1.8 Magnetohydrodynamics

It is the field that examines how magnetic fields, whether applied or generated within the fluid, influence electrically conducting flows.

2.2 Classification of Fluid

There are following types of fluid:

2.2.1 Real Fluid

A real fluid is one that possesses viscosity. In practical scenarios, all known fluids are classified as real fluids.

2.2.2 Ideal Fluid

It is a fluid that is incompressible and possesses no viscosity. Such a fluid is purely hypothetical, as all real fluids exhibit some degree of viscosity.

2.2.3 Ideal Plastic Fluid

A fluid in which the shear stress exceeds a certain yield value and becomes proportional to the shearing strain (or velocity gradient), is termed an ideal plastic fluid. For example, toothpaste and mayonnaise.

2.2.4 Newtonian Fluid

A Newtonian fluid is defined as a fluid in which the applied shear stress maintains a linear proportionality with the velocity gradient or shear strain rate. For example, water and honey.

2.2.5 Non-Newtonian Fluid

A Non-Newtonian fluid is defined as a real fluid for which the relationship between shear stress and the velocity gradient is non-proportional. For example, blood and paints.

2.3 Types of Heat Transfer

2.3.1 Conduction

Conduction can be considered as heat transfer induced by a temperature difference in a stationary solid or fluid. For instance, when one end of a metal rod is placed near a heat source, the heat gradually travels to the other end. In solids, thermal

conduction arises from two key processes:

(*i*) The transport of energy by free electrons.

(*ii*) The transmission of lattice vibrational waves generated by molecular vibrations at their fixed lattice sites.

Lattice is a structured, fixed arrangement of atoms or molecules in a solid. In fluids, conduction can be observed when a still layer of water in contact with a hot container wall gradually becomes warmer.

2.3.2 Convection

Convection is the mechanism of heat transfer that occurs between a solid boundary and a moving fluid due to temperature difference. The fluid temperature used in analysis generally corresponds to its bulk or free-stream temperature.

2.3.3 Forced Convection

Forced convection takes place when devices like fans, pumps or natural wind actively move the fluid across a solid surface.

Since the motion is externally imposed, heat transfer becomes more efficient. With the rise of fluid velocity, the rate of heat transfer typically increases as well.

2.3.4 Free Convection

Natural convection, also called free convection, is the heat transfer mechanism in which fluid flow is driven solely by buoyancy forces that develop due to density variations caused by temperature differences or species concentration gradients in multi-component fluids.

2.3.5 Thermal Radiation

Thermal radiation is the emission of radiant (electromagnetic) energy by a medium, which depends on its temperature.

In some models, this radiant energy is considered to be transported as electromagnetic waves, while in others, it is treated as being carried by particle-like photons.

2.4 Conservation Laws

2.4.1 Law of Conservation of Mass

As per the conservation of mass law, the rate of change of mass within a fixed control volume is equal to the net rate of mass flow across its boundary. This principle can be expressed mathematically in the form of the continuity equation, which ensures mass is conserved in a fluid system. Mathematically,

$$\frac{\partial \rho}{\partial t} + \Delta.(\rho V) = 0, \tag{2.2}$$

where ρ denotes density (kg/m^3) of the medium, V the vector of velocity (ms^{-1}) and Δ denotes the nabla or del operator. The continuity equation (2.2) is in conservation (also known as the divergence form), as it can be directly obtained from the integral representation of mass conservation. By means of the material (or Eulerian) derivative operator $\frac{D}{Dt}$:

$$\frac{D}{Dt} = \frac{\partial}{\partial t} + V.\Delta. \tag{2.3}$$

The continuity equation (2.2) can be represented by the alternate, non-conservation form

$$\frac{\partial \rho}{\partial t} + V.\Delta\rho + \rho\Delta.V = \frac{D\rho}{Dt} + \rho\Delta.V. \tag{2.4}$$

For steady-state condition, the continuity equation becomes:

$$\Delta.\left(\rho V\right)=0. \tag{2.5}$$

When density changes experienced by a fluid particle are insignificant, the incompressible fluid assumption applies and hence $\frac{D\rho}{Dt}$=0. The continuity equation (2.4) turns out:

$$\Delta.V=0. \tag{2.6}$$

It is often identified as the incompressibility constraint governing incompressible flows.

2.4.2 Momentum Equation

According to the the principle of linear momentum conservation, equivalent to Newton's second law, the changing rate of linear momentum of a group of particles is equal to the total external force acting on them, provided that the internal forces satisfy Newton's Third Law. This relationship is expressed as:

$$\frac{\partial}{\partial t}\left(\rho V\right)+\Delta.\left(\rho V\otimes V\right)=\Delta.\sigma+\rho f. \tag{2.7}$$

In this context, $\otimes$ indicates the tensor, also called dyadic, product of two vectors, while σ corresponds to the Cauchy stress tensor (N/m^2) and f is the body force vector, measured per unit mass and normally considered to be the gravity vector.

2.4.3 Law of Conservation of Energy

The law of conservation of energy, also known as the First Law of Thermodynamics, asserts that the rate of variation of the total energy in a system is given by the total of the rates of work performed by external forces and the heat added per unit time.

Generally, the First Law can be expressed in the conservation form as:

$$\frac{\partial \rho e^t}{\partial t} + \Delta.\rho v e^t = -\Delta.q' + \Delta.(\sigma.v) + Q' + \rho f.v, \tag{2.8}$$

where,
$e^t = e + 1/2v.v$ is the total energy (J/m^3), e represents the internal energy, q' is the heat flux vector (W/m^2) and Q' is the internal heat generation (W/m^3).

2.5 Types of Flow

This section presents an overview of various fluid flow types encountered in different contexts during the study of fluid motion.

2.5.1 Compressible Flow

In a compressible flow, the fluid density is variable and differs from point to point within the flow field. Mathematically,

$$\rho \neq k,$$

where k is constant.

2.5.2 Incompressible Flow

In incompressible flow, the fluid maintains a constant density. This property is common for liquids, whereas gases usually experience density changes and are thus compressible. Mathematically,

$$\rho = k,$$

where k is constant.

2.5.3 Rotational Flow

A flow is classified as rotational if the particles not only move along streamlines but also spin around their individual axes.

2.5.4 Irrotational Flow

In irrotational flow, fluid particles follow the streamlines while remaining free of any rotation around their individual axes.

2.5.5 Laminar Flow

Laminar flow is characterized by fluid particles moving along clearly defined, parallel streamlines, forming smooth and regular paths.

2.5.6 Turbulent Flow

In turbulent flow, fluid particles follow unpredictable, swirling trajectories rather than smooth streamlines.

2.5.7 Steady Flow

Steady flow is characterized by fluid properties at a point that remain unchanged over time, including parameters like velocity, pressure, density etc.

Mathematically, we have

$$\frac{\partial \ominus}{\partial t} = 0,$$

where $\ominus$ is any fluid property.

2.5.8 Unsteady Flow

Unsteady flow refers to fluid's motion in which different fluid properties (e.g. velocity, pressure, density etc.) are time-dependent at a specific point. Thus for unsteady flow, mathematically, we have,

$$\frac{\partial \ominus}{\partial t} \neq 0,$$

where $\ominus$ is any fluid property.

2.5.9 Viscous Flow

When the influence of friction within the fluid is considerable, the flow is classified as viscous.

2.5.10 Internal Flow

When a fluid is solely enclosed by solid surfaces, the resulting motion is known as internal or duct flow.

2.5.11 External Flow

Flows that occur around bodies submerged in a large, essentially unbounded fluid are called external flows.

2.6 Dimensionless Numbers

2.6.1 Reynolds Number

This dimensionless number plays a crucial role in identifying different flow behaviors, including whether the flow is laminar or turbulent. Mathematically, it is

represented as:

$$Re = \frac{\chi U}{\nu}.$$

In the above expressions, U denotes the free-stream velocity, χ is the characteristic length scale and ν is the fluid's kinematic viscosity.

2.6.2 Nusselt Number

This quantity describes the relationship between heat transferred by convection and that transferred by conduction at a surface. Mathematically,

$$Nu = \frac{h\chi}{k},$$

where h, χ and k represent convective heat transfer, characteristic length and thermal conductivity, respectively.

2.6.3 Prandtl Number

The dimensionless ratio comparing kinematic viscosity to heat diffusivity within a fluid is termed as Prandtl number. It is denoted by Pr.

Mathematically, it can be written as

$$Pr = \frac{\nu}{\alpha} \quad = \frac{\mu C_P}{\rho k},$$

where μ denotes the momentum diffusivity or kinetic diffusivity and α denotes thermal diffusivity.

2.6.4 Schmidt Number

The dimensionless parameter obtained by dividing the kinematic viscosity ν_f by the molecular diffusivity D_B is defined as Schmidt number Sc.

Mathematically, it can be written as:

$$Sc = \frac{\nu_f}{D_B},$$

where ν_f is the kinematic viscosity and D_B is the mass diffusivity.

2.6.5 Skin Friction Coefficient

The skin friction coefficient is typically defined as:

$$Cf = \frac{\tau_w}{\rho U_w^2},$$

where τ_w, ρ and U_w are the local wall shear stress, fluid density and free stream velocity (usually taken outside the boundary layer or at the inlet).

2.6.6 Sherwood Number

It is a dimensionless parameter that expresses the ratio of mass transported by convection to the mass transferred by diffusion. Mathematically expressed as,

$$Sh = \frac{x\chi}{D_B},$$

here χ is the characteristics length, D_B is the mass diffusivity and x is the mass transfer coefficient.

2.6.7 Eckert Number

This dimensionless number, which is applied in the study of continuum mechanics, expresses the connection between flow behavior and boundary-layer enthalpy variation, serving as an indicator of heat dissipation. Mathematically,

$$Ec = \frac{U_w^2}{(C_P)_f \delta T}.$$

2.6.8 Biot Number

This dimensionless parameter compares the rate of convective heat transfer from a surface to the rate of conductive heat transfer inside the body. Mathematically,

$$B_i = \alpha(2\pi f \kappa C \rho)^{-1/2},$$

where α is the heat transfer coefficient, f is the frequency, C is the specific heat capacity, ρ is the density and κ is thermal conductivity.

2.6.9 Chemical Reaction Parameter

The parameter Cr represents the non-dimensional rate of a first-order chemical reaction occurring within the fluid. An increase in Cr corresponds to an intensified reactive process, which enhances the decay of species concentration away from the surface.

2.7 Shooting Method

This section is devoted to the illustration of the shooting method, which is a numerical scheme for the computation of the solution of a boundary value problem. The following boundary value problem elaborates how the shooting method operates:

$$\left.\begin{aligned} &M''(x) = M(x)M'(x) + 2M^2(x) \\ &M(0) = 0, \qquad M(H) = G. \end{aligned}\right\} \tag{2.9}$$

The domain of problem is considered as [0, H] and H, G are some real numbers. The following notations are introduced to reduce the order of the above boundary value problem.

$$\left.\begin{aligned} &M = Z_1 \\ &M' = Z_1' = Z_2, \\ &M'' = Z_2'. \end{aligned}\right\}$$

As a result, (2.9) is transformed to the subsequent set of first-order ODEs:

$$Z_1' = Z_2, \qquad Z_1(0) = 0, \tag{2.10}$$

$$Z_2' = Z_1 Z_2 + 2Z_1^2, \qquad Z_2(0) = s, \tag{2.11}$$

where s is the missing initial condition which will be guessed. The above IVP will be numerically solved by the RK-4 method. The missing condition s is to be chosen such that:

$$Z_1(H, s) = G.$$

For convenience, now onward $Z_1(H, s)$ will be denoted by $Z_1(s)$.

Further, $Z_1(s) - G$ is donated by $\phi(s)$, so that

$$\phi(s) = 0. \tag{2.12}$$

The above equation (2.12) can be solved by using any appropriate root-finding technique, e.g.,

Newton's method which has the following iterative formula:

$$s_{n+1} = s_n - \frac{\phi(s_n)}{\left(\frac{\partial \phi(s)}{\partial s}\right)_{s=s_n}},$$

or

$$s_{n+1} = s_n - \frac{Z_1(s_n) - G}{\left(\frac{\partial Z_1(s)}{\partial s}\right)_{s=s_n}}. \tag{2.13}$$

To find $\frac{\partial Z_1(s)}{\partial s}$, the following new notations are introduced:

$$\frac{\partial Z_1}{\partial s} = Z_3, \quad \frac{\partial Z_2}{\partial s} = Z_4. \tag{2.14}$$

By using these notations Newton's iterative scheme, gets the form:

$$s_{n+1} = s_n - \frac{Z_1(s_n) - G}{Z_3(s_n)}. \tag{2.15}$$

Now differentiating the ODEs (2.10) and (2.11) with respect to s, another system of ODEs is obtained, as follows:

$$Z_3' = Z_4, \qquad Z_3(0) = 0, \tag{2.16}$$

$$Z_4' = Z_3 Z_2 + Z_1 Z_4 + 4 Z_1 Z_3, \qquad Z_4(0) = 1. \tag{2.17}$$

Finally, the following IVP is obtained:

$$\begin{aligned} Z_1' &= Z_2, & Z_1(0) &= 0, \\ Z_2' &= Z_1 Z_2 + 2Z_1^2, & Z_2(0) &= t, \\ Z_3' &= Z_4, & Z_3(0) &= 0, \\ Z_4' &= Z_3 Z_2 + Z_1 Z_4 + 4 Z_1 Z_3, & Z_4(0) &= 1. \end{aligned}$$

The above IVP will be solved numerically by using RK-4 method. The stopping criteria is set as,

$$\mid Z_1(s) - G \mid < \epsilon,$$

where $\epsilon > 0$ is sufficiently small positive number.

Chapter 3

A Sensitivity Analysis of Radiative CuO–Ag Nanofluid Flow

3.1 Introduction

In this chapter, the work of Reddy et al. [37] is reviewed. The study investigates fluid flow over a stretching sheet under velocity slip condition, with the sheet subjected to radiative heat. The governing equations, originally in partial differential form, are simplified into ordinary differential equations via similarity transformations.

Numerical results are obtained using the shooting method comprising of the Runge-Kutta method of order 4. Velocity and thermal profiles are depicted graphically for various dimensionless parameters.

Furthermore, computational results for the skin friction coefficient and Nusselt number are also provided. The results and discussion section offers a comprehensive analysis of the findings.

3.2 Mathematical Model

This study focuses on convective heat transfer in a water-based hybrid nanofluid flowing over a stretching sheet subjected to an oblique magnetic field. The magnetic field, with constant strength B_0, is applied at an angle γ to the normal direction. The hybrid nanofluid is considered incompressible, steady and laminar, moving in a two-dimensional space with velocity components u and v along the x and y-axes, respectively. The surface stretching generates the flow, while thermal radiation effects are taken into account through radiative heat transfer. Under these assumptions, the governing equations for fluid motion and heat transfer are expressed by the continuity, momentum and energy equations as follows:

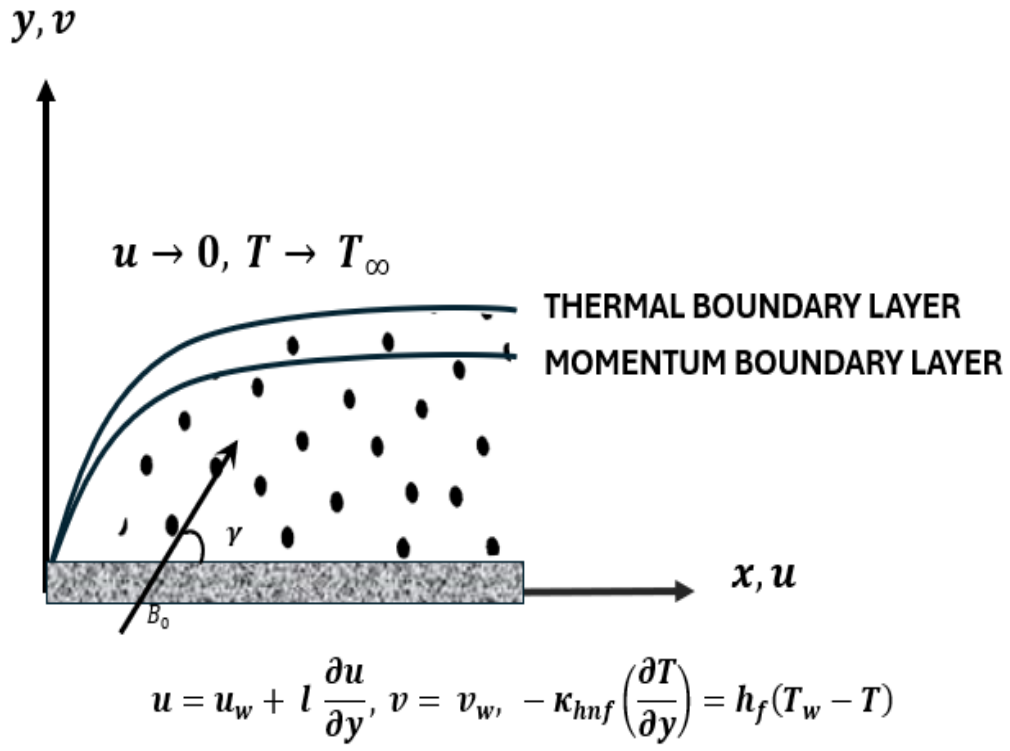

FIGURE 3.1: Geometry of the flow

Continuity Equation:

$$\frac{\partial u}{\partial x} + \frac{\partial v}{\partial y} = 0. \tag{3.1}$$

Momentum Equation:

$$u\frac{\partial u}{\partial x}+v\frac{\partial v}{\partial y}=\frac{\mu_{hnf}}{\rho_{hnf}}\frac{\partial^2 u}{\partial^2 y}-\frac{\sigma_{hnf}}{\rho_{hnf}}B_0^2 u\sin^2\gamma. \tag{3.2}$$

Energy Equation:

$$u\frac{\partial T}{\partial x}+v\frac{\partial T}{\partial y}=\frac{\kappa_{hnf}}{(\rho C_p)_{hnf}}\frac{\partial^2 T}{\partial y^2}-\frac{1}{(\rho C_P)_{hnf}}\frac{\partial q_r}{\partial y}+\frac{Q_0}{(\rho C_P)_{hnf}}\left(T-T_\infty\right). \tag{3.3}$$

Boundary Conditions :

$$\left.\begin{array}{ll}\text{At}\ \ y=0: & u=u_w+l\dfrac{\partial u}{\partial y},\ \ v=v_w,\ \ -\kappa_{hnf}\dfrac{\partial T}{\partial y}=h_f\left(T_w-T\right),\\ \text{As}\ \ y\longrightarrow\infty: & u\longrightarrow 0,\ \ T\longrightarrow T_\infty.\end{array}\right\} \tag{3.4}$$

where l is velocity slip parameter and h_f is the convective heat coefficient.

3.3 Similarity Transformations and Non- dimensionalisation of Mathematical Model

In this section, the mathematical model describing the hybrid nanofluid flow is simplified through non-dimensionalisation.

This involves defining suitable dimensionless variables and parameters that reduce the complexity of the original equations.

By applying these transformations, the equations become easier to analyze while still preserving the key physical effects.

$$u=axf'(\eta),\ \ v=-\sqrt{a\nu_f}f(\eta),\ \ \eta=\sqrt{\frac{a}{\nu_f}}y,\ \ \theta(\eta)=\frac{T-T_\infty}{T_w-T_\infty}. \tag{3.5}$$

The similarity transformations (3.5) used here convert the model into a system of ODEs.

3.3.1 Non-dimensionalisation of Continuity Equation

The derivatives required to satisfy the continuity equation are given as:

$$\begin{aligned}\frac{\partial u}{\partial x} &= \frac{\partial}{\partial x}(axf'(\eta)) \\ &= af'(\eta). \end{aligned} \tag{3.6}$$

$$\begin{aligned}\frac{\partial v}{\partial y} &= \frac{\partial}{\partial y}(-\sqrt{a\nu_f}f(\eta)) \\ &= -\sqrt{a\nu_f}f'(\eta)\frac{\partial \eta}{\partial y} \\ &= -\sqrt{a\nu_f}f'(\eta)\sqrt{\frac{a}{\nu_f}} \\ &= -af'(\eta). \end{aligned} \tag{3.7}$$

Substitution of (3.6) and (3.7) into continuity equation (3.1) implies:

$$af'(\eta) - af'(\eta) = 0,$$

which shows that continuity equation is satisfied identically.

3.3.2 Non-dimensionalisation of Momentum Equation

For momentum equation, the required derivatives are:

$$\begin{aligned}\frac{\partial^2 u}{\partial^2 y} &= \frac{\partial}{\partial y}\left(\frac{\partial u}{\partial y}\right) \\ &= \frac{\partial}{\partial y}\left(ax\sqrt{\frac{a}{\nu_f}}f''\right) \\ &= ax\sqrt{\frac{a}{\nu_f}}f'''\left(\sqrt{\frac{a}{\nu_f}}\right) \\ &= \frac{a^2x}{\nu_f}f'''. \end{aligned}$$

$$\Rightarrow \qquad \frac{\partial^2 u}{\partial^2 y} = \frac{a^2x}{\nu_f}f'''.$$

$$\Rightarrow \qquad \frac{\mu_{hnf}}{\rho_{hnf}}\frac{\partial^2 u}{\partial^2 y} = \frac{\mu_{hnf}}{\rho_{hnf}}\frac{a^2x}{\nu_f}f'''. \tag{3.8}$$

$$\frac{\sigma_{hnf}}{\rho_{hnf}} B_0^2 u \sin^2\gamma = \frac{\sigma_{hnf}}{\rho_{hnf}} B_0^2 a x f' \sin^2\gamma. \tag{3.9}$$

Using equation (3.6) - (3.9) into momentum equation (3.2):

$$a^2 x f'^2 - a^2 x f f'' = \frac{\mu_{hnf}}{\rho_{hnf}} \frac{a^2 x}{\nu_f} f''' - \frac{\sigma_{hnf}}{\rho_{hnf}} B_0^2 a x f' \sin^2\gamma.$$

$$\Rightarrow \quad f f'' - f'^2 + \frac{\mu_{hnf}}{\rho_{hnf}} \frac{f'''}{\nu_f} - \frac{\sigma_{hnf}}{\rho_{hnf}} \frac{B_0^2 f' \sin^2\gamma}{a} = 0.$$

$$\Rightarrow \quad f f'' - f'^2 + \frac{\mu_{hnf}}{\rho_{hnf}} \frac{f'''}{\nu_f} - \frac{\sigma_{hnf}/\sigma_f}{\rho_{hnf}/\rho_f} f' \left(\frac{B_0^2 \sigma_f}{a \rho_f} \right) \sin^2\gamma = 0.$$

$$\Rightarrow \quad f f'' - f'^2 + \frac{\mu_{hnf}}{\rho_{hnf}} \frac{f'''}{\nu_f} - \frac{\sigma_{hnf}/\sigma_f}{\rho_{hnf}/\rho_f} f' M \sin^2\gamma = 0.$$

$$\Rightarrow \quad \frac{\rho_{hnf}}{\rho_f}(f f'' - f'^2) + \frac{\mu_{hnf}}{\rho_f \nu_f} f''' - \frac{\sigma_{hnf}}{\sigma_f} M f' \sin^2\gamma = 0.$$

$$\Rightarrow \quad \frac{\rho_{hnf}}{\rho_f}(f f'' - f'^2) + \frac{\mu_{hnf}}{\mu_f} f''' - \frac{\sigma_{hnf}}{\sigma_f} M f' \sin^2\gamma = 0.$$

$$\Rightarrow \quad f''' + \frac{(\rho_{hnf}/\rho_f)}{(\mu_{hnf}/\mu_f)}(f f'' - f'^2) - \frac{(\sigma_{hnf}/\sigma_f)}{(\mu_{hnf}/\mu_f)} M f' \sin^2\gamma = 0.$$

$$\Rightarrow \quad f''' + \frac{P_1}{P_2}(f f'' - f'^2) - \frac{P_3}{P_2} M f' \sin^2\gamma = 0, \tag{3.10}$$

where $P_1 = \frac{\rho_{hnf}}{\rho_f}$, $P_2 = \frac{\mu_{hnf}}{\mu_f}$ and $P_3 = \frac{\sigma_{hnf}}{\sigma_f}$.

The equation (3.10) represents non-dimensional form of Momentum equation.

3.3.3 Non-dimensionalisation of Energy Equation

The required derivatives for energy equation are:

$$\frac{\partial T}{\partial x} = \frac{\partial}{\partial x}(\theta(\eta)(T_w - T_\infty) + T_\infty) = 0.$$
$$u \frac{\partial T}{\partial x} = 0. \tag{3.11}$$

$$\Rightarrow \quad \frac{\partial T}{\partial y} = (T_w - T_\infty)\theta'(\eta)\frac{\partial \eta}{\partial y}$$
$$= (T_w - T_\infty)\theta' \sqrt{\frac{a}{\nu_f}}.$$

$$\Rightarrow \quad v \frac{\partial T}{\partial y} = -\sqrt{a \nu_f}(T_w - T_\infty) f \theta' \sqrt{\frac{a}{\nu_f}}$$

$$= -a(T_w - T_\infty) f\theta'. \tag{3.12}$$

$$\begin{aligned}\frac{\partial^2 T}{\partial^2 y} &= \frac{\partial}{\partial y}\left((T_w - T_\infty)\theta'(\eta)\sqrt{\frac{a}{\nu_f}}\right)\\ &= (T_w - T_\infty)\sqrt{\frac{a}{\nu_f}}\theta''(\eta)\frac{\partial \eta}{\partial y}\\ &= (T_w - T_\infty)\sqrt{\frac{a}{\nu_f}}\theta''\sqrt{\frac{a}{\nu_f}}\\ &= \frac{a}{\nu_f}(T_w - T_\infty)\theta''. \end{aligned} \tag{3.13}$$

The Rosseland approximation for the radiative heat flux is defined as

$$q_r = \frac{-16\sigma^* T_\infty^3}{3K^*} T_y.$$

$$\Rightarrow \qquad \frac{\partial q_r}{\partial y} = \frac{-16\sigma^* T_\infty^3}{3K^*}\left(\frac{(T_w - T_\infty)a}{\nu_f}\theta''\right). \tag{3.14}$$

$$T - T_\infty = (T_w - T_\infty)\theta. \tag{3.15}$$

Using (3.11) - (3.15) the energy equation (3.3) becomes:

$$-af(T_w - T_\infty)\theta' = \frac{\kappa_{hnf}}{(\rho C_P)_{hnf}}\frac{a(T_w - T_\infty)\theta''}{\nu_f} + \frac{16T_\infty^3\sigma^* a(T_w - T_\infty)\theta''}{3(\rho C_P)_{hnf}K^*\nu_f}.$$

$$+\frac{Q_0(T_w - T_\infty)\theta}{(\rho C_P)_{hnf}}.$$

$$\Rightarrow \qquad \theta''\left(\frac{\kappa_{hnf}}{(\rho C_P)_{hnf}\nu_f} + \frac{16T_\infty^3\sigma^*}{3(\rho C_P)_{hnf}K^*\nu_f}\right) + f\theta' + \frac{Q_0\theta}{a(\rho C_P)_{hnf}} = 0.$$

$$\Rightarrow \qquad \theta''\left(\kappa_{hnf} + \frac{16T_\infty^3\sigma^*}{3K^*}\right) + ((\rho C_P)_{hnf}\nu_f) f\theta' + \frac{Q_0\nu_f\theta}{a} = 0.$$

$$\Rightarrow \qquad \theta''\left(\frac{\kappa_{hnf}}{\kappa_f} + \frac{4T_\infty^3\sigma^*}{3K^*}\kappa_f\right) + \frac{(\rho C_P)_{hnf}\nu_f f\theta'}{\kappa_f} + \frac{Q_0\nu_f\theta}{a\kappa_f} = 0.$$

$$\Rightarrow \qquad \theta''\left(\frac{\kappa_{hnf}}{\kappa_f} + \frac{4}{3}N\right) + \frac{(\rho C_P)_{hnf}\nu_f f\theta'}{\kappa_f} + \frac{Q_0\nu_f\theta}{a\kappa_f} = 0.$$

$$\Rightarrow \qquad \frac{1}{(\rho C_P)_f}\left(\frac{\kappa_{hnf}}{\kappa_f} + \frac{4N}{3}\right)\theta'' + \frac{(\rho C_P)_{hnf}}{(\rho C_P)_f}\frac{\nu_f}{\kappa_f} f\theta' + \left(\frac{Q_0}{a(\rho C_P)_f}\right)\frac{\nu_f\theta}{\kappa_f} = 0.$$

$$\Rightarrow \qquad \frac{1}{(\rho C_P)_f}\left(\frac{\kappa_{hnf}}{\kappa_f} + \frac{4N}{3}\right)\theta'' + \frac{(\rho C_P)_{hnf}}{(\rho C_P)_f}\frac{\nu_f}{\kappa_f} f\theta' + \frac{\nu_f}{\kappa_f}\lambda\theta = 0.$$

$$\Rightarrow \quad \frac{\kappa_f}{\nu_f(\rho C_P)_f}\left(\frac{\kappa_{hnf}}{\kappa_f}+\frac{4N}{3}\right)\theta''+\frac{(\rho C_P)_{hnf}}{(\rho C_P)_f}f\theta'+\lambda\theta=0.$$

$$\Rightarrow \quad \frac{\rho_f\kappa_f}{\mu_f(\rho C_P)_f}\left(\frac{\kappa_{hnf}}{\kappa_f}+\frac{4N}{3}\right)\theta''+\frac{(\rho C_P)_{hnf}}{(\rho C_P)_f}f\theta'+\lambda\theta=0.$$

$$\Rightarrow \quad \frac{1}{Pr}\left(\frac{\kappa_{hnf}}{\kappa_f}+\frac{4N}{3}\right)\theta''+\frac{(\rho C_P)_{hnf}}{(\rho C_P)_f}f\theta'+\lambda\theta=0.$$

$$\Rightarrow \quad \frac{1}{Pr}\left(P_4+\frac{4N}{3}\right)\theta''+P_5 f\theta'+\lambda\theta=0, \tag{3.16}$$

where $P_4=\frac{\kappa_{hnf}}{\kappa_f}$ and $P_5=\frac{(\rho C_P)_{hnf}}{(\rho C_P)_f}$.

The above equation (3.16) represents non-dimensional form of energy equation.

3.3.4 Non-dimensionalisation of Boundary Conditions

- $u=u_w(x)+l\dfrac{\partial u}{\partial y}, \qquad at \quad y=0.$

  $\Rightarrow \quad axf'(\eta)=ax+l\left(axf''(\eta)\sqrt{\dfrac{a}{\nu_f}}\right), \qquad at \quad \eta=0.$

  $\Rightarrow \quad f'(\eta)=1+l\sqrt{\dfrac{a}{\nu_f}}f''(\eta), \qquad at \quad \eta=0.$

  $\Rightarrow \quad f'(\eta)=1+Lf''(\eta), \qquad at \quad \eta=0.$

  $\Rightarrow \quad f'(0)=1+Lf''(0).$

- $-\kappa_{hnf}\left(\dfrac{\partial T}{\partial y}\right)=h_f\left(T_w-T\right), \qquad at \quad y=0.$

  $\Rightarrow \quad -\kappa_{hnf}\left(T_w-T_\infty\right)\theta'(\eta)\sqrt{\dfrac{a}{\nu_f}}=h_f\left(T_w-\left(\theta(\eta)\left(T_w-T_\infty\right)+T_\infty\right)\right), \quad at \quad \eta=0.$

  $\Rightarrow \quad -\kappa_{hnf}\left(T_w-T_\infty\right)\theta'(\eta)\sqrt{\dfrac{a}{\nu_f}}=h_f\left(T_w-T_\infty\right)\left(1-\theta(\eta)\right), \qquad at \quad \eta=0.$

  $\Rightarrow \quad \theta'(\eta)=-\sqrt{\dfrac{\nu_f}{a}}\dfrac{h_f}{\kappa_{hnf}}\left(1-\theta(\eta)\right), \qquad at \quad \eta=0.$

  $\Rightarrow \quad \theta'(\eta)=-\sqrt{\dfrac{\nu_f}{a}}\dfrac{h_f/\kappa_f}{\kappa_{hnf}/\kappa_f}\left(1-\theta(\eta)\right), \qquad at \quad \eta=0.$

$$\Rightarrow \theta'(\eta) = -\frac{1}{\kappa_{hnf}/\kappa_f}\left(\sqrt{\frac{\nu_f}{a}}\frac{h_f}{\kappa_f}\right)(1-\theta(\eta)), \qquad at \quad \eta = 0.$$

$$\Rightarrow \theta'(0) = -\frac{1}{\kappa_{hnf}/\kappa_f} B_i\,(1-\theta(0)).$$

3.3.5 Non-dimensional Elements

This analysis includes non-dimensional parameters like Hartmann number $M = \frac{\sigma_f B_0^2}{a\rho_f}$, Prandtl number $Pr = \frac{\mu_f(\rho_{C-P})_f}{\rho_f \kappa_f}$, the radiation parameter $N = \frac{4\sigma^* T_\infty^3}{K^* \kappa_f}$, the heat source parameter $\lambda = \frac{Q_0}{a(\rho C_P)_f}$, suction parameter $S = -\frac{v_w}{\sqrt{a\nu_f}}$, slip parameter $L = l\sqrt{\frac{a}{\nu_f}}$ and Biot number $B_i = \sqrt{\frac{\nu_f}{a}}\frac{h_f}{\kappa_f}$.

3.4 Relevant Physical Quantities

Two fundamental physical quantities namely, skin friction and the Nusselt number, are of significant importance to engineers during the development of nanoscale systems. These are framed mathematically as below:

3.4.1 Skin Friction

$$C_f = \frac{\mu_{hnf}\left(\frac{\partial u}{\partial y}\right)_{y=0}}{\rho_{hnf}u_w^2} = \frac{\frac{\mu_{hnf}}{\mu_f}\mu_f a x f''(0)\sqrt{\frac{a}{\nu_f}}}{\frac{\rho_{hnf}}{\rho_f}\rho_f a^2 x^2}$$

$$= \frac{\frac{\mu_{hnf}}{\mu_f}\nu_f\sqrt{\frac{a}{\nu_f}}f''(0)}{\frac{\rho_{hnf}}{\rho_f}ax} = \frac{\frac{\mu_{hnf}}{\mu_f}\sqrt{\nu_f}f''(0)}{\frac{\rho_{hnf}}{\rho_f}\sqrt{ax^2}}.$$

$$\Rightarrow C_f\sqrt{\frac{ax^2}{\nu_f}} = \frac{\left(\frac{\mu_{hnf}}{\mu_f}\right)}{\left(\frac{\rho_{hnf}}{\rho_f}\right)}f''(0).$$

$$\Rightarrow C_f\sqrt{\frac{u_w x}{\nu_f}} = \left(\frac{(1-\phi_{CuO})^{-2.5}(1-\phi_{Ag})^{-2.5}}{(1-\phi_{Ag})\left\{(1-\phi_{CuO})+\phi_{CuO}\left(\frac{\rho_{CuO}}{\rho_f}\right)\right\}} + \phi_{Ag}\left(\frac{\rho_{Ag}}{\rho_f}\right)\right)f''(0).$$

$$\Rightarrow C_f\sqrt{Re} = \left(\frac{(1-\phi_{CuO})^{-2.5}(1-\phi_{Ag})^{-2.5}}{(1-\phi_{Ag})\left\{(1-\phi_{CuO})+\phi_{CuO}\left(\frac{\rho_{CuO}}{\rho_f}\right)\right\}}+\phi_{Ag}\left(\frac{\rho_{Ag}}{\rho_f}\right)\right)f''(0).$$

3.4.2 Nusselt Number

$$Nu = \frac{x\left\{\left(-\kappa_{hnf}\frac{\partial T}{\partial y}\right)+q_r\right\}_{y=0}}{\kappa_f(T_w-T_\infty)}.$$

$$\Rightarrow \quad Nu = \frac{-x\left\{\kappa_{hnf}(T_w-T_\infty)\theta'\sqrt{\frac{a}{\nu_f}}+\frac{16\sigma T_\infty^3}{3k^*}(T_w-T_\infty)\theta'\sqrt{\frac{a}{\nu_f}}\right\}}{\kappa_f(T_w-T_\infty)}.$$

$$\Rightarrow \quad Nu = \frac{-x\left\{\kappa_{hnf}\theta'\sqrt{\frac{a}{\nu_f}}+\frac{16\sigma T_\infty^3}{3k^*}\theta'\sqrt{\frac{a}{\nu_f}}\right\}}{\kappa_f}.$$

$$\Rightarrow \quad Nu = \frac{-x\left\{\kappa_{hnf}(\kappa_f/\kappa_f)\theta'\sqrt{\frac{a}{\nu_f}}+\frac{16\sigma T_\infty^3}{3k^*}(\kappa_f/\kappa_f)\theta'\sqrt{\frac{a}{\nu_f}}\right\}}{\kappa_f}.$$

$$\Rightarrow \quad Nu = -x\left\{\frac{\kappa_{hnf}}{\kappa_f}\theta'\sqrt{\frac{a}{\nu_f}}+\frac{16\sigma T_\infty^3}{3k^*\kappa_f}\theta'\sqrt{\frac{a}{\nu_f}}\right\}.$$

$$\Rightarrow \quad Nu = -\left(\frac{\kappa_{hnf}}{\kappa_f}+\frac{4N}{3}\right)\sqrt{\frac{ax^2}{\nu_f}}\theta'(0).$$

$$\Rightarrow \quad Nu\sqrt{\frac{\nu_f}{ax^2}} = -\left(\frac{\kappa_{hnf}}{\kappa_f}+\frac{4}{3}N\right)\theta'(0).$$

$$\Rightarrow \quad \frac{Nu}{\sqrt{Re}} = -\left(\frac{\kappa_{hnf}}{\kappa_f}+\frac{4}{3}N\right)\theta'(0).$$

3.5 Solution Framework

The numerical solutions are determined through the application of the shooting method, employing the fourth-order Runge-Kutta technique for computation of the solution of the initial value problem and Newton's method for refinement of the missing conditions. To tackle the solution of the dimensionless momentum

equation (3.10), the following notations have been adopted as an initial step:

$$f = \tau_1, \qquad f' = \tau_1' = \tau_2, \qquad f'' = \tau_1'' = \tau_2' = \tau_3, \quad f''' = \tau_1''' = \tau_2'' = \tau_3'.$$

The momentum equation is then transformed into the following system of first order ODEs:

$$\tau_1' = \tau_2, \qquad \tau_1(0) = S,$$

$$\tau_2' = \tau_3, \qquad \tau_2(0) = 1{+}LP,$$

$$\tau_3' = \left(\frac{P_1}{P_2}\right)(M\tau_2 \sin^2\gamma) - \left(\frac{P_3}{P_2}\right)(\tau_1\tau_3 - \tau_2^2), \qquad \tau_3(0) = P.$$

The IVP described above will be solved numerically using the fourth-order Runge-Kutta method. The problem domain is assumed to be finite i.e. $[0,\ \eta_\infty]$. The missing condition P is to be chosen such that:

$$\tau_3(\eta_\infty, P) = 0.$$

Newton-Raphson method will be used to update the missing P, using the following iterative scheme:

$$P_{n+1} = P_n - \frac{\tau_3(\eta_\infty, P_n)}{\left(\frac{\partial}{\partial P}\tau_3(\eta_\infty, P)\right)_{P=P_n}}. \tag{3.17}$$

Further, the following notations are introduced :

$$\frac{\partial \tau_1}{\partial P} = \tau_4, \quad \frac{\partial \tau_2}{\partial P} = \tau_5, \quad \frac{\partial \tau_3}{\partial P} = \tau_6.$$

Hence the iterative scheme (3.17) will get the form:

$$P_{n+1} = P_n - \frac{\tau_3(\eta_\infty, P_n)}{\tau_6(\eta_\infty, P_n)}.$$

Now, differentiating the last system of the first order ODEs with respect to P, another system of ODEs will be obtained as follows:

$$\tau_4' = \tau_5, \qquad \tau_4(0) = 0,$$

$$\tau_5' = \tau_6, \qquad \tau_5(0) = L,$$

$$\tau_6' = \left(\frac{P_1}{P_2}\right)(M\tau_5 \sin^2\gamma) - \left(\frac{P_3}{P_2}\right)(\tau_1\tau_6 + \tau_4\tau_3 - 2\tau_2\tau_5), \qquad \tau_6(0) = 1.$$

The stopping criteria for Newton's technique is set as:

$$|\tau_3(\eta_\infty, P)| < \epsilon,$$

where $\epsilon > 0$ is an arbitrarily small positive number. From now onward, ϵ has been taken as 10^{-10}. The ordinary differential equation (3.16) will be approximated by using the shooting technique and assuming f as a known function.

For this, the following notions are utilized:

$$\theta = \zeta_1,\ \theta' = \zeta_1' = \zeta_2.$$

The energy equation is then transformed into the following system of first-order ODEs:

$$\zeta_1' = \zeta_2, \qquad \zeta_1(0) = Q,$$

$$\zeta_2' = \left(\frac{-Pr}{P_4 + \frac{4N}{3}}\right)(P_5\tau_1\zeta_2 + \lambda\zeta_1), \qquad \zeta_2(0) = \left(\frac{B_i}{P_4}\right)(Q - 1).$$

The IVP described above will be solved numerically using the fourth-order Runge-Kutta method. The missing condition Q is to be chosen such that:

$$\zeta_1(\eta_\infty, Q) = 0.$$

The above equation can be solved by using Newton's method with the following iterative formula:

$$Q_{n+1} = Q_n - \frac{\zeta_1(\eta_\infty, Q_n)}{\left(\frac{\partial\zeta_1}{\partial Q}(\eta_\infty, Q)\right)_{Q=Q_n}}. \tag{3.18}$$

The following notations are further introduced:

$$\frac{\partial\zeta_1}{\partial Q} = \zeta_3, \quad \frac{\partial\zeta_2}{\partial d} = \zeta_4.$$

The Newton's iterative scheme (3.18) takes the form:

$$Q_{n+1} = Q_n - \frac{\zeta_1(\eta_\infty, Q_n)}{\zeta_3(\eta_\infty, Q_n)}.$$

Now, differentiating the last system of two first-order ODEs with respect to Q, another system of ODEs is obtained as follows:

$$\zeta_3' = \zeta_4, \qquad \zeta_3(0) = 1,$$

$$\zeta_4' = \left(\frac{-Pr}{P_4 + \frac{4N}{3}}\right)(P_5\tau_1\zeta_4 + \lambda\zeta_3), \qquad \zeta_4(0) = \frac{B_i}{P_4}.$$

The stopping criterion for Newton's method is set as:

$$|\zeta_1(\eta_\infty, Q)| < \epsilon.$$

3.6 Results Interpretation

This section provides a detailed assessment of the velocity and temperature profiles in relation to variations in several governing dimensionless parameters. The investigation is carried out through graphical representations, which illustrate the impacts of parameter variations on the flow and heat transfer characteristics. Furthermore, the effect of these parameters on skin friction and the Nusselt number is systematically examined and summarized in tabular form. The graphical analysis offers a clear visualization of the system's dynamic behavior. By studying the trends, valuable insights into the modifications of velocity and thermal fields under different parameter values, are obtained. The results demonstrate how variations in different parameters govern the overall transport phenomena of the system.

3.6.1 Analysis of Computational Results

The tables 3.1, 3.2 and 3.3 contain numeric values and formulas of different thermophysical properties for base fluid water nanoparticles and hybrid nanoparticles.

The findings in Table 3.4 reveal that an increase in the values of M leads to higher values of local skin friction coefficient, indicating a decrease in the fluid velocity.

A decrease in the values of γ causes an increase in the values of local skin friction coefficient indicating an increase in the fluid velocity. Increasing the values of S shows an increase in values of skin friction, indicating a decrease in the fluid velocity.

TABLE 3.1: Thermophysical characteristics of base fluid H_2O and nanoparticles ϕ_{CuO} and ϕ_{Ag}.

Physical properties	H_2O	CuO	Ag
$\rho/kgm^{-}1$	997	6500	10,500
$C_P/Jkg^{-}1K^{-}1$	4180	525.6	235
$\kappa/Wm^{-}1K^{-}1$	0.6071	20	429
$\sigma/Sm^{-}1$	$5.5 * 10^{-6}$	$5.96 * 10^{7}$	$3.5 * 10^{6}$

TABLE 3.2: Thermophysical characteristics of nanofluid.

Characteristics	Formulation
Heat Capacity	ρ_{nf}=(1-ϕ_{CuO})ρ_f+ϕ_{CuO} ρ_{CuO}
	$(\rho C_P)_{nf}$=(1-ϕ_{CuO})$(\rho C_P)_f$+ϕ_{CuO} $(\rho C_P)_{CuO}$
Dynamic Viscosity	$\mu_{nf}=\frac{\mu_f}{(1-\phi_{CuO})^{2.5}}$
Thermal Conductivity	$\frac{\kappa_{nf}}{\kappa_f} = \left[\frac{\kappa_{CuO}+(n-1)\kappa_f-(n-1)\phi_{CuO}(\kappa_f-\kappa_{CuO})}{\kappa_{CuO}+(n-1)\kappa_f-\phi_{CuO}(\kappa_f-\kappa_{CuO})}\right]$
Electrical Conductivity	$\frac{\sigma_{nf}}{\sigma_f} = \frac{\sigma_f+2\sigma_f-2\phi_{CuO}(\sigma_f-\sigma_f)}{\sigma_f+2\sigma_f+\phi_{CuO}(\sigma_f-\sigma_f)}$

The tables 3.4 and 3.5 present the results of the skin friction coefficient and local Nusselt number for the CuO-Ag/H_2O hybrid nanofluid respectively, considering different inputs of various parameters under consideration. It is noticed that the missing condition P can be chosen from the interval I_s in Table 3.3.

TABLE 3.3: Thermophysical characteristics of hybrid nanofluid.

Characteristics	Formulation
Heat Capacity	ρ_{hnf}=(1-ϕ_{Ag}) [(1-ϕ_{CuO}) ρ_f+ϕ_{CuO} ρ_{CuO}] $+\phi_{Ag}\rho_{Ag}$
	$(\rho C_P)_{hnf}$=(1-ϕ_{Ag})[(1-ϕ_{CuO}) $(\rho C_P)_f$ $+\phi_{CuO}(\rho C_P)_{sCuO}] + \phi_{Ag}(\rho C_P)_{Ag}$
Dynamic Viscosity	$\mu_{hnf}=\frac{\mu_f}{(1-\phi_{CuO})^{2.5}(1-\phi_{Ag})^{2.5}}$
Thermal Conductivity	$\frac{\kappa_{hnf}}{\kappa_{nf}} = \left[\frac{\kappa_{Ag}+(n-1)\kappa_{nf}-(n-1)\phi_{Ag}(\kappa_{nf}-\kappa_{Ag})}{\kappa_{Ag}+(n-1)\kappa_{nf}-\phi_{Ag}(\kappa_{nf}-\kappa_{Ag})}\right]$
Electrical Conductivity	$\frac{\sigma_{hnf}}{\sigma_{nf}} = \frac{\sigma_{Ag}+2\sigma_{nf}-2\phi_{Ag}(\sigma_{nf}-\sigma_{Ag})}{\sigma_{Ag}+2\sigma_{nf}+\phi_{Ag}(\sigma_{nf}-\sigma_{Ag})}$
	$\frac{\sigma_{nf}}{\sigma_f} = \frac{\sigma_{CuO}+2\sigma_f-2\phi_{CuO}(\sigma_f-\sigma_{CuO})}{\sigma_{CuO}+2\sigma_f+\phi_{CuO}(\sigma_f-\sigma_{CuO})}$

An increase in values of L shows a decrease in values of skin friction, resulting in a decrease in the fluid velocity. An increase in the concentration of nanoparticles, ϕ_{CuO} and ϕ_{Ag} shows an increase in values of skin friction resulting an increase in the fluid velocity.

Moreover, the results in Table 3.5 indicate that Nusselt number increases for higher values of Pr and N, reflecting a strong heat transfer. The increase in values of λ results into a decrease in values of Nusselt number indicating an increase in temperature of fluid.

Meanwhile, an increase in values of Biot number shows an increase in values of Nusselt number resulting an increase in temperature of fluid. Furthermore, it is observed that Nusselt number decreases reciprocally with an increase in concentration of nanoparticles ϕ_{CuO} and ϕ_{Ag}.

TABLE 3.4: The results of the skin friction coefficient $C_f\sqrt{Re_x}$ along with the interval I_s for different values of M, γ, S, L, ϕ_{CuO} and ϕ_{Ag}.

M	γ	S	L	ϕ_{CuO}	ϕ_{Ag}	$C_f\sqrt{Re_x}$	I_s
0.1	$\pi/3$	0.1	0.2	0.01	0.01	-0.88355	[-0.9, 3.2]
0.3						-0.93058	[-1.0, 3.0]
0.5						-0.97411	[-1.0, 2.7]
0.7						-1.01468	[-1.1, 2.4]
	$\pi/4$					-0.87534	[-0.9, 3.3]
	$\pi/5$					-0.87020	[-0.9, 3.3]
	$\pi/7$					-0.85856	[-0.9, 3.3]
		0.2				-0.85856	[-1.0, 3.5]
		0.4				-1.00391	[-1.1, 4.0]
		0.6				-1.08964	[-1.2, 4.6]
			0.4			-0.71871	[-0.7, 2.4]
			0.6			-0.60933	[-0.6, 2.0]
			0.8			-0.53073	[-0.5, 1.7]
				0.02		-0.89064	[-0.9, 3.1]
				0.03		-0.89699	[-0.9, 3.0]
				0.04		-0.90426	[-0.9, 3.0]
					0.02	-0.92010	[-0.9, 2.7]
					0.03	-0.95594	[-1.0, 2.4]
					0.04	-0.99119	[-1.0, 2.0]

TABLE 3.5: The results of the local Nusselt number $\frac{Nu_x}{\sqrt{Re_x}}$ for different values of Pr, N, λ, B_i, ϕ_{CuO} and ϕ_{Ag}.

Pr	N	λ	B_i	ϕ_{CuO}	ϕ_{Ag}	$\frac{Nu_x}{\sqrt{Re_x}}$
6.2	0.1	0.2	1	0.01	0.01	0.67599
6.4						0.68250
6.6						0.68876
6.8						0.69479
	0.5					0.86878
	0.7					0.94906
	1.0					1.05263
		0.3				0.63168
		0.4				0.56722
		0.5				0.46027
			2			0.96417
			3			1.12387
			4			1.22535
				0.02		0.67470
				0.03		0.67349
				0.04		0.67235
					0.02	0.67006
					0.03	0.66385
					0.04	0.65733

3.6.2 Velocity Field

Figure 3.2 elaborates the effect of Hartmann number on the velocity profile. Higher values of M lead to a decline in the fluid velocity and compression of the momentum boundary layer. This behavior is attributed to strengthen the applied magnetic field, which enhances the Lorentz force acting as a flow-resisting force acting on the fluid. Figure 3.3 presents the influence of the inclination angle γ of the magnetic field on the velocity profile. It is observed that the fluid velocity increases as γ decreases, indicating that a larger inclination angle enhances the magnetic resistance to the fluid flow.

Thickness of the velocity boundary layer with different values of suction parameter S is described in Figure 3.4. The velocity distribution within the boundary layer is reduced due to gradually increasing values of S, resulting in reduced fluid motion and thinner boundary layer. As a result, the overall velocity distribution across the layer decreases. It is observed in Figure 3.5 that increasing values of velocity slip parameter L shows a decline in the values of fluid flow. This results into velocity boundary layer becoming thinner.

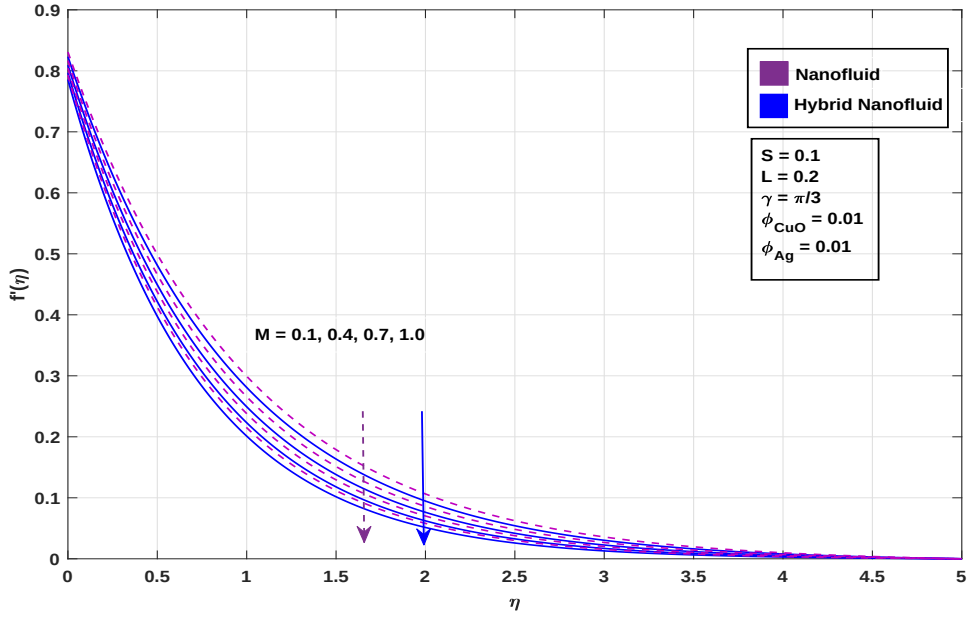

FIGURE 3.2: Impact of M on $f'(\eta)$

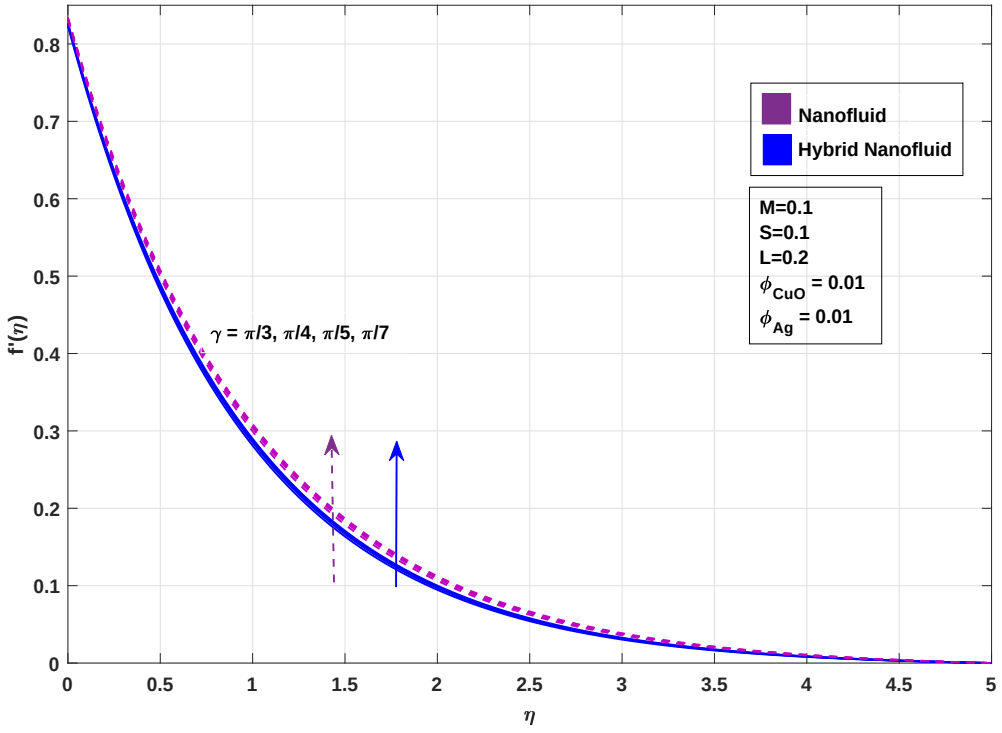

FIGURE 3.3: Impact of γ on $f'(\eta)$

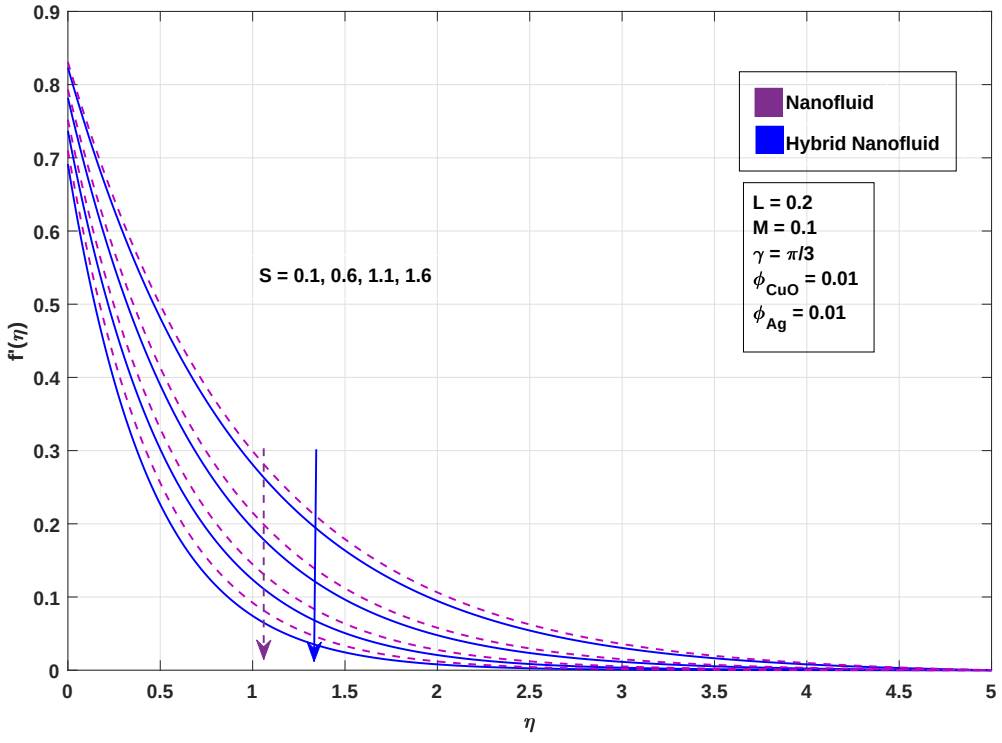

FIGURE 3.4: Impact of S on $f'(\eta)$

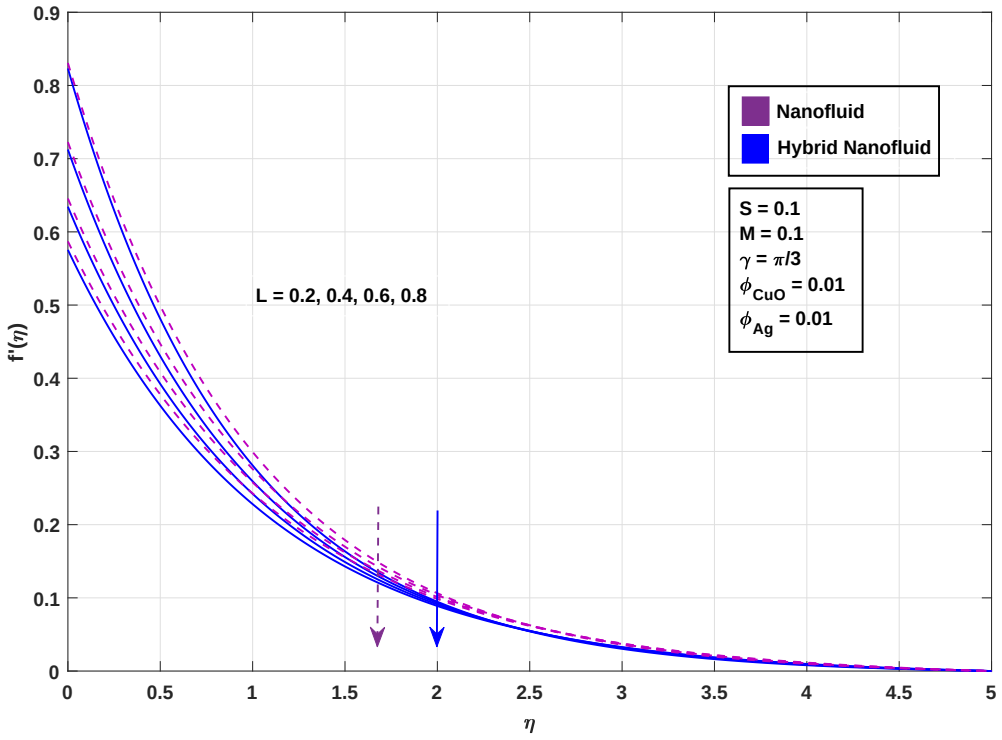

FIGURE 3.5: Impact of L on $f'(\eta)$

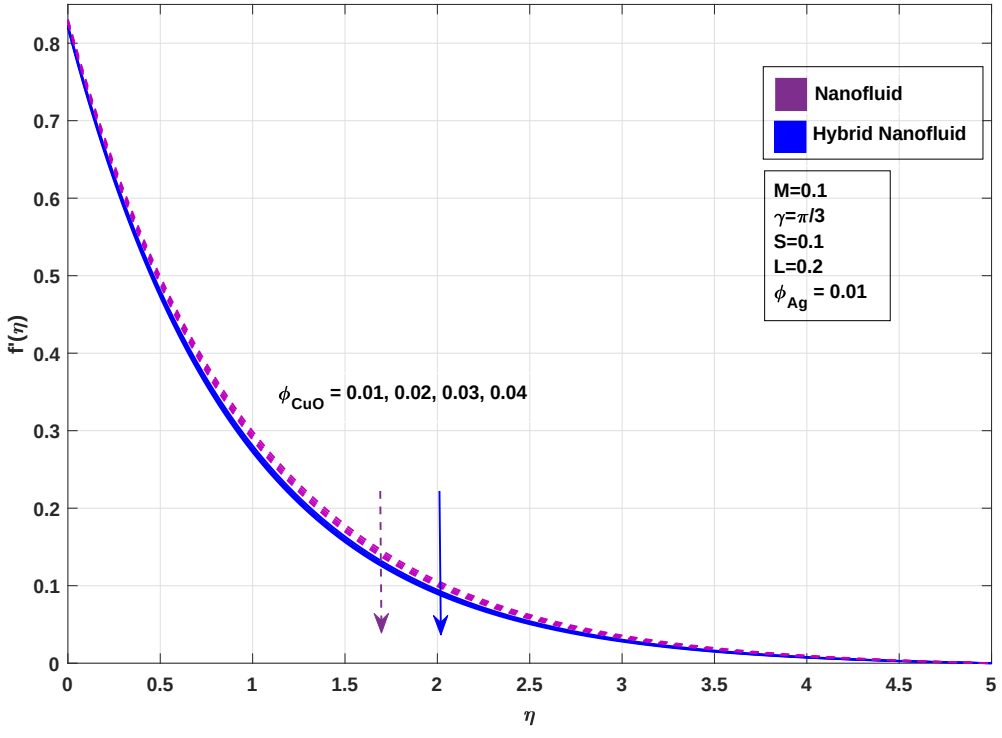

FIGURE 3.6: Impact of ϕ_{CuO} on $f'(\eta)$

3.6.3 Thermal Field

It is observed from Figure 3.7 that by rising the values of Prandtl number Pr, a significant reduction in the fluid temperature distribution is obtained and the associated thermal boundary layer becomes thinner. From the Figure 3.8 it is concluded that a rise in values of N enhances radiative energy transfer, which consequently raises the fluid temperature and thermal boundary layer becomes thicker. Figure 3.9 elaborates that a higher heat source parameter λ indicates greater internal heat generation within the fluid, which supplies additional thermal energy to the system. This excessive heat raises the fluid temperature and causes the thermal boundary layer to expand, as heat diffuses farther from the heated surface. Furthermore, a rise in the temperature of fluid with an increase in Biot number can be observed in the Figure 3.10. Physically, with higher Biot number convective heat transfer at the boundary is strengthened, elevating the fluid temperature and thickening the thermal boundary layer. An increase in copper oxide volume fraction (ϕ_{CuO}) enhances the effective thermal conductivity of the nanofluid, allowing more efficient heat transfer from the surface to the fluid. As a result, the fluid temperature rises and the thermal boundary layer becomes thicker. This behavior can be observed in the Figure 3.11

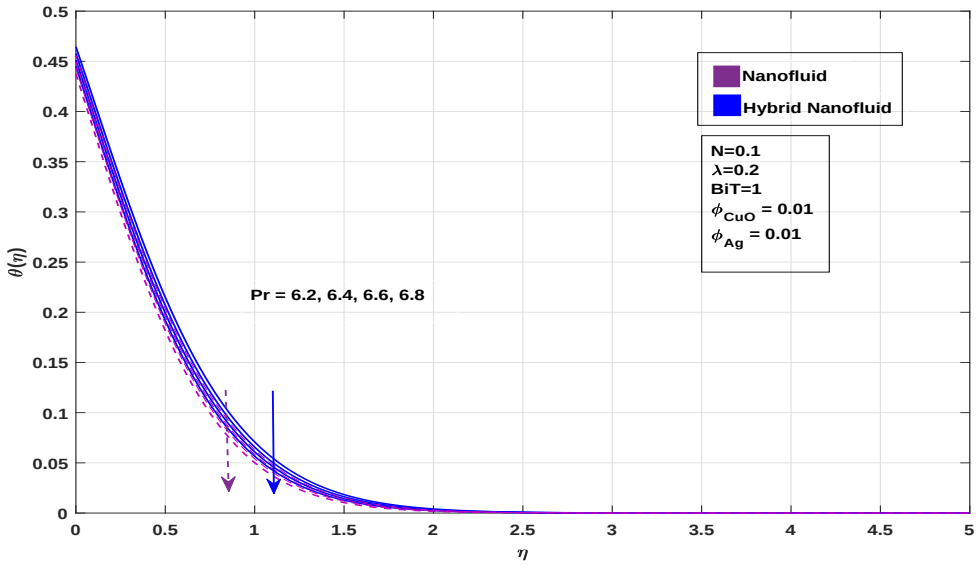

FIGURE 3.7: Impact of Pr on temperature profile

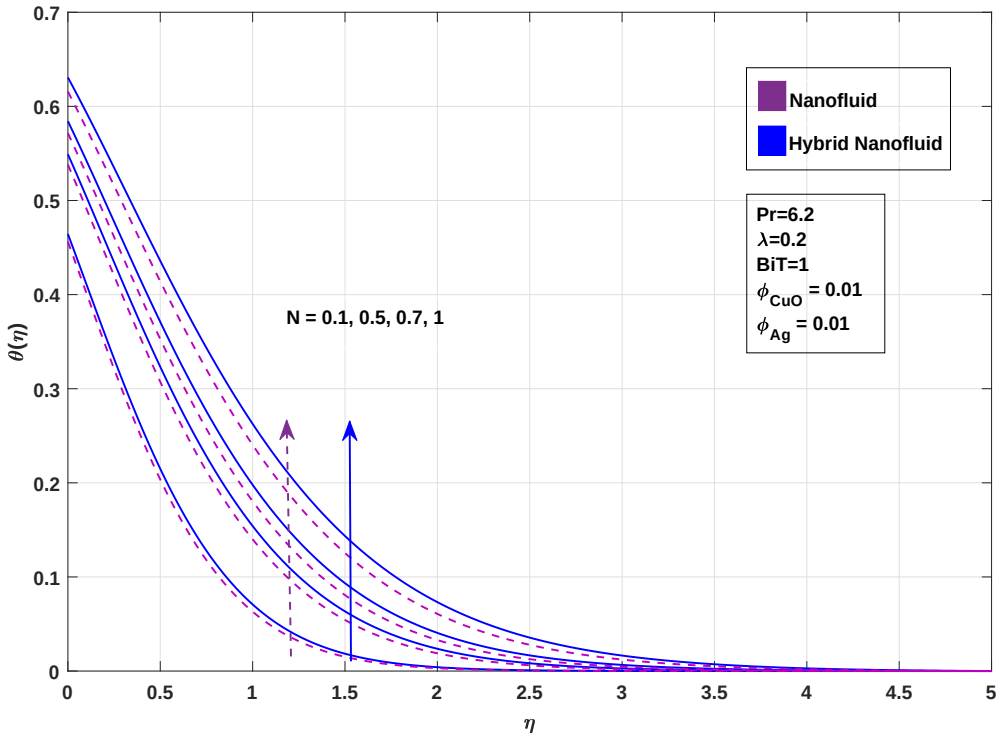

FIGURE 3.8: Impact of N on temperature profile

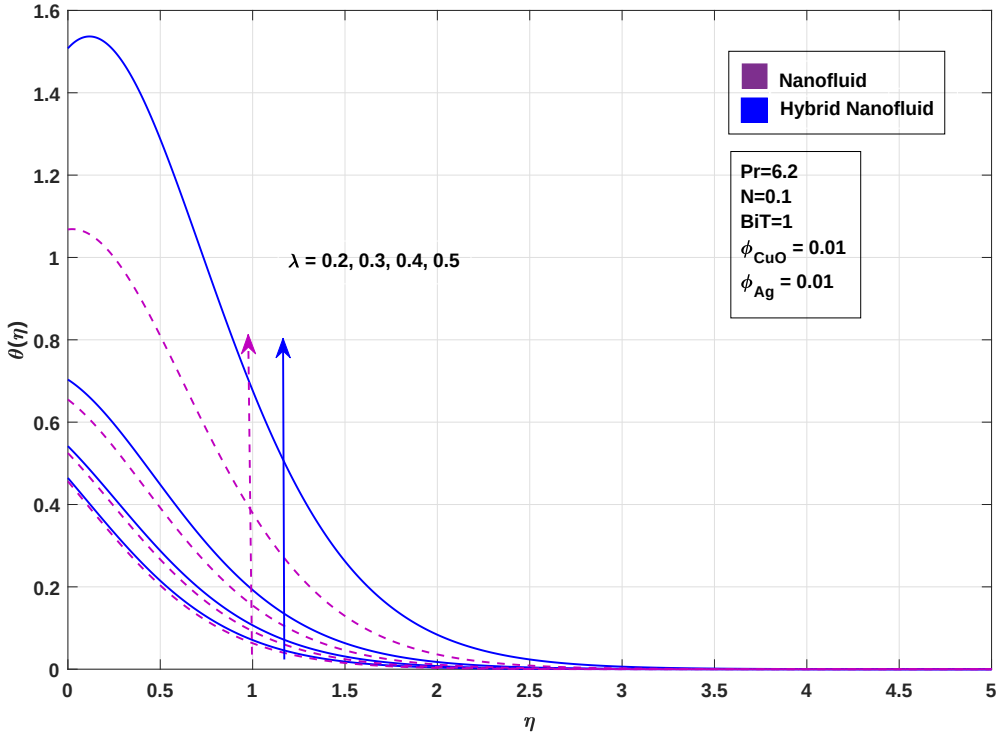

FIGURE 3.9: Impact of λ on temperature profile

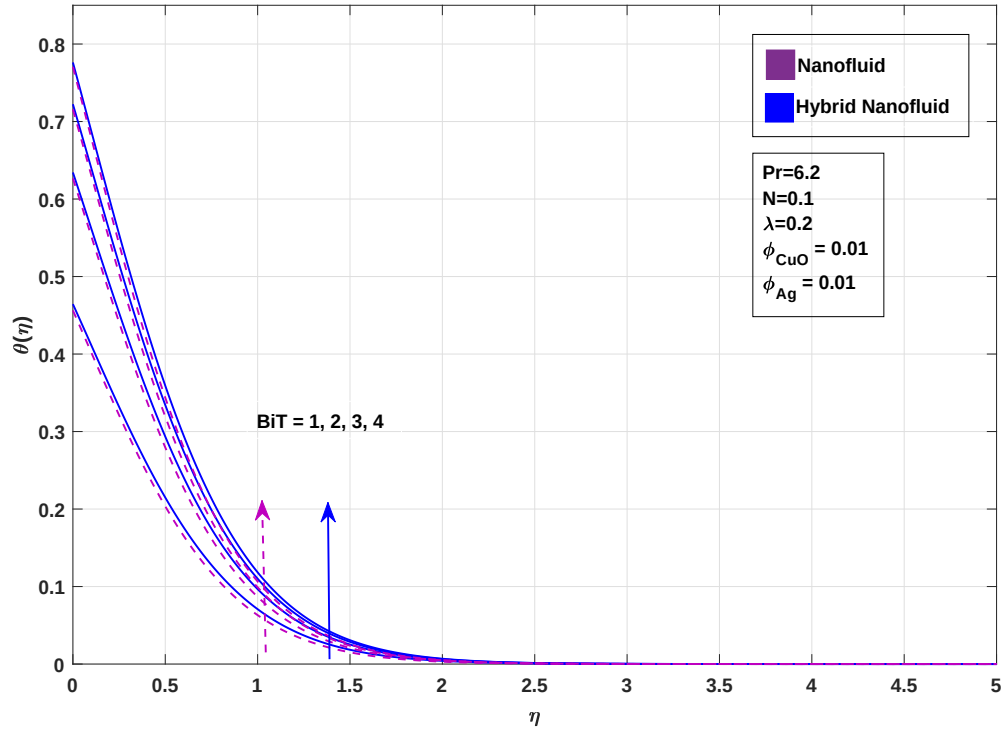

FIGURE 3.10: Impact of B_i on temperature profile

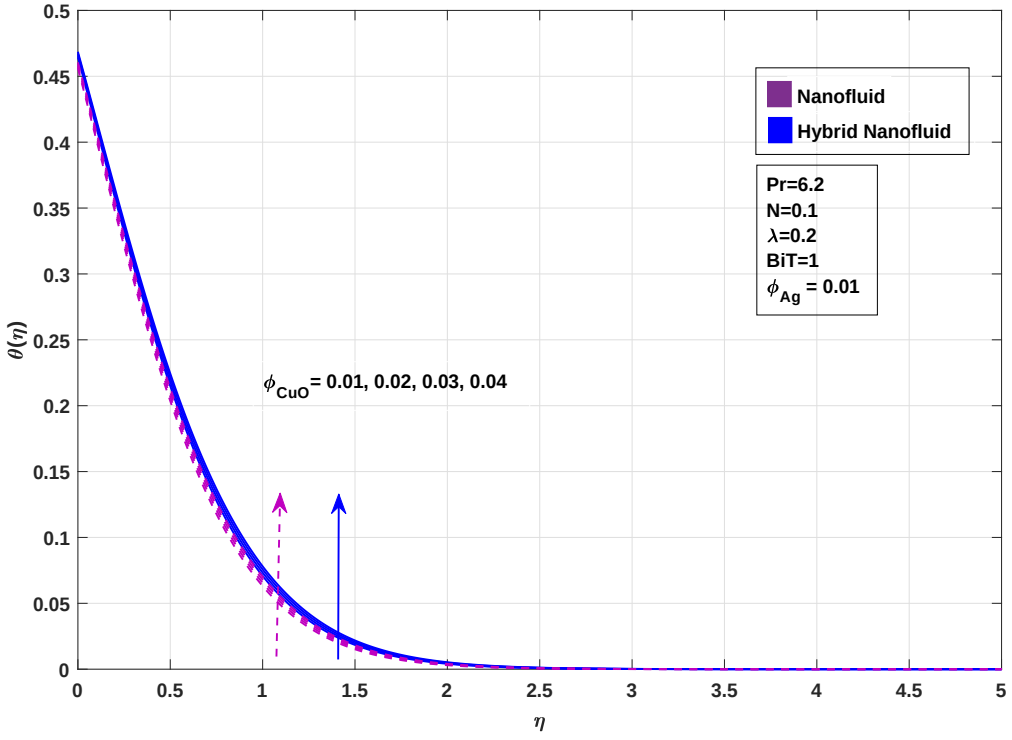

FIGURE 3.11: Impact of ϕ_{CuO} on temperature profile

Chapter 4

A Computational Analysis of Unsteady Radiative Chemical Reactive Hybrid Nanofluid Flow within Porous Media

4.1 Introduction

In this chapter, the work of Reddy et al. [37] is extended. The study investigates an unsteady hybrid nanofluid flow over a stretching sheet under the velocity slip condition and oblique Lorentz force with the sheet subjected to the radiative heat. The governing equations, originally in partial differential form, are reduced to ordinary differential equations via similarity transformations. Numerical results are obtained using the shooting method combined with the Runge-Kutta Method of order 4. Graphical representations of the velocity, temperature and concentration profiles are presented for various dimensionless parameters. Furthermore, computational results for the skin friction coefficient, Nusselt number and Sherwood number are also provided.

4.2 Mathematical Model

The present analysis deals with the convective heat transfer in a water and ethylene glycol based hybrid nanofluid induced flow over stretching sheet subjected to an inclined magnetic field. The applied magnetic field has constant magnitude B_0 and is inclined at an angle γ from the normal. The hybrid nanofluid, assumed to be incompressible, unsteady and laminar, flows in a two-dimensional domain, with velocity components u and v along the Cartesian coordinates x and y, respectively. The stretching of the surface initiates the flow and radiative heat transfer is included to capture the thermal radiation effects.

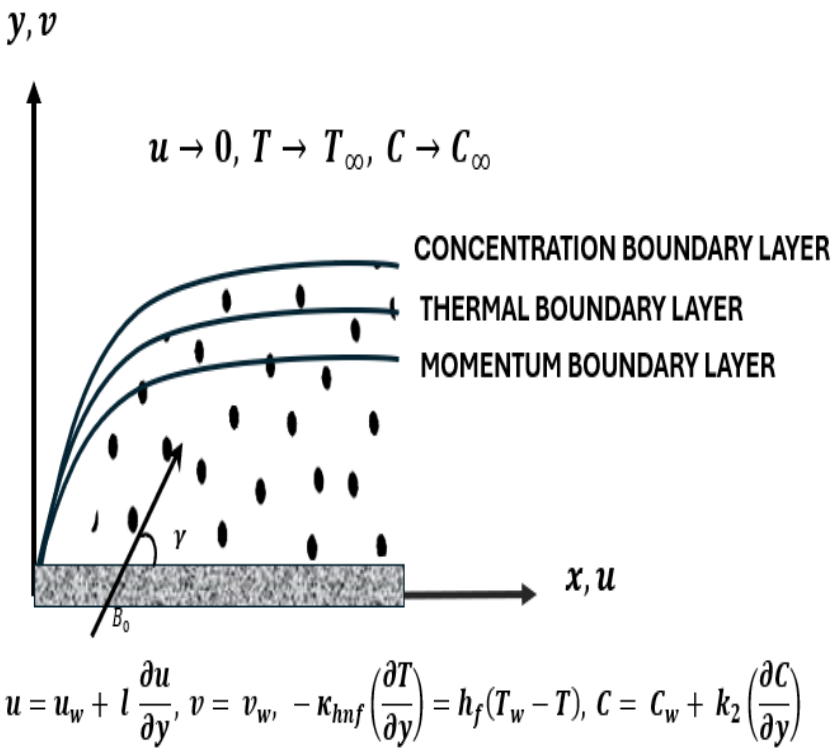

FIGURE 4.1: Systematic representation of physical model

Based on the aforementioned assumptions and physical considerations, the governing equations describing the fluid flow and heat transfer are given by the continuity, momentum, energy and concentration equations as follows.

Continuity Equation:

$$\frac{\partial u}{\partial x}+\frac{\partial v}{\partial y}=0. \tag{4.1}$$

Momentum Equation:

$$\frac{\partial u}{\partial t}+u\frac{\partial u}{\partial x}+v\frac{\partial v}{\partial y}=\frac{\mu_{hnf}}{\rho_{hnf}}\frac{\partial^2 u}{\partial^2 y}-\frac{\sigma_{hnf}}{\rho_{hnf}}B_0^2 u\sin^2\gamma-\frac{\mu_{hnf}}{\rho_{hnf}}\frac{u}{K}. \tag{4.2}$$

Energy Equation:

$$\begin{aligned}\frac{\partial T}{\partial t}+u\frac{\partial T}{\partial x}+v\frac{\partial T}{\partial y}&=\frac{\kappa_{hnf}}{(\rho C_p)_{hnf}}\frac{\partial^2 T}{\partial y^2}-\frac{1}{(\rho C_P)_{hnf}}\frac{\partial q_r}{\partial y}+\frac{q'''}{(\rho C_p)_{hnf}}\\&+\frac{\mu_{hnf}}{(\rho C_p)_{hnf}}\left(\frac{\partial u}{\partial y}\right)^2+\frac{\sigma_{hnf}}{(\rho C_P)_{hnf}}B_0^2u^2\sin^2\gamma+\frac{\mu_{hnf}}{(\rho C_P)_{hnf}}\left(\frac{u^2}{K}\right).\end{aligned} \tag{4.3}$$

Concentration Equation:

$$\frac{\partial C}{\partial t}+u\frac{\partial C}{\partial x}+v\frac{\partial C}{\partial y}=(D_m)_{hnf}\frac{\partial^2 C}{\partial y^2}-k_r^2\left(\frac{T}{T_\infty}\right)^m exp\left(\frac{-E_a}{kT}\right)(C-C_\infty). \tag{4.4}$$

Boundary Conditions:

$$\left.\begin{aligned}&\text{At } y=0: u=u_w+l\frac{\partial u}{\partial y},\ v=v_w,\ -\kappa_{hnf}\frac{\partial T}{\partial y}=h_f\left(T_w-T\right),C=C_w+k_2\frac{\partial C}{\partial y}\\&\text{As } \ y\longrightarrow\infty:\ \ u\longrightarrow 0,\ \ T\longrightarrow T_\infty.\end{aligned}\right\} \tag{4.5}$$

where l is the velocity slip parameter, h_f the convective heat coefficient and k_2 the concentration slip parameter.

4.3 Similarity Transformations and Non- dimensionalisation of Mathematical Model

In this section, the process of non-dimensionalisation for the mathematical model governing the behavior of the hybrid nanofluid is presented. The procedure requires introducing the dimensionless variables and parameters to transform the original equations into a simpler form. By using the dimensionless quantities, a deeper insight into the physical phenomena is gained and the analysis is made more tractable. The following similarity transformation [15] will be applied to

convert the mathematical model into a system of ODEs:

$$u = \frac{ax}{1-\alpha t} f'(\eta), \quad v = -\sqrt{\frac{a\nu_f}{1-\alpha t}} f(\eta),$$

$$\theta(\eta) = \frac{T - T_\infty}{T_w - T_\infty}, \quad \phi(\eta) = \frac{C - C_\infty}{C_w - C_\infty}, \qquad \eta = \sqrt{\frac{a}{\nu_f(1-\alpha t)}} y.$$

4.3.1 Non-dimensionalisation of Continuity Equation

The derivatives required to satisfy the continuity equation are given as:

$$\begin{aligned} \frac{\partial u}{\partial x} &= \frac{\partial}{\partial x}\left(\frac{ax}{1-\alpha t}.\right) f'(\eta) \\ &= \frac{a}{1-\alpha t} f'(\eta). \end{aligned} \tag{4.6}$$

$$\begin{aligned} \frac{\partial v}{\partial y} &= \frac{\partial}{\partial y}\left(-\sqrt{\frac{a\nu_f}{1-\alpha t}} f(\eta)\right) \\ &= -\sqrt{\frac{a\nu_f}{1-\alpha t}} f'(\eta) \frac{\partial \eta}{\partial y} \\ &= -\sqrt{\frac{a\nu_f}{1-\alpha t}} f'(\eta) \sqrt{\frac{a}{\nu_f(1-\alpha t)}} \\ &= -a f'(\eta). \end{aligned} \tag{4.7}$$

By substitution of (4.6) and (4.7) in (4.1)

$$a f'(\eta) - a f'(\eta) = 0,$$

which shows that continuity equation is satisfied identically.

4.3.2 Non-dimensionalisation of Momentum Equation

For momentum equation, the required derivatives are:

$$u\frac{\partial u}{\partial x} = \left(\frac{ax}{1-\alpha t} f'(\eta)\right)\left(\frac{a}{1-\alpha t} f'(\eta)\right).$$

$$\Rightarrow \qquad u\frac{\partial u}{\partial x} = \frac{a^2 x}{(1-\alpha t)^2} f'^2(\eta). \tag{4.8}$$

$$\frac{\partial u}{\partial y} = \frac{\partial}{\partial y}\left(\frac{ax}{1-\alpha t} f'(\eta)\right)$$

$$= \frac{ax}{1-\alpha t} f'' \frac{\partial \eta}{\partial y}$$

$$= \frac{ax}{1-\alpha t} f'' \sqrt{\frac{a}{\nu_f(1-\alpha t)}}.$$

$$v\frac{\partial u}{\partial y} = \sqrt{\frac{a}{\nu_f(1-\alpha t)}} f(\eta) \frac{ax}{1-\alpha t} f'' \sqrt{\frac{a}{\nu_f(1-\alpha t)}}.$$

$$\Rightarrow \qquad v\frac{\partial u}{\partial y} = \frac{-a^2 x}{(1-\alpha t)^2} f f''. \tag{4.9}$$

$$\frac{\partial u}{\partial t} = axf'(\eta)\frac{d}{dt}\left(\frac{1}{1-\alpha t}\right) + \frac{ax}{1-\alpha t}\frac{\partial}{\partial t}\left(f'(\eta)\right)$$

$$= axf'(\eta)\left(\frac{-(-\alpha)}{(1-\alpha t)^2}\right) + \frac{ax}{1-\alpha t} f''(\eta)\frac{\partial \eta}{\partial t}$$

$$= \frac{ax\alpha f'}{(1-\alpha t)^2} + \frac{axf''}{1-\alpha t}\frac{\partial}{\partial t}\left(\sqrt{\frac{a}{\nu_f(1-\alpha t)}} y\right)$$

$$= \frac{ax\alpha f'}{(1-\alpha t)^2} + \sqrt{\frac{a}{\nu_f}}\frac{axy}{1-\alpha t} f'' \frac{d}{dt}\left((1-\alpha t)^{-1/2}\right)$$

$$= \frac{ax\alpha f'}{(1-\alpha t)^2} + \sqrt{\frac{a}{\nu_f}}\frac{axy}{1-\alpha t} f''\left(\frac{\alpha}{2}(1-\alpha t)^{-3/2}\right).$$

$$\Rightarrow \qquad \frac{\partial u}{\partial t} = \frac{ax\alpha f'}{(1-\alpha t)^2} + \frac{\alpha}{2}\sqrt{\frac{a}{\nu_f}}\frac{axyf''}{\sqrt{(1-\alpha t)^5}}.$$

$$= \frac{ax\alpha f'}{(1-\alpha t)^2} + \frac{\alpha}{2}\sqrt{\frac{a}{\nu_f}}\frac{axf''}{\sqrt{(1-\alpha t)^5}}\sqrt{\frac{\nu_f(1-\alpha t)}{a}}\eta.$$

$$= \frac{ax\alpha f'}{(1-\alpha t)^2} + \frac{ax\alpha f''}{2(1-\alpha t)^2}\eta.$$

$$= \frac{ax\alpha}{(1-\alpha t)^2}\left(f' + \frac{\eta}{2}\right). \tag{4.10}$$

$$\frac{\partial^2 u}{\partial^2 y} = \frac{\partial}{\partial y}\left(\frac{\partial u}{\partial y}\right)$$

$$= \frac{\partial}{\partial y}\left(\frac{ax}{(1-\alpha t)}\sqrt{\frac{a}{\nu_f(1-\alpha t)}} f''\right)$$

$$= \frac{ax}{1-\alpha t}\sqrt{\frac{a}{\nu_f(1-\alpha t)}}f'''\left(\sqrt{\frac{a}{\nu_f(1-\alpha t)}}\right).$$

$$\Rightarrow \quad \frac{\partial^2 u}{\partial^2 y} = \frac{a^2 x}{(1-\alpha t)^2\nu_f}f'''.$$

$$\Rightarrow \quad \frac{\mu_{hnf}}{\rho_{hnf}}\frac{\partial^2 u}{\partial^2 y} = \frac{\mu_{hnf}}{\rho_{hnf}}\frac{a^2 x}{\nu_f}f'''. \tag{4.11}$$

$$\frac{\sigma_{hnf}}{\rho_{hnf}}B_0^2 u\sin^2\gamma = \frac{\sigma_{hnf}}{\rho_{hnf}}B_0^2 axf'\sin^2\gamma. \tag{4.12}$$

$$\frac{u}{K} = \frac{axf'(\eta)}{K(1-\alpha t)}.$$

$$\frac{\mu_{hnf}}{\rho_{hnf}}\frac{u}{K} = \frac{\mu_{hnf}}{\rho_{hnf}}\frac{axf'(\eta)}{K(1-\alpha t)}. \tag{4.13}$$

Using equations (4.8)-(4.13) the momentum equation (4.2) becomes:

$$\frac{a^2 x}{(1-\alpha t)^2}\left(\frac{\alpha}{a}f' + \frac{\alpha\eta}{2a}f'' + f'^2 - ff''\right)$$

$$= \frac{a^2 x}{(1-\alpha t)^2}\left(\frac{\mu_{hnf}f'''}{\rho_{hnf}\nu_f} - \frac{\sigma_{hnf}B_0^2(1-\alpha t)}{\rho_{hnf}a}\sin^2\gamma f' - \frac{\mu_{hnf}(1-\alpha t)f'}{\rho_{hnf}Ka}\right).$$

$$\Rightarrow \quad \frac{\alpha}{a}f' + \frac{\alpha\eta}{2a}f'' + f'^2 - ff''$$

$$= \frac{\mu_{hnf}f'''}{\rho_{hnf}\nu_f} - \frac{\sigma_{hnf}B_0^2(1-\alpha t)}{\rho_{hnf}a}\sin^2\gamma f' - \frac{\mu_{hnf}(1-\alpha t)f'}{\rho_{hnf}Ka}$$

$$= \left(\frac{\mu_{hnf}/\mu_f}{\rho_{hnf}/\rho_f}\right)\frac{\mu_f}{\rho_f}\frac{f'''}{\nu_f} - \left(\frac{\sigma_{hnf}/\sigma_f}{\rho_{hnf}/\rho_f}\right)\frac{\sigma_f}{\rho_f}\frac{B_0^2(1-\alpha t)}{a}\sin^2\gamma f'$$

$$- \left(\frac{\mu_{hnf}/\mu_f}{\rho_{hnf}/\rho_f}\right)\frac{\mu_f}{\rho_f}\frac{(1-\alpha t)}{Ka}f'$$

$$= \left(\frac{\mu_{hnf}/\mu_f}{\rho_{hnf}/\rho_f}\right)f''' - \left(\frac{\sigma_{hnf}/\sigma_f}{\rho_{hnf}/\rho_f}\right)M\sin^2\gamma f' - \left(\frac{\mu_{hnf}/\mu_f}{\rho_{hnf}/\rho_f}\right)k_1 f'.$$

$$\Rightarrow \quad U_P f' + \frac{\epsilon\eta}{2}f'' + f'^2 - ff''$$

$$= \left(\frac{\mu_{hnf}/\mu_f}{\rho_{hnf}/\rho_f}\right)f''' - \left(\frac{\sigma_{hnf}/\sigma_f}{\rho_{hnf}/\rho_f}\right)M\sin^2\gamma f' - \left(\frac{\mu_{hnf}/\mu_f}{\rho_{hnf}/\rho_f}\right)k_1 f'.$$

$$\Rightarrow f''' - \left(\frac{P_3}{P_2}\right)M\sin^2\gamma f' - \left(\frac{P_1}{P_2}\right)(f' + \frac{U_P\eta}{2}f'' + f'^2 - ff'') - k_1 f' = 0, \tag{4.14}$$

where $P_1 = \frac{\rho_{hnf}}{\rho_f}$, $P_2 = \frac{\mu_{hnf}}{\mu_f}$ and $P_3 = \frac{\sigma_{hnf}}{\sigma_f}$.

The equation (4.14) represents non-dimensional form of momentum equation.

4.3.3 Non-dimensionalisation of Energy Equation

The required derivatives for energy equation are:

$$\frac{\partial T}{\partial t} = (T_w - T_\infty)\theta'(\eta)\frac{\partial \eta}{\partial t}$$

$$= (T_w - T_\infty)\theta'\left(\frac{\eta\alpha}{2(1-\alpha t)}\right).$$

$$\Rightarrow \quad \frac{\partial T}{\partial t} = \left(\frac{\eta\alpha(T_w - T_\infty)}{2(1-\alpha t)}\right)\theta'. \tag{4.15}$$

$$\frac{\partial T}{\partial x} = \frac{\partial}{\partial x}(\theta(\eta)(T_w - T_\infty) + T_\infty)$$

$$= \theta'(\eta)\frac{\partial \eta}{\partial x}(T_w - T_\infty) = 0.$$

$$\Rightarrow \quad u\frac{\partial T}{\partial x} = 0. \tag{4.16}$$

$$\frac{\partial T}{\partial y} = (T_w - T_\infty)\theta'(\eta)\frac{\partial \eta}{\partial y}$$

$$= (T_w - T_\infty)\theta'\sqrt{\frac{a}{\nu_f}}.$$

$$\Rightarrow \quad v\frac{\partial T}{\partial y} = -\sqrt{a\nu_f}(T_w - T_\infty)f\theta'\sqrt{\frac{a}{\nu_f}}.$$

$$\Rightarrow \quad v\frac{\partial T}{\partial y} = -a(T_w - T_\infty)f\theta'. \tag{4.17}$$

$$\frac{\partial^2 T}{\partial^2 y} = \frac{\partial}{\partial y}\left((T_w - T_\infty)\theta'(\eta)\sqrt{\frac{a}{\nu_f}}\right)$$

$$= (T_w - T_\infty)\sqrt{\frac{a}{\nu_f}}\theta''(\eta)\frac{\partial \eta}{\partial y}$$

$$= (T_w - T_\infty)\sqrt{\frac{a}{\nu_f}}\theta''\sqrt{\frac{a}{\nu_f}}.$$

$$\Rightarrow \quad \frac{\partial^2 T}{\partial^2 y} = \frac{a}{\nu_f}(T_w - T_\infty)\theta''. \tag{4.18}$$

$$\frac{\partial q_r}{\partial y} = \frac{-16T_\infty^3\sigma^*}{3K^*}\frac{\partial^2 T}{\partial y^2}$$

$$= \frac{-16T_\infty^3\sigma^*}{3K^*}\left(\frac{(T_w - T_\infty)a}{\nu_f}\theta''\right). \tag{4.19}$$

$$q''' = \frac{\kappa_{hnf}u_w}{x\nu_{hnf}}\left(A_1(T_w - T_\infty)f' + B_1(T - T_\infty)\right)$$

$$= \frac{\kappa_{hnf}ax}{x\nu_{hnf}(1-\alpha t)}\left(A_1(T_w - T_\infty)f' + B_1((T_w - T_\infty)\theta + T_\infty - T_\infty)\right)$$

$$= \frac{a\kappa_{hnf}}{(1-\alpha t)\nu_{hnf}}\left(A_1(T_w - T_\infty)f' + B_1((T_w - T_\infty)\theta)\right)$$

$$= \frac{a\kappa_{hnf}}{(1-\alpha t)\nu_{hnf}}(T_w - T_\infty)\left(A_1 f' + B_1\theta\right)$$

$$= \frac{(\kappa_{hnf}/\kappa_f)\kappa_f}{(\nu_{hnf}/\nu_f)\nu_f}\frac{a(T_w - T_\infty)}{(1-\alpha t)}\left(A_1 f' + B_1\theta\right)$$

$$= \left(\frac{\kappa_{hnf}/\kappa_f}{\nu_{hnf}/\nu_f}\right)\frac{\kappa_f}{\nu_f}\frac{a(T_w - T_\infty)}{(1-\alpha t)}\left(A_1 f' + B_1\theta\right). \tag{4.20}$$

$$\left(\frac{\partial u}{\partial y}\right)^2 = \frac{a^2x^2f''^2}{(1-\alpha t)^2}\left(\frac{a}{\nu_f(1-\alpha t)}\right) = \frac{a^3x^2f''^2}{\nu_f(1-\alpha t)^3}. \tag{4.21}$$

$$B_0^2u^2\sin^2\gamma = B_0^2\sin^2\gamma\left(\frac{a^2x^2}{(1-\alpha t)^2}\right)f'^2. \tag{4.22}$$

$$\frac{u^2}{K} = \frac{1}{K}\left(\frac{a^2x^2f'^2}{(1-\alpha t)^2}\right). \tag{4.23}$$

Using equations (4.15)-(4.23), the energy equation (4.3) becomes:

$$\frac{(T_w - T_\infty)}{(1-\alpha t)}\frac{\alpha\eta}{2}\theta' - \frac{(T_w - T_\infty)}{(1-\alpha t)}af\theta' = \frac{(T_w - T_\infty)a}{(\rho C_P)_{hnf}(1-\alpha t)}\frac{\kappa_{hnf}}{\kappa_f}\frac{\kappa_f}{\nu_f}\theta''$$

$$+\frac{(T_w - T_\infty)a}{(\rho C_P)_{hnf}(1-\alpha t)\nu_f}\frac{4}{3}\left(\frac{4T_\infty^3\sigma^*}{k^*\kappa_f}\kappa_f\right)\theta'' + \left(\frac{(T_w - T_\infty)a}{(\rho C_P)_{hnf}(1-\alpha t)}\frac{\kappa_{hnf}/\kappa_f}{\nu_{hnf}/\nu_f}\frac{\kappa_f}{\nu_f}\right)$$

$$(A_1 f' + B_1\theta) + \frac{\mu_f}{(\rho C_P)_{hnf}}\frac{\mu_{hnf}}{\mu_f}\frac{a^3x^2f''^2}{\nu_f(1-\alpha t)^3}$$

$$+\frac{1}{(\rho C_P)_{hnf}}\frac{\sigma_{hnf}}{\sigma_f}\frac{\sigma_f B_0^2\sin^2\gamma a^2x^2f'^2}{(1-\alpha t)^2} + \frac{\mu_f}{(\rho C_P)_{hnf}}\frac{\mu_{hnf}}{\mu_f}\frac{a^2x^2f'^2}{K(1-\alpha t)^2} \tag{4.24}$$

$$\Rightarrow \quad (\rho C_P)_{hnf}\left(\frac{\alpha\eta}{2a}\theta' - f\theta'\right) = \frac{\kappa_{hnf}}{\kappa_f}\frac{\kappa_f}{\nu_f}\theta'' + \frac{4N}{3}\frac{\kappa_f}{\nu_f}\theta''$$

$$+\frac{\kappa_{hnf}/\kappa_f}{\nu_{hnf}/\nu_f}\frac{\kappa_f}{\nu_f}(A_1 f' + B_1\theta) + \frac{\mu_{hnf}}{\mu_f}\frac{\mu_f}{\nu_f}\frac{a^2x^2f''^2}{(1-\alpha t)^2(T_w - T_\infty)}$$

$$
\begin{aligned}
&+\frac{\sigma_{hnf}}{\sigma_f}\frac{\sigma_f B_0^2 \sin^2\gamma a x^2 f'^2}{(1-\alpha t)(T_w-T_\infty)}+\frac{\mu_{hnf}}{\mu_f}\frac{a x^2 f'^2}{K(1-\alpha t)(T_w-T_\infty)}\\
&=\frac{\kappa_f}{\nu_f}\left(\frac{\kappa_{hnf}}{\kappa_f}+\frac{4N}{3}\right)\theta''+\frac{\kappa_f}{\nu_f}\left(\frac{\kappa_{hnf}/\kappa_f}{\nu_{hnf}/\nu_f}(A_1 f'+B_1\theta)\right)\\
&+\frac{\mu_{hnf}}{\mu_f}\frac{\mu_f a x^2 f'^2}{(1-\alpha t)(T_w-T_\infty)}\\
&=\frac{\kappa_f}{\nu_f}\left(\frac{\kappa_{hnf}}{\kappa_f}+\frac{4N}{3}\right)\theta''+\frac{\kappa_f}{\nu_f}\left(\frac{\kappa_{hnf}/\kappa_f}{\nu_{hnf}/\nu_f}(A_1 f'+B_1\theta)\right)\\
&+\frac{\mu_{hnf}}{\mu_f}(C_P)_f Ec f''^2+\frac{\sigma_{hnf}}{\sigma_f}MEc(C_P)_f\rho_f f'^2\\
&+\frac{\mu_{hnf}}{\mu_f}\frac{\mu_f}{K}\frac{a(1-\alpha t)}{a(1-\alpha t)^2}\frac{(C_P)_f}{(C_P)_f}.\\
&=\frac{\kappa_f}{\nu_f}\left(\frac{\kappa_{hnf}}{\kappa_f}+\frac{4N}{3}\right)\theta''+\frac{\kappa_f}{\nu_f}\left(\frac{\kappa_{hnf}/\kappa_f}{\nu_{hnf}/\nu_f}(A_1 f'+B_1\theta)\right)\\
&+\frac{\mu_{hnf}}{\mu_f}(C_P)_f Ec f''^2+\frac{\sigma_{hnf}}{\sigma_f}MEc(C_P)_f\rho_f f'^2\\
&+\frac{\mu_{hnf}}{\mu_f}\mu_f Ec(1-\alpha t)f'^2.\\
\Rightarrow\ &\frac{(\rho_{C_P})_{hnf}}{(\rho_{C_P})_f}\left(\frac{U_P\eta}{2}\theta'-f\theta'\right)=\frac{\kappa_f}{(\rho_{C_P})_f\nu_f}\left(\frac{\kappa_{hnf}}{\kappa_f}+\frac{4N}{3}\right)\theta''\\
&+\frac{\kappa_f}{(\rho_{C_P})_f\nu_f}\left(\frac{\kappa_{hnf}/\kappa_f}{\nu_{hnf}/\nu_f}(A_1 f'+B_1\theta)\right)+\frac{\mu_{hnf}}{\mu_f}\frac{\rho_f(C_P)_f}{(\rho_{C_P})_f}Ec f''^2\\
&+\frac{\rho_f}{(\rho_{C_P})_f}\frac{\sigma_{hnf}}{\sigma_f}M(C_P)_f Ec+\frac{(C_P)_f}{(\rho_{C_P})_f}\frac{\mu_{hnf}}{\mu_f}\frac{\mu_f}{Ka}(1-\alpha t)f'^2.\\
=\ &\frac{\kappa_f}{(\rho_{C_P})_f\nu_f}\left(\frac{\kappa_{hnf}}{\kappa_f}+\frac{4N}{3}\right)\theta''+\frac{\kappa_f}{\mu_f(C_P)_f}\left(\frac{\kappa_{hnf}/\kappa_f}{\nu_{hnf}/\nu_f}(A_1 f'+B_1\theta)\right)+\frac{\mu_{hnf}}{\mu_f}Ec f''^2\\
&+\frac{\sigma_{hnf}}{\sigma_f}MEc f'^2+\frac{\mu_{hnf}}{\mu_f}\frac{\nu_f}{Ka}(1-\alpha t)f'^2.\\
\Rightarrow\ &\frac{(\rho_{C_P})_{hnf}}{(\rho_{C_P})_f}\left(\frac{U_P\eta}{2}\theta'-f\theta'\right)=\frac{1}{Pr}\left(\frac{\kappa_{hnf}}{\kappa_f}+\frac{4N}{3}\right)\theta''+\frac{1}{Pr}\left(\frac{\kappa_{hnf}/\kappa_f}{\nu_{hnf}/\nu_f}(A_1 f'+B_1\theta)\right)\\
&+\frac{\mu_{hnf}}{\mu_f}Ec f''^2+\frac{\sigma_{hnf}}{\sigma_f}MEc f'^2+\frac{\mu_{hnf}}{\mu_f}\frac{\nu_f}{k_1}f'^2.\\
\Rightarrow\ &P_5\left(\frac{U_P\eta}{2}\theta'-f\theta'\right)=\frac{1}{Pr}\left(P_4+\frac{4N}{3}\right)\theta''+\frac{1}{Pr}\left(\frac{P_4}{P_1}(A_1 f'+B_1\theta)\right)\\
&+P_2 Ec f''^2+P_3 MEc f'^2+P_2\frac{\nu_f}{k_1}f'^2, \qquad (4.25)
\end{aligned}
$$

where $P_4 = \frac{\kappa_{hnf}}{\kappa_f}$ and $P_5 = \frac{(\rho_{C_P})_{hnf}}{(\rho_{C_P})_f}$.

The above equation (4.25) represents non-dimensional form of energy equation.

4.3.4 Non-dimensionalisation of Concentration Equation

The derivatives required to compose dimensionless form of concentration equation:

$$C = (C_w - C_\infty)\phi + C_\infty, \qquad T = (T_w - T_\infty)\theta + T_\infty.$$

$$\frac{\partial C}{\partial t} = (C_w - C_\infty)\phi' \frac{\partial \eta}{\partial t}.$$

$$\Rightarrow \quad \frac{\partial C}{\partial t} = (C_w - C_\infty)\phi' \frac{\eta\alpha}{2(1-\alpha t)}. \tag{4.26}$$

$$\frac{\partial C}{\partial x} = 0.$$

$$\Rightarrow \quad u\frac{\partial C}{\partial x} = 0. \tag{4.27}$$

$$\frac{\partial C}{\partial y} = (C_w - C_\infty)\phi'(\eta)\frac{\partial \eta}{\partial y}$$

$$= (C_w - C_\infty)\phi' \sqrt{\frac{a}{\nu_f(1-\alpha t)}}.$$

$$\Rightarrow \quad v\frac{\partial C}{\partial y} = -\sqrt{\frac{a\nu_f}{(1-\alpha t)}} f(\eta)(C_w - C_\infty)\phi' \sqrt{\frac{a}{\nu_f(1-\alpha t)}}.$$

$$\Rightarrow \quad v\frac{\partial C}{\partial y} = \frac{-a(C_w - C_\infty)}{1-\alpha t} f\phi'. \tag{4.28}$$

$$\frac{\partial^2 C}{\partial y^2} = \frac{\partial}{\partial y}\left(\frac{\partial C}{\partial y}\right)$$

$$= \frac{\partial}{\partial y}\left((C_w - C_\infty)\phi' \sqrt{\frac{a}{\nu_f(1-\alpha t)}}\right)$$

$$= (C_w - C_\infty)\phi''(\eta)\frac{\partial \eta}{\partial y}\sqrt{\frac{a}{\nu_f(1-\alpha t)}}$$

$$= (C_w - C_\infty)\frac{\partial \eta}{\partial y}\sqrt{\frac{a}{\nu_f(1-\alpha t)}}\sqrt{\frac{a}{\nu_f(1-\alpha t)}}\phi''.$$

$$\Rightarrow \quad \frac{\partial^2 C}{\partial y^2} = \frac{a(C_w - C_\infty)}{\nu_f(1-\alpha t)}\phi''. \tag{4.29}$$

Using equations (4.26)-(4.29), concentration equation (4.4) becomes:

$$\frac{\eta\alpha(C_w-C_\infty)}{2(1-\alpha t)}\phi' - \frac{a(C_w-C_\infty)}{1-\alpha t}f\phi' = \frac{(D_m)_{hnf}a(C_w-C_\infty)}{\nu_f(1-\alpha t)}\phi''$$

$$-k_r^2\left(\frac{T_w-T_\infty}{T_\infty}\theta+1\right)\exp\left(\frac{-E_a}{k((T_w-T_\infty)\theta+T_\infty)}\right)(C_w-C_\infty)\,\phi.$$

$$\Rightarrow \frac{(C_w-C_\infty)a}{(1-\alpha t)}\left(\frac{\eta\alpha}{2a}-f\phi'\right) = \frac{(C_w-C_\infty)a}{(1-\alpha t)}\frac{(D_m)_{hnf}}{(D_m)_f}\frac{(D_m)_f}{\nu_f}\phi''$$

$$-\frac{k_r^2}{a}\left(\frac{T_w-T_\infty}{T_\infty}\theta+1\right)\exp\left(\frac{-E_a}{kT_\infty\left(\left(\frac{T_w-T_\infty}{T_\infty}\right)\theta+1\right)}\right)\phi.$$

$$\Rightarrow \frac{U_P\eta}{2}\phi' - f\phi' = \frac{P_6}{Sc}\phi'' - Cr(\delta\theta+1)\exp\left(\frac{-E}{\delta\theta+1}\right)\phi.$$

$$\Rightarrow P_6\phi'' - CrSc(\delta\theta+1)\exp\left(\frac{-E}{\delta\theta+1}\right)\phi + Sc\left(f\phi' - \frac{U_P\eta}{2}\phi'\right) = 0, \tag{4.30}$$

which is non-dimensional form of concentration equation, with $P_6 = \frac{(D_m)_{hnf}}{(D_m)_f}$.

4.3.5 Non-dimensionalisation of Boundary Conditions

- $u = u_w(x) + l\dfrac{\partial u}{\partial y}, \qquad at \quad y = 0.$

$$\Rightarrow \frac{ax}{1-\alpha t}f'(\eta) = \frac{ax}{1-\alpha t} + l\left(\frac{ax}{1-\alpha t}f''(\eta)\sqrt{\frac{a}{\nu_f(1-\alpha t)}}\right), \qquad at \quad \eta = 0.$$

$$\Rightarrow f'(\eta) = 1 + l\sqrt{\frac{a}{\nu_f(1-\alpha t)}}f''(\eta), \qquad at \quad \eta = 0.$$

$$\Rightarrow f'(\eta) = 1 + Lf''(\eta), \qquad at \quad \eta = 0.$$

$$\Rightarrow f'(0) = 1 + Lf''(0).$$

- $-\kappa_{hnf}\left(\dfrac{\partial T}{\partial y}\right) = h_f\left(T_w - T\right), \qquad at \quad y = 0.$

$$\Rightarrow -\kappa_{hnf}\left(T_w - T_\infty\right)\theta'(\eta)\sqrt{\frac{a}{\nu_f(1-\alpha t)}}$$

$$= h_f\left(T_w - (\theta(\eta)\left(T_w - T_\infty\right) + T_\infty)\right), \qquad at \quad \eta = 0.$$

$$\Rightarrow -\kappa_{hnf}\sqrt{\frac{a}{\nu_f(1-\alpha t)}}\theta'(\eta) = h_f\left(1 - \theta(\eta)\right), \qquad at \quad \eta = 0.$$

$$\Rightarrow \theta'(\eta) = -\sqrt{\frac{\nu_f(1-\alpha t)}{a}}\frac{h_f}{\kappa_{hnf}}\left(1-\theta(\eta)\right), \qquad at \quad \eta = 0.$$

$$\Rightarrow \quad \theta'(\eta) = -\sqrt{\frac{\nu_f(1-\alpha t)}{a}}\frac{h_f/\kappa_f}{\kappa_{hnf}/\kappa_f}\left(1-\theta(\eta)\right), \qquad at \quad \eta = 0.$$

$$\Rightarrow \quad \theta'(\eta) = -\frac{1}{\kappa_{hnf}/\kappa_f}\left(\sqrt{\frac{\nu_f(1-\alpha t)}{a}}\frac{h_f}{\kappa_f}\right)\left(1-\theta(\eta)\right), \qquad at \quad \eta = 0.$$

$$\Rightarrow \theta'(0) = -\frac{1}{\kappa_{hnf}/\kappa_f}B_i\left(1-\theta(0)\right).$$

- $C = C_w + k_2\dfrac{\partial C}{\partial y}, \qquad at \quad y = 0,$

$$\Rightarrow (C_w - C_\infty)\,\phi(\eta) + C_\infty = C_w + k_2\left((C_w - C_\infty)\,\phi'(\eta)\sqrt{\frac{a}{\nu_f(1-\alpha t)}}\right), at \;\; \eta = 0,$$

$$\Rightarrow \quad \phi(\eta) = 1 + k_2\left(\phi'(\eta)\sqrt{\frac{a}{\nu_f}}\right), \qquad at \quad \eta = 0,$$

$$\Rightarrow \quad \phi(0) = 1 + k_2\left(\phi'(0)\sqrt{\frac{a}{\nu_f}}\right).$$

4.3.6 Relevant Physical Quantities and Non-dimensional Elements

This analysis includes non-dimensional parameters like Schmidt number $Sc = \frac{\nu_f}{(D_m)_{hnf}}$, chemical reaction parameter $C_r = \frac{k_r^2}{a}$ and temperature difference parameter $\delta = \frac{(T_w - T_\infty)}{T_\infty}$.

4.3.7 Sherwood Number

The Sherwood number is very important for mathematicians and engineers while quantifying mass transfer. The mathematical elaboration of Sherwood number (Sh) is given below:

$$Sh_x = \frac{x}{C_w - C_\infty}\frac{\partial C}{\partial y}$$

$$C = (C_w - C_\infty)\phi(\eta) + C_\infty.$$

$$\Rightarrow \quad \frac{\partial C}{\partial y} = (C_w - C_\infty)\phi'(\eta)\sqrt{\frac{a}{\nu_f}}.$$

$$\therefore \quad Sh_x = x\phi'(\eta)\sqrt{\frac{a}{\nu_f}}, \qquad at \quad \eta = 0.$$

$$\Rightarrow \quad \sqrt{\frac{\nu_f}{ax^2}}Sh_x = \phi'(0).$$

$$\Rightarrow \quad \frac{Sh_x}{\sqrt{Re}} = \phi'(0).$$

4.4 Solution Framework

The numerical solutions are determined through the application of the shooting method, employing the fourth-order Runge-Kutta technique for computation of the solution of the initial value problem and Newton's method for refinement of the missing conditions.

To tackle the solution of the dimensionless momentum equation (4.14), the following notations have been adopted as an initial step:

$$f = \tau_1, \qquad f' = \tau_1' = \tau_2, \qquad f'' = \tau_1'' = \tau_2' = \tau_3, \qquad f''' = \tau_1''' = \tau_2'' = \tau_3'.$$

The momentum equation is then transformed into the following system of first order ODEs:

$$\tau_1' = \tau_2, \qquad \tau_1(0) = S,$$

$$\tau_2' = \tau_3, \qquad \tau_2(0) = 1 + LP,$$

$$\tau_3' = \left(\frac{P_3}{P_2}\right)(M\tau_2 \sin^2\gamma) + k_1\tau_2 + \left(\frac{P_1}{P_2}\right)\left(U_P\tau_2 + \tau_2^2 - \tau_1\tau_3 + (U_P\frac{\eta}{2}\tau_3)\right), \qquad \tau_3(0) = P.$$

The IVP described above will be solved numerically using the fourth-order Runge-Kutta method. The problem domain is assumed to be bounded i.e. $[0, \eta_\infty]$. The missing condition P is to be chosen such that:

$$\tau_3(\eta_\infty, P) = 0.$$

Newton-Raphson method will be used to update the missing P, using the following iterative scheme:

$$P_{n+1} = P_n - \frac{\tau_3(\eta_\infty, P_n)}{\left(\frac{\partial}{\partial P}\tau_3(\eta_\infty, P)\right)_{P=P_n}}. \tag{4.31}$$

The following notations are further introduced:

$$\frac{\partial \tau_1}{\partial P} = \tau_4, \quad \frac{\partial \tau_2}{\partial P} = \tau_5, \quad \frac{\partial \tau_3}{\partial P} = \tau_6.$$

Hence the iterative scheme (4.31) will get the form:

$$P_{n+1} = P_n - \frac{\tau_3(\eta_\infty, P_n)}{\tau_6(\eta_\infty, P_n)}.$$

Now, differentiating the last system of the first order ODEs with respect to P, another system of ODEs is obtained as follows:

$$\tau_4' = \tau_5, \qquad \tau_4(0) = 0.$$

$$\tau_5' = \tau_6, \qquad \tau_5(0) = L.$$

$$\tau_6' = \frac{P_3}{P_2}\left(M\tau_5 \sin^2\gamma\right) + k_1\tau_5 + \frac{P_1}{P_2}\left(U_P\tau_5 + 2\tau_2\tau_5 - \tau_4\tau_3 - \tau_1\tau_6\right) + U_P\frac{\eta}{2}\tau_6, \qquad \tau_6(0) = 1.$$

The stopping criteria for Newton's technique is set as:

$$|\tau_3(\eta_\infty, P)| < \epsilon,$$

where $\epsilon > 0$ denotes an arbitrarily small positive parameter. In the present analysis, ϵ is fixed at 10^{-10}.

The ordinary differential equation (4.25) will be approximated by using the shooting technique, assuming θ as a known function. For this, the following notions are utilized:

$$\theta = \zeta_1, \quad \theta' = \zeta_1' = \zeta_2.$$

The energy equation is then transformed into the following system of first-order ODEs:

$$\zeta_1' = \zeta_2, \qquad \zeta_1(0) = Q,$$

$$\zeta_2' = \left(\frac{Pr}{P_4 + \frac{4N}{3}}\right)\left[\frac{-1}{Pr}\left(\frac{P_1P_4}{P_2}\right)(A_1\tau_2 + B_1\zeta_1) - P_2Ec\tau_3^2 - P_3MEc\tau_2^2\right.$$

$$\left. -P_2k_1\tau_2^2 + P_5(U_P\frac{\eta}{2}\zeta_2 - \tau_1\zeta_2)\right], \qquad \zeta_2(0) = \left(\frac{-B_i}{P_4}\right)(1-Q).$$

The above initial value problem (IVP) will be numerically solved by the Runge-Kutta method of order 4. The missing condition Q is to be chosen such that:

$$\zeta_1(\eta_\infty, Q) = 0.$$

The above equation can be solved by using Newton's method with the following iterative formula:

$$Q_{n+1} = Q_n - \frac{\zeta_1(\eta_\infty, Q_n)}{\left(\frac{\partial\zeta_1}{\partial Q}(\eta_\infty, Q)\right)_{Q=Q_n}}. \tag{4.32}$$

The following notations are further introduced:

$$\frac{\partial\zeta_1}{\partial Q} = \zeta_3, \qquad \frac{\partial\zeta_2}{\partial Q} = \zeta_4.$$

The Newton's iterative scheme (4.32) takes the form:

$$Q_{n+1} = Q_n - \frac{\zeta_1(\eta_\infty, Q_n)}{\zeta_3(\eta_\infty, Q_n)}.$$

Now, differentiating the last system of two first-order ODEs with respect to Q, another system of ODEs is obtained as follows:

$$\zeta_3' = \zeta_4, \qquad \zeta_3(0) = 1.$$

$$\zeta_4' = \frac{Pr}{P_4 + \frac{4N}{3}}\left[\frac{-1}{Pr}\left(\frac{P_1P_4}{P_2}\right)B_1\zeta_3 + P_5(U_P\frac{\eta}{2}\zeta_4 - \tau_1\zeta_4)\right], \qquad \zeta_4(0) = \frac{B_i}{P_4}.$$

The stopping criterion for Newton's method is set as:

$$|\zeta_1(\eta_\infty, Q)| < \epsilon.$$

The following notations have been used as initial step to solve dimensionless form of diffusion equation:

$$\phi = \omega_1, \qquad \phi' = \omega_1' = \omega_2, \qquad \phi'' = \omega_2''.$$

The non-dimensionalised diffusion equation (4.30) is then transformed into system of ODEs as follows:

$$\omega_1' = \omega_2 \qquad \omega_1(0) = 1,$$

$$\omega_2' = \frac{1}{P_6}\left(CrSc(\delta\zeta_1 + 1)\exp\left(\frac{-E}{\delta\zeta_1 + 1}\right)\omega_1 - Sc\left(\tau_1\omega_2 - U_P\frac{\eta}{2}\omega_2\right)\right), \quad \omega_2(0) = R.$$

The aforementioned IVP is solved numerically using the Runge-Kutta method of order 4. The missing condition R is to be chosen such that:

$$\omega_2(\eta_\infty, R) = 0.$$

Newton-Raphson method will be used to update the missing condition R, using iterative scheme:

$$R_{n+1} = R_n - \frac{\omega_2(\eta_\infty, R_n)}{\left(\frac{\partial}{\partial R}\omega_2(\eta_\infty, R)\right)} \tag{4.33}$$

The following notations are further introduced:

$$\frac{\partial\omega_1}{\partial R} = \omega_3, \qquad \frac{\partial\omega_2}{\partial R} = \omega_4.$$

The Newton's iterative scheme (4.33) takes the form:

$$R_{n+1} = R_n - \frac{\omega_2(\eta_\infty, R_n)}{\omega_4(\eta_\infty, R_n)}.$$

Now, differentiating the last system of two first order ordinary differential equations with respect to R, another system of ODEs is obtained as follows:

$$\omega_3' = \omega_4, \qquad \omega_3(0) = 0,$$

$$\omega_4' = \frac{1}{P_6}\left(CrSc(\delta\zeta_1 + 1)\exp(\frac{-E}{\delta\zeta_1 + 1})\omega_1 - Sc(\tau_1\omega_4 - U_P\frac{\eta}{2}\omega_4)\right) \qquad \omega_4(0) = 1.$$

The stopping criterion for Newton's method is set as:

$$|\omega_2(\eta_\infty, R)| < \epsilon.$$

4.5 Results Interpretation

This section evaluates the physical characteristics of the velocity, thermal and concentration profiles with respect to variations in key physical parameters. The analysis is carried out through graphical representations of these profiles, while the effects of dimensionless parameters on quantities such as skin friction, Nusselt number and Sherwood number are further examined and summarized in tabular form.

These graphical results provide clear insights into the system's behavior under varying parameter values, enabling a deeper understanding of how changes in the velocity, temperature and concentration profiles reflect the underlying physical mechanisms.

4.5.1 Analysis of Computational Results

Table 4.1 shows the results of skin friction coefficient for the $CuO - Ag/$ Ethylene Glycol-H_2O hybrid nanofluid, considering different inputs of M, γ, S, L, k_1, U_P, ϕ_{CuO} and ϕ_{Ag}. The findings reveal that rise in the values of M and γ leads to a decline in absolute values of local skin friction coefficients, indicating a decrease in the fluid velocity. The Lorentz force acts like a dragging or resistive force opposing the fluid motion due to increasing values of Hartmann number M. So, velocity decreases because the magnetic field is suppressing the fluid flow.

It is analyzed that as the values for angle of inclination γ become higher, more opposition to the fluid motion is introduced, leading to a drop in velocity.

In the similar manner, an increase in the values of the suction parameter S and slip parameter L results a decrease in fluid flow. The velocity profile is suppressed and boundary layer becomes thinner as the values of suction parameter S are gradually increased. Meanwhile, higher values of slip parameter L reduces the momentum transfer between sheet and the fluid.

Increasing porous media effect k_1 reduces the fluid velocity and skin friction, leading to a suppressed velocity profile and a thinner boundary layer due to the stronger resistance offered by the porous medium. An increase in the unsteadiness parameter U_P results in a noticeable decline in the skin friction coefficient. Also, rise in amount of volume fractions of ϕ_{CuO} and ϕ_{Ag} shows decline in skin friction coefficient.

Table 4.2 shows how variation of several non-dimensionalised parameters e.g. Prandtl number, radiation coefficient, space dependent internal heat generation coefficient and time dependent internal heat absorption coefficient affect values of Nusselt number. A rise in the Prandtl number Pr results in increasing Nusselt number because higher Pr corresponds to smaller values of thermal diffusivity, which strengthens the thermal gradient near the surface. This results in more effective convective heat transfer, thereby raising the heat transfer rate from the surface to the fluid. The higher values of radiation parameter N enhance the Nusselt number because stronger thermal radiation promotes additional heat transfer from the surface. This intensifies the thermal gradient at the sheet, resulting in improved convective heat transfer performance and thus higher Nusselt number values.

Furthermore, an increase in the space-dependent internal heat generation coefficient A_1 leads to a decline in the Nusselt number. This is because stronger internal heat generation introduces excess thermal energy into the fluid, which results in decreasing temperature gradient at the surface. As a result, the effectiveness of convective heat transfer diminishes, lowering the Nusselt number values. Similarly, higher values of the time-dependent internal heat absorption coefficient B_1 result in an increase in the fluid temperature. This occurs because stronger heat absorption adds additional thermal energy to the system, allowing the temperature within boundary layer to rise.

It is noted that increasing the Hartmann number M shows a reduction in the Nusselt number. The presence of a stronger magnetic field generates a Lorentz force that resists fluid motion thereby, lowering the convective heat transfer rate and reducing the Nusselt number. By escalating values of Eckert number Ec an

increase in Nusselt number is observed.This is because higher Ec signifies stronger viscous dissipation, which converts more kinetic energy of the fluid into internal energy. As a result, the enhanced thermal energy intensifies the temperature gradients near the surface, thereby rising the convective heat transfer rate.

TABLE 4.1: Thermophysical characteristics of base fluid (50 percent Water+50 percent Eythlene Glycol) and nanoparticles CuO and Ag

Thermophysical properties	WEG	CuO	Ag
ρ/kgm^{-1}	1056	6500	10,500
$C_P/Jkg^{-1}K^{-1}$	3288	525.6	235
$\kappa/Wm^{-1}K^{-1}$	0.4250	20	429
σ/Sm^{-1}	0.00509	$5.96 * 10^7$	$3.5 * 10^6$

More the medium under consideration is porous, less value of Nusselt number is obtained due to porous media effect k_1. The higher resistance offered by the porous structure suppresses fluid motion and weakens convective transport resulting in smaller values of Nusselt number. The increasing values of unsteadiness parameter U_P result a reduction in the Nusselt number. This behavior arises because enhanced unsteady effects reduce the surface heat transfer rate by enlarging the thermal boundary layer and lowering the wall temperature gradient.

Table 4.3 shows how Sherwood number is affected due to different parameters. It is found that higher values of the unsteadiness parameter U_P cause a decline in the Sherwood number. This behavior arises because stronger unsteady effects thicken the concentration boundary layer, thereby reducing the surface concentration gradient and weakening mass transfer. It is also analyzed that higher values of the Schmidt number Sc show a corresponding rise in the Sherwood number. A higher Sc indicates lower mass diffusivity, which sharpens the concentration gradient at the surface. This steeper gradient enhances the mass transfer rate. The analysis shows that enhancing values of the chemical reaction parameter Cr lead to an

enhancement in the Sherwood number. This implies that stronger chemical reactions intensify the rate of species consumption within the boundary layer. As a result, the concentration boundary layer turns thinner and the wall concentration gradient increases, thereby improving the overall mass transfer rate at the surface. Moreover, it is evident that bigger the values of parameter δ provide bigger values of the Sherwood number. This behavior indicates that larger values of δ enhance the mass transfer process by enhancing the concentration gradient at the sheet, which as a result, raises the rate of species transport from the surface.

TABLE 4.2: The results of the skin friction coefficient $C_f\sqrt{Re_x}$ and interval of convergence I_s for values of M, γ, S, L, k_1, U_P, ϕ_{CuO} and ϕ_{Ag}.

M	γ	S	L	k_1	U_P	ϕ_{CuO}	ϕ_{Ag}	$C_f\sqrt{Re_x}$	I_s
0.5	0	0.5	0.3	1	0.05	0.01	0.01	0.62276	[-1.2,5.5]
1								0.62276	[-1.2,5.5]
1.5								0.62276	[-1.2,5.5]
2								0.62276	[-1.2,5.5]
	$\pi/6$							0.62274	[-1.3,5.3]
	$\pi/4$							0.62271	[-1.3,5.1]
	$\pi/2$							0.62267	[-1.4,4.8]
		1						1.24259	[-1.6,6.8]
		1.5						1.86242	[-1.9,8.1]
		2						2.48227	[-2.3,9.4]
			0.5					0.62229	[-1.1,4.2]
			0.7					0.62197	[-0.8,3.4]
			0.9					0.62173	[-0.7,2.8]
				1.5				0.62267	[-1.3,4.2]
				2				0.62260	[-1.4,4.1]
				2.5				0.62253	[-1.4,3.5]
					0.15			0.62275	[-1.2,4.9]
					0.20			0.62274	[-1.2,4.3]
					0.25			0.62273	[-1.2,3.1]
						0.02		0.61140	[-1.2,3.0]
						0.03		0.60151	[-1.2,3.0]
						0.04		0.59294	[-1.2,3.0]
							0.02	0.56321	[-1.2,2.8]
							0.03	0.51190	[-1.2,2.6]
							0.04	0.46726	[-1.4,2.4]

TABLE 4.3: The results of the local Nusselt number $\frac{Nu_x}{\sqrt{Re_x}}$ for values of Pr, N, A_1, B_1, M, Ec, k_1 and U_P.

Pr	N	A_1	B_1	M	Ec	k_1	U_P	Nu
4	1	0.1	0.1	0.1	0.2	0.3	0.05	0.45714
5								0.47507
6								0.48749
7								0.49660
	1.5							0.56213
	2							0.65975
	2.5							0.75185
		0.2						0.44686
		0.3						0.43658
		0.4						0.42630
			0.2					0.45076
			0.3					0.44376
			0.4					0.43602
				0.2				0.45441
				0.3				0.45168
				0.4				0.44895
					0.4			0.40511
					0.6			0.35308
					0.8			0.30105
						0.5		0.43295
						0.7		0.41166
						1		0.38393
							0.10	0.45200
							0.15	0.44615
							0.20	0.43940

TABLE 4.4: The results of the Sherwood number Sh for values of U_P, E, Sc, Cr and δ.

U_P	E	Sc	Cr	δ	Sh
0.05	0.1	1	1	0.5	1.43151
0.10					1.42478
0.15					1.41829
0.20					1.41212
	0.2				1.39161
	0.3				1.35376
	0.4				1.31790
		2			2.25639
		3			2.97936
		4			3.65122
			2		1.82531
			3		2.13897
			4		2.40771
				1	1.48490
				1.5	1.53710
				2	1.58810

4.5.2 Analysis of Graphical Results

4.5.3 Velocity Field

Figure 4.2 elaborates the impact of Hartmann number variation on the fluid velocity. Higher values of M lead to a decline in the fluid velocity and compression

of the momentum boundary layer. This trend is primarily due to the strengthening of the imposed magnetic field, which enhances the Lorentz force acting as a resistive force against the fluid motion. Figure 4.3 presents the influence of the inclination angle γ of the magnetic field on the momentum profile. It is observed that fluid velocity increases as γ decreases, indicating that a larger inclination angle enhances the magnetic resistance to the fluid flow.

The thickness of the momentum boundary layer with different values of suction parameter S is described in Figure 4.4. The velocity distribution within the boundary layer is reduced due to gradually increasing values of S, resulting in reduced fluid motion and a corresponding decline in the boundary layer thickness. As a result, the boundary layer thickness turns thinner, and the overall velocity distribution across the layer decreases. The behavior of escalating values of velocity slip parameter L resulting into declining values of fluid flow is observed in Figure 4.5. This results into momentum boundary layer becoming thinner.

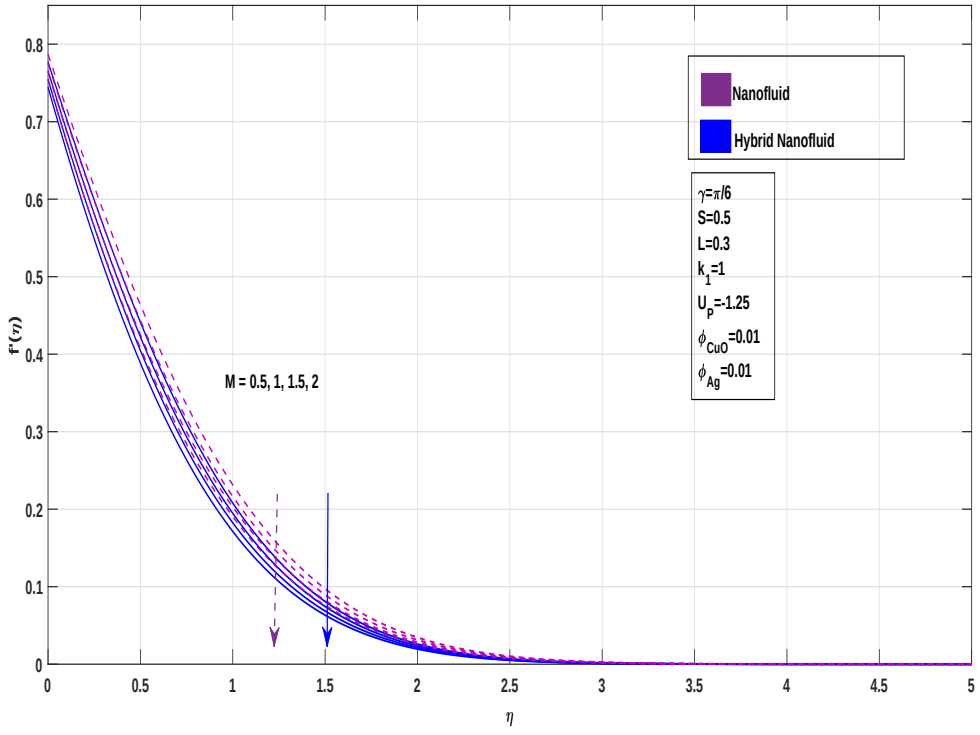

FIGURE 4.2: Impact of M on velocity profile

Figure 4.6 illustrates the impact of porous medium parameter k_1 on the velocity distribution. With increasing resistance, the motion of the fluid is significantly hindered, leading to lower flow intensity. As the speed diminishes, penetration away from the sheet becomes limited, producing a thinner momentum boundary layer. From a physical perspective, the drag introduced by the porous structure enforces this reduction in flow strength. Furthermore, it is observed from Figure 4.7 that higher values of the unsteadiness parameter U_P cause a reduction in the fluid velocity. This behavior may be attributed to the fact that larger values of U_P enhance the unsteady effects, which suppress the development of the boundary layer and consequently reduce the momentum transport. The impact of volume fraction of ϕ_{CuO} on velocity profile can be viewed via Figure 4.8. An increase in volume fraction results in increasing density of the fluid, hence a decrease in the fluid flow. An increase in the nanoparticle volume fraction enhances the effective viscosity of the suspension, which in turn suppresses fluid motion. Consequently, the velocity profile exhibits a noticeable reduction and the momentum boundary layer becomes thinner as the fluid's capacity to move away from the surface is reduced.

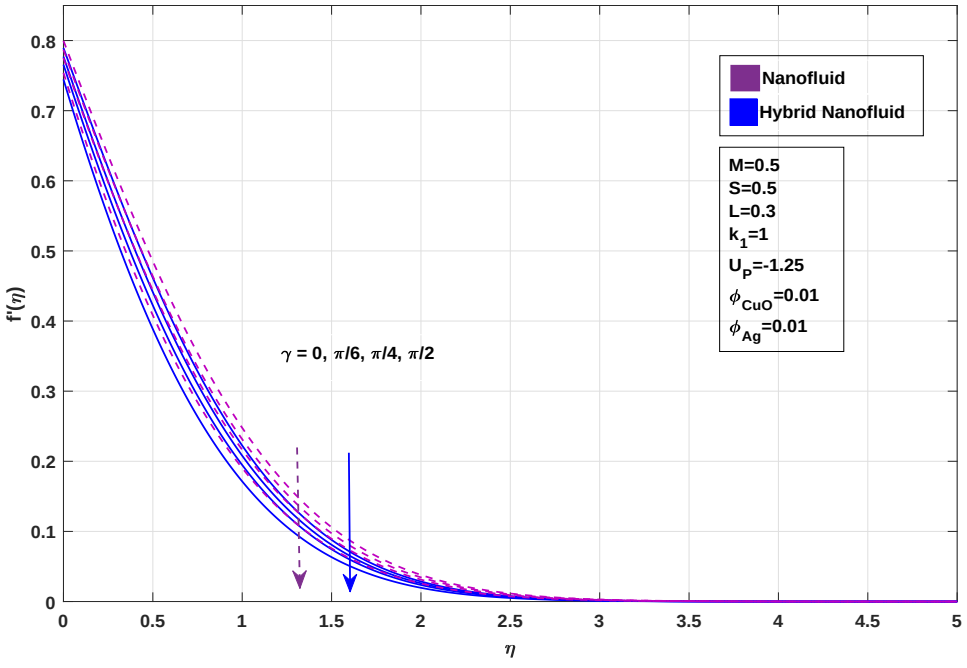

FIGURE 4.3: Impact of γ on velocity profile

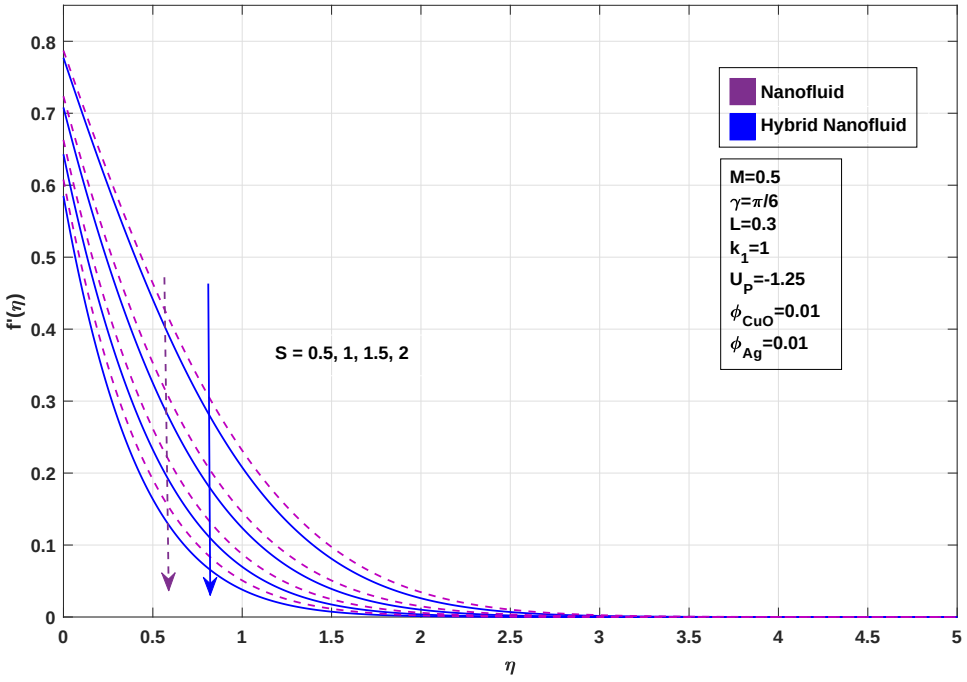

FIGURE 4.4: Impact of S on velocity profile

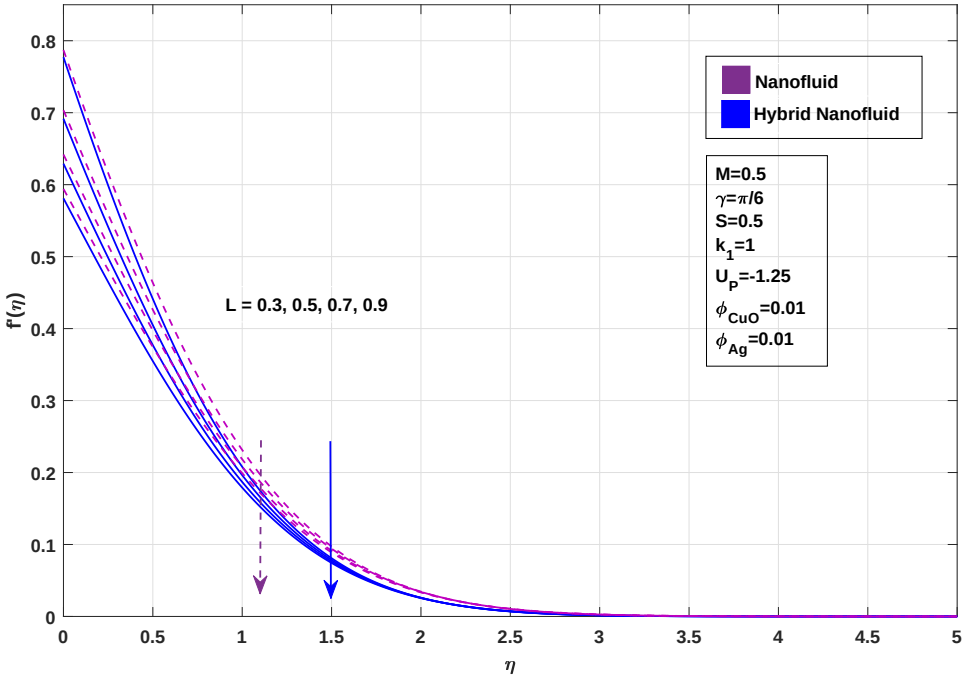

FIGURE 4.5: Impact of L on velocity profile

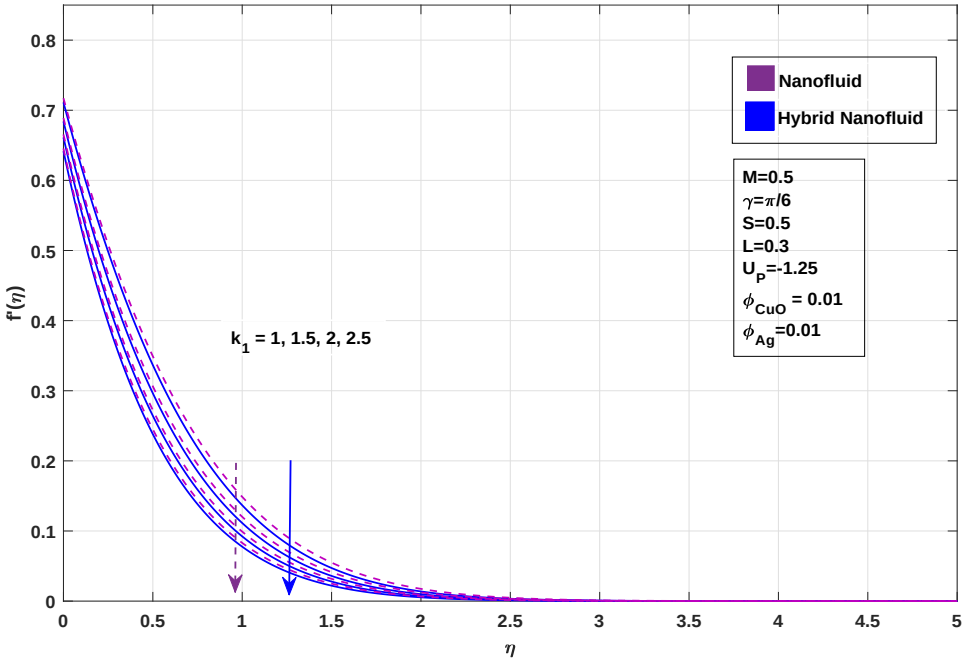

FIGURE 4.6: Impact of k_1 on velocity profile

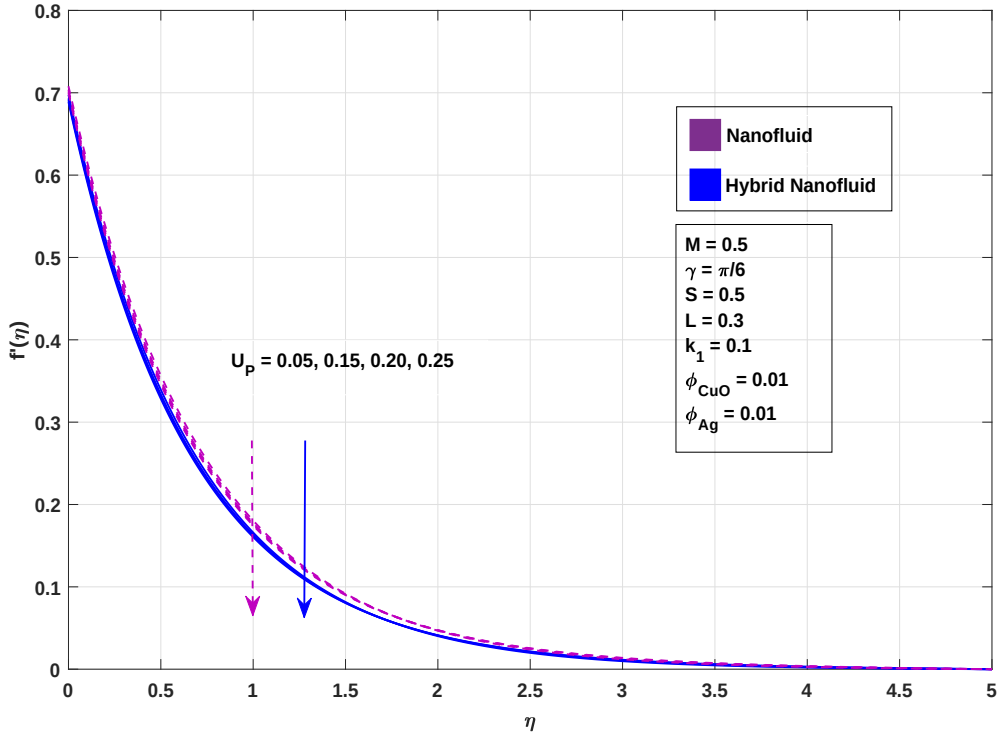

FIGURE 4.7: Impact of U_P on velocity profile

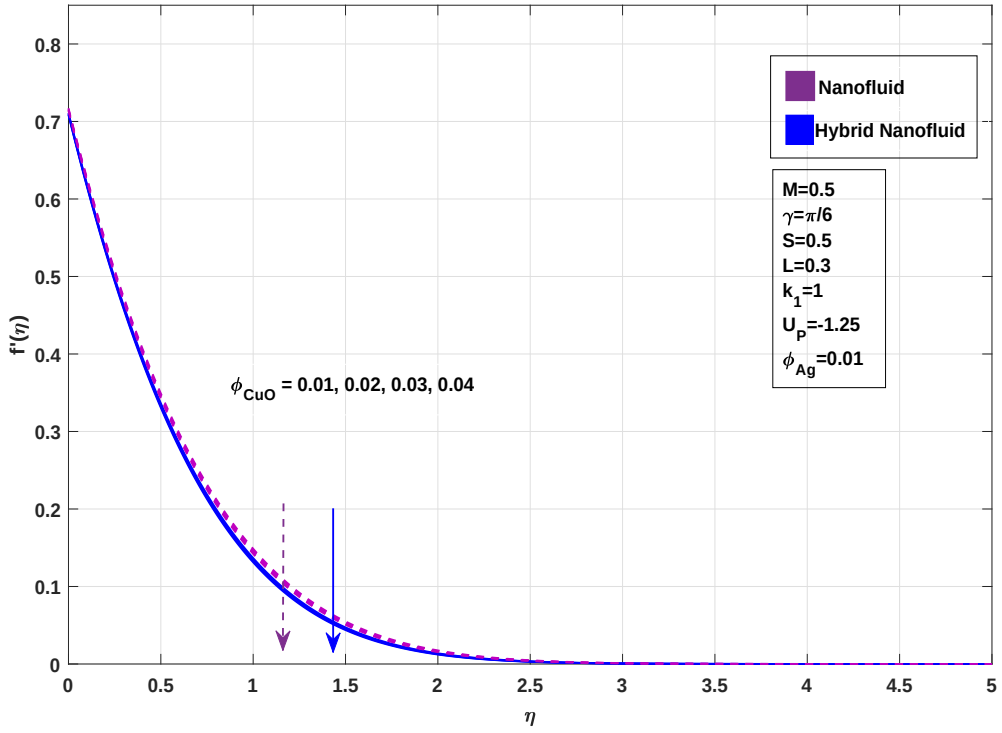

FIGURE 4.8: Impact of ϕ_{CuO} on velocity profile

4.5.4 Thermal Field

Figure 4.9 depicts that higher values of Prandtl number reduce the thermal diffusivity of the fluid, which lowers the temperature distribution within the boundary layer and consequently leads to a thinner thermal boundary layer and a decrease in temperature of the fluid. Influence of altered radiation parameter values N on thermal boundary layer thickness is shown in Figure 4.10. An increase in N enhances radiative energy transfer, which consequently raises the fluid temperature. The thermal boundary layer turns thicker, since higher radiation supplies more energy, allowing heat to penetrate deeper into the fluid. This results in a slower decay of temperature away from the stretching sheet.

Figure 4.11 elaborates that an increase in the space-dependent heat sink parameter A_1 leads to a decrease in the fluid temperature. This behavior arises because larger values of A_1 correspond to a stronger heat sink effect, which extracts thermal

energy from the boundary layer. Consequently, the fluid temperature is reduced and the thickness of the thermal boundary layer decreases.

Meanwhile, Figure 4.12 depicts that a rise in the temperature-dependent heat source parameter B_1 leads to an elevation in the fluid temperature. This occurs because higher values of B_1 strengthen the internal heat generation within the fluid, thereby increasing the thermal energy content. As a consequence, the thermal boundary layer turns thicker, resulting in a rise in the temperature profile.

An increase in values of M, the Hartmann number, results an increase in temperature of fluid is elaborated in Figure 4.13. When velocity is suppressed by the magnetic field, fluid layers move more slowly. As a result, the fluid temperature increases with increase in values of the Hartmann number M. Due to the additional heat generated by viscous dissipation, the fluid preserves more thermal energy, allowing heat to diffuse far from the surface. Consequently, the thermal boundary layer turns thicker, as the region affected by temperature extends deeper into the fluid domain. Figure 4.14 illustrates that higher values of the Eckert number intensify viscous dissipation within the flow, which converts a portion of the kinetic energy into internal energy. This additional heating effect raises the fluid temperature throughout the boundary layer.

Figure 4.15 demonstrates that when the porous medium effect is intensified, the flow experiences stronger drag, which suppresses the fluid motion. This resistance increases internal friction and enhances the conversion of mechanical energy into heat, resulting an increase in the fluid temperature. As a consequence, the thermal profile shifts upward, showing higher temperature values across the boundary layer. Moreover, the thermal boundary layer turns thicker, since the additional heat diffuses far into the fluid domain, extending the region influenced by temperature variations.

It is observed in Figure 4.16 that an increase in the unsteadiness parameter U_P leads to a rise in the fluid temperature. This is due to the fact that higher unsteadiness strengthens the transient effects within the thermal boundary layer. Consequently, the fluid retains more heat, resulting in an elevation of the thermal profile and increase in the thickness of thermal boundary layer.

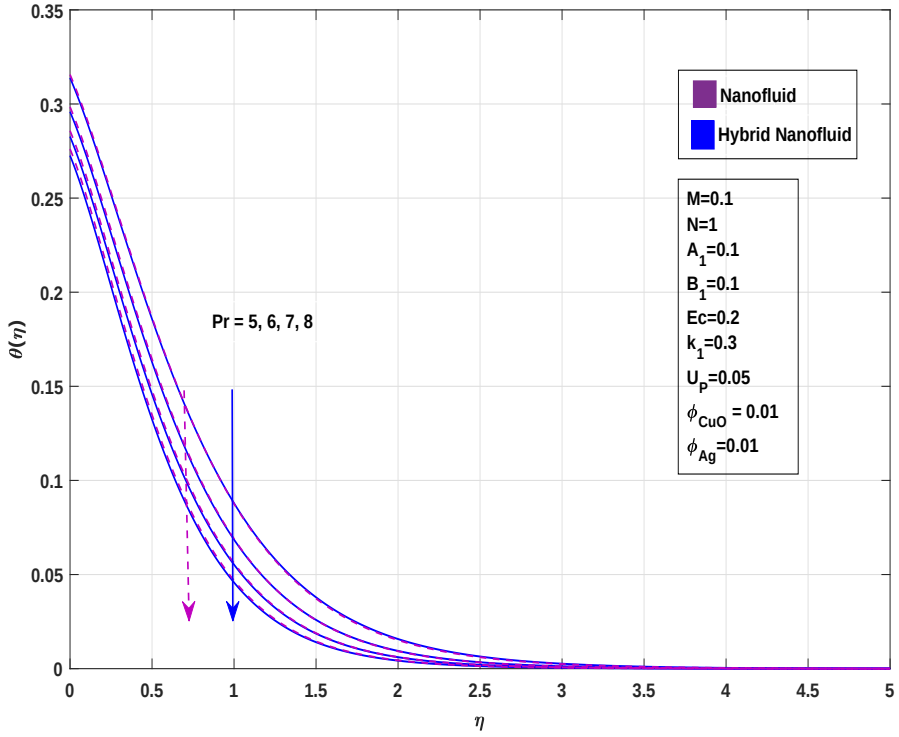

FIGURE 4.9: Impact of Pr on temperature profile

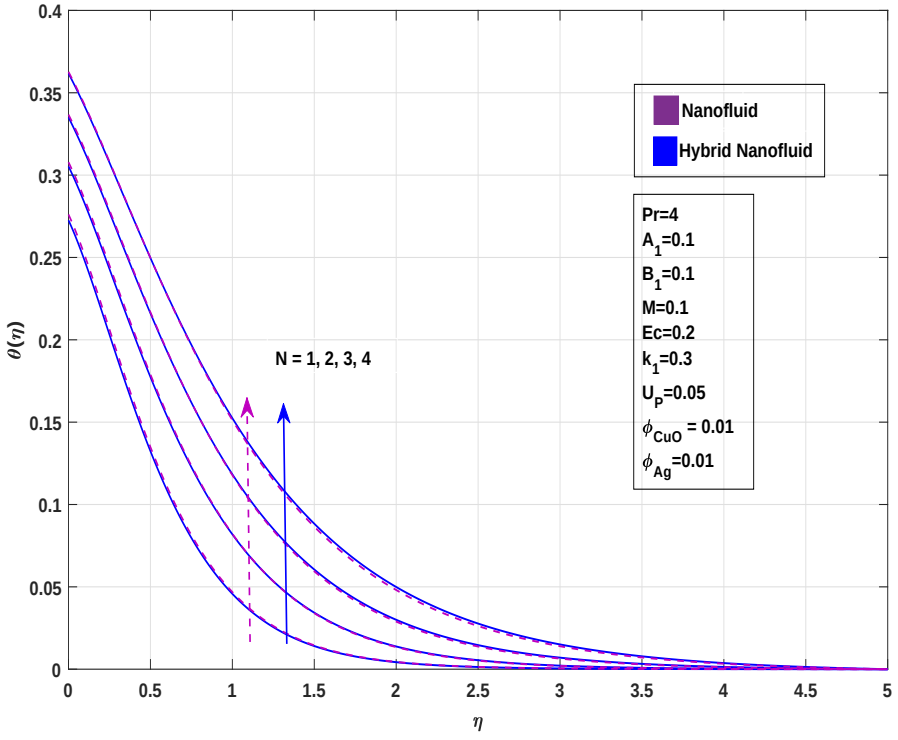

FIGURE 4.10: Impact of N on temperature profile

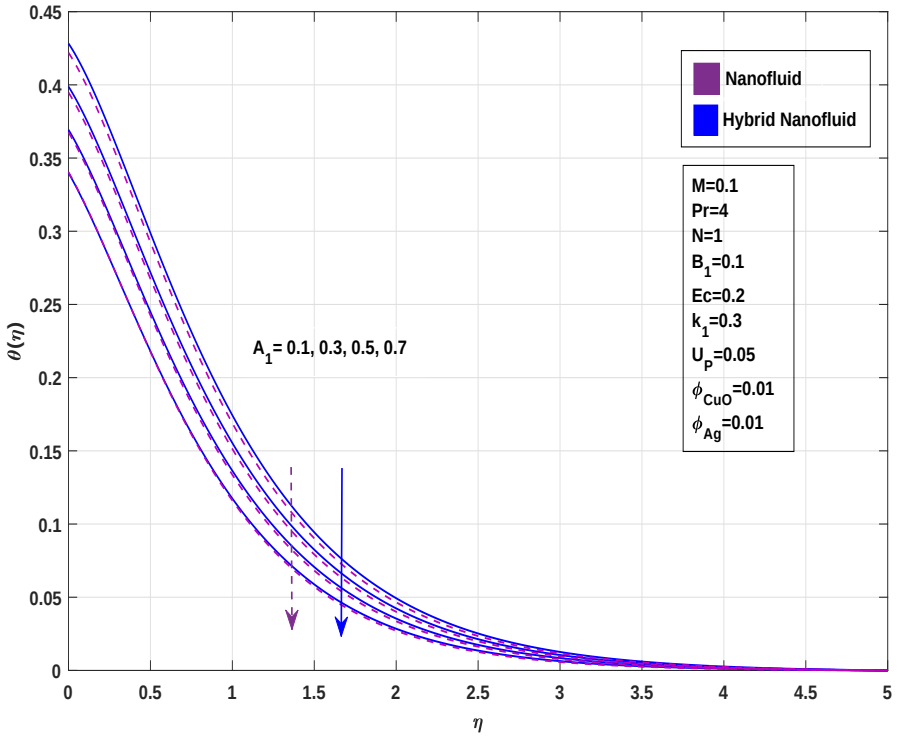

FIGURE 4.11: Impact of A_1 on temperature profile

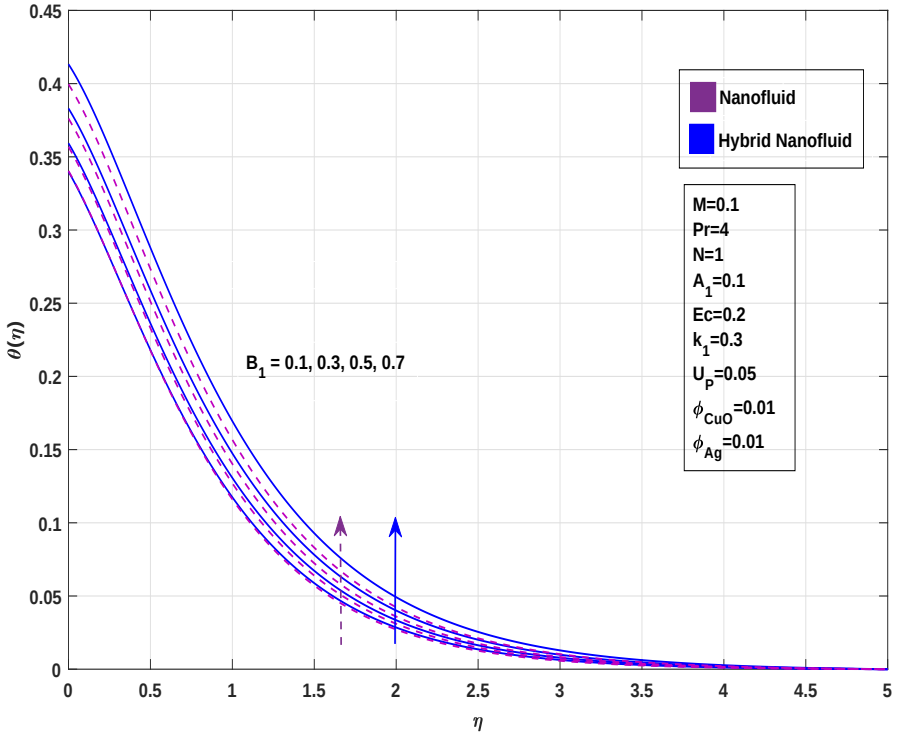

FIGURE 4.12: Impact of B_1 on temperature profile

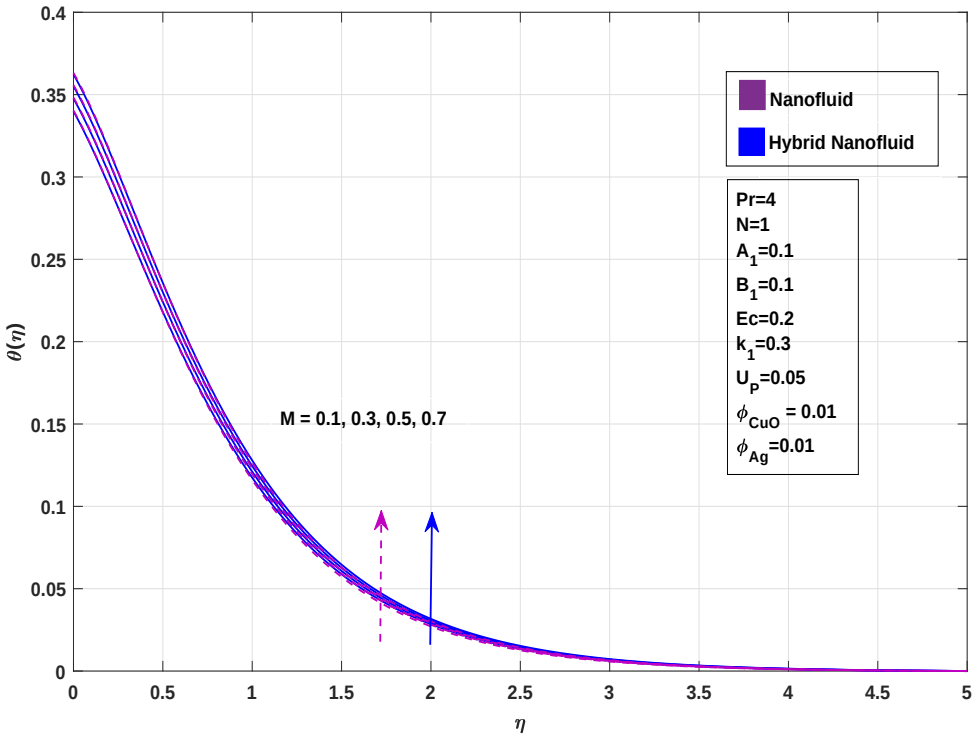

FIGURE 4.13: Impact of M on temperature profile

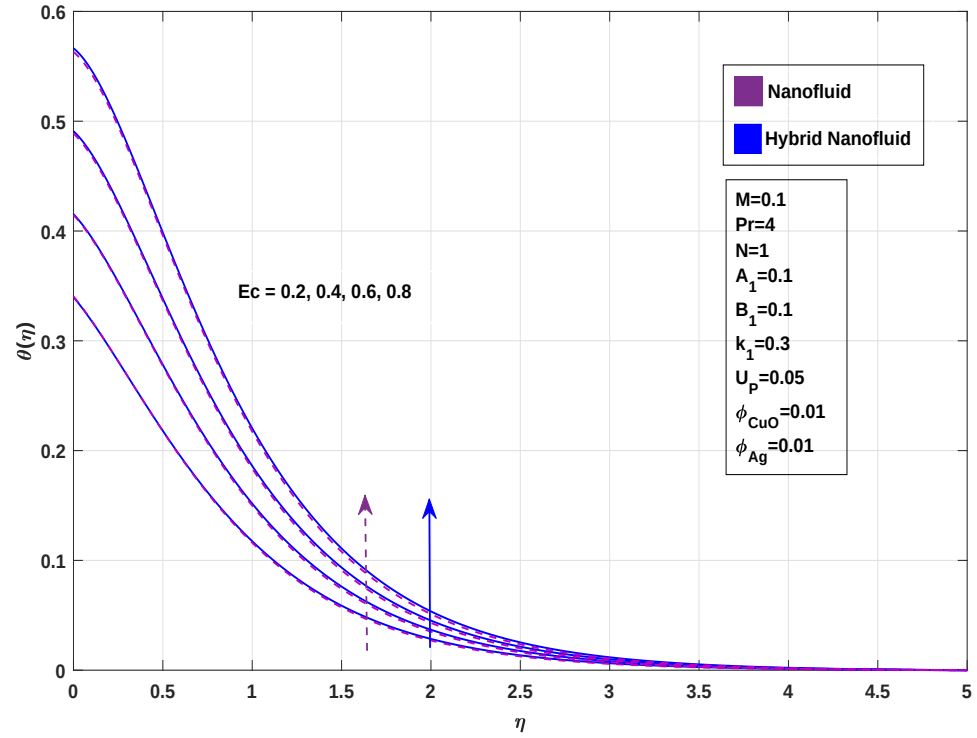

FIGURE 4.14: Impact of Ec on temperature profile

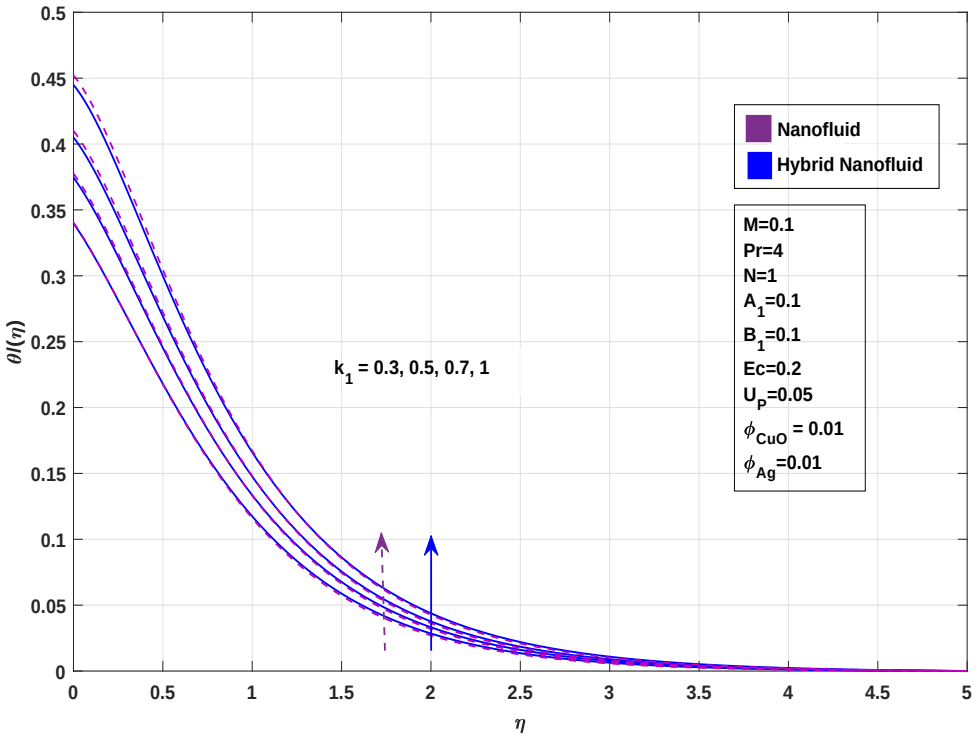

FIGURE 4.15: Impact of k_1 on temperature profile

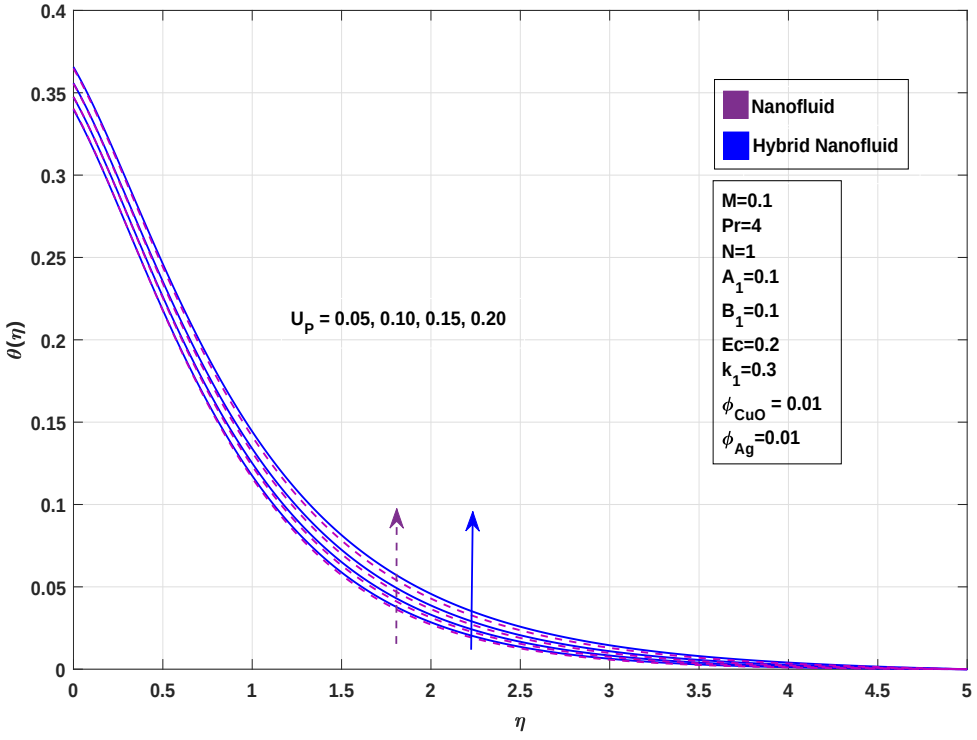

FIGURE 4.16: Impact of U_P on temperature profile

4.5.5 Concentration Field

As demonstrated in Figure 4.16 a rise in the values of the unsteadiness parameter U_P results in an enhancement of the concentration profile. Physically, this occurs because greater unsteadiness reduces the rate of mass diffusion, thereby allowing the solute species to accumulate in the boundary layer region. As a result, the concentration boundary layer is thickened and the overall concentration distribution increases.

Figure 4.17 indicates that higher values of the activation energy parameter E result in higher concentration values. Physically, this behavior can be elaborated in the way that larger activation energy weakens the chemical reaction process, thereby reducing the consumption of species. Consequently, more solute remains in the fluid, which enhances the concentration profile and thickens the concentration boundary layer.

The graphical results from Figure 4.18 indicate that increasing values of the Schmidt number result into a reduction in the concentration profile within the boundary layer. Physically, this behavior is due to the fact that a higher Schmidt number corresponds to a lower mass diffusivity relative to momentum diffusivity. As a result, species diffusion in the fluid is suppressed, causing the solute concentration to decay more rapidly from the wall towards the free stream. Accordingly, the thickness of the concentration boundary layer decreases and the overall mass transfer rate is diminished. This demonstrates that fluids with higher Schmidt numbers exhibit weaker species diffusion compared to those with lower Schmidt numbers.

The results in Figure 4.19 show that increasing values of the chemical reaction parameter Cr lead to a reduction in the concentration profile. Physically, this happens due to the fact that a higher value of Cr corresponds to a more intense reactive process, which accelerates the consumption of the species within the boundary layer. Consequently, the diffusion of mass is suppressed, producing lower concentration values and a compressed concentration profile. Furthermore, Figure 4.20 shows that a rise in the temperature difference parameter δ shows

a noticeable reduction in the concentration distribution. Physically, it explains that by higher values of δ reaction rate is enhanced, hence results into decrease in concentration profile.

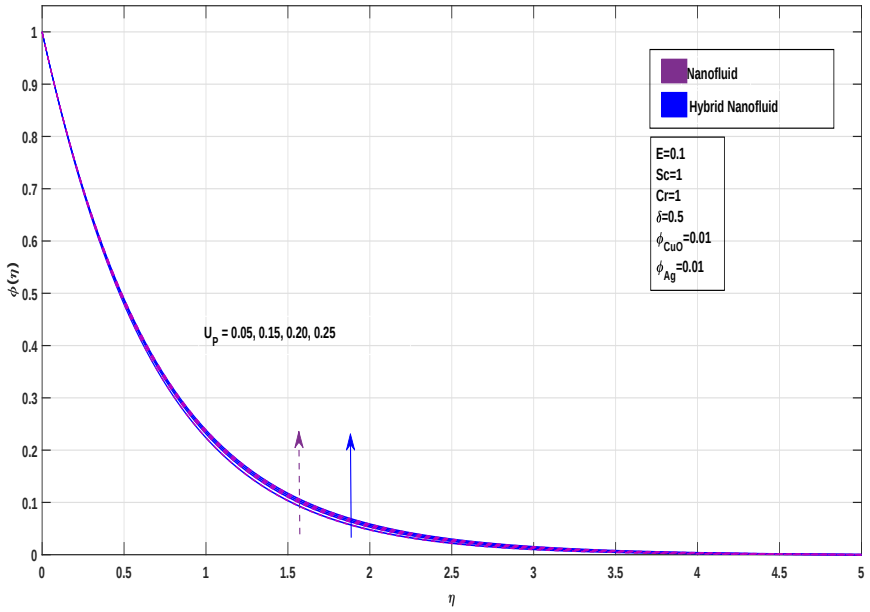

FIGURE 4.17: Impact of U_P on concentration profile

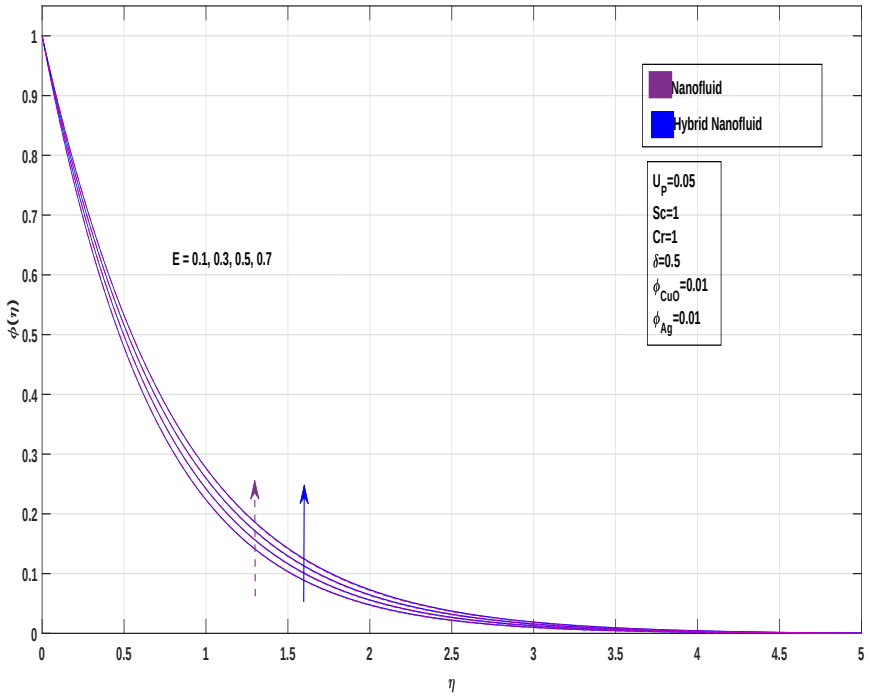

FIGURE 4.18: Impact of E on concentration profile

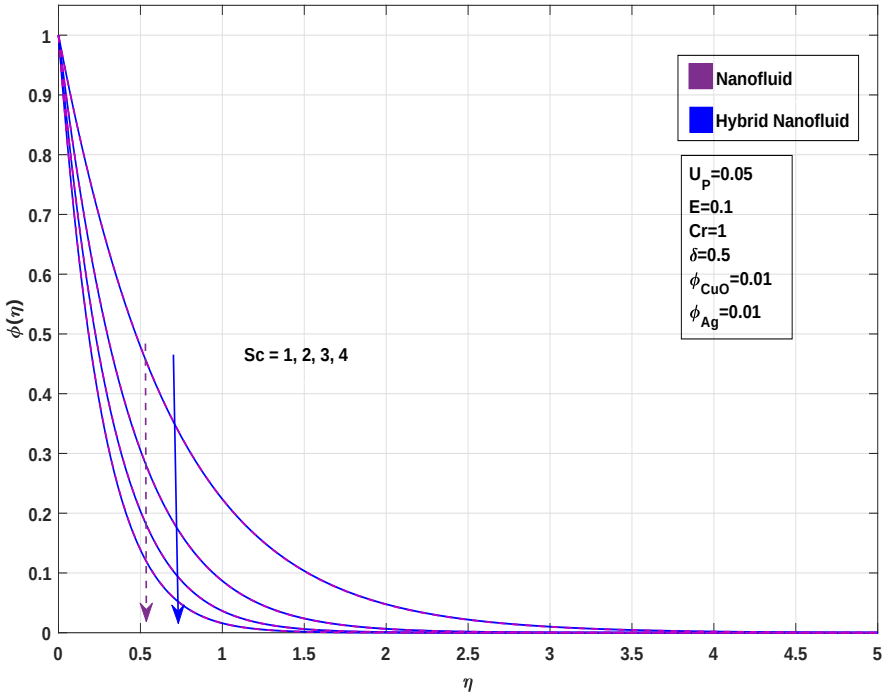

FIGURE 4.19: Impact of Sc on concentration profile

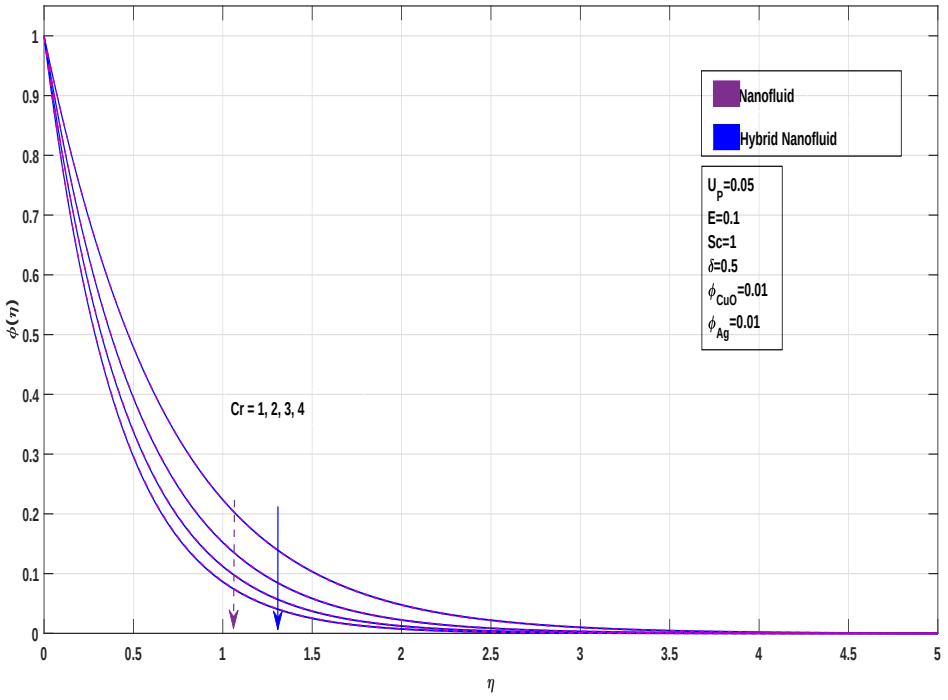

FIGURE 4.20: Impact of Cr on concentration profile

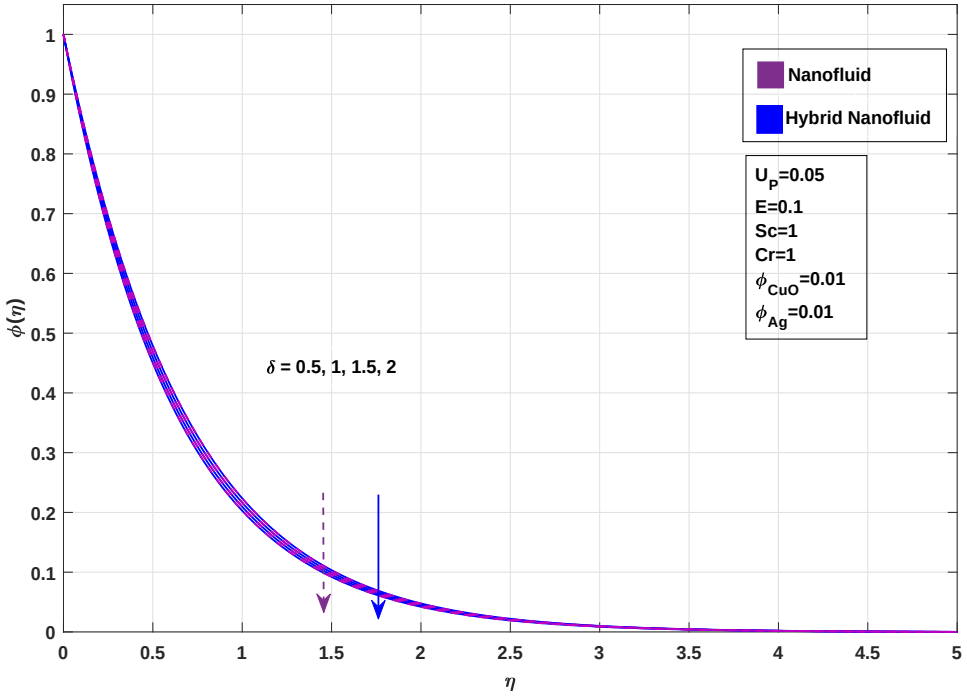

FIGURE 4.21: Impact of δ on concentration profile

Chapter 5

Conclusion

A detailed investigation is performed in this thesis to assess the effects of multiple physical parameters on the velocity, temperature, and concentration fields of nanoparticles suspended in two working fluids: the nanofluid CuO and the hybrid nanofluid $CuO - Ag$. The analysis incorporated several dimensionless quantities, including the Hartmann number M, inclination angle γ, suction parameter S, velocity slip factor L, porous medium parameter k_1, unsteadiness parameter U_P, radiation parameter N, Prandtl number Pr, heat sink coefficient A_1, heat source coefficient B_1, Eckert number Ec, activation energy E, Schmidt number Sc, chemical reaction parameter Cr and the temperature difference parameter δ.

(i) Suction parameter (S) and inclination angle (γ) inversely affect the fluid velocity, leading to reduced flow rates. Magnetic field parameter namely Hartmann number (M) caused a decrease in the fluid velocity due to Lorentz force.
(ii) An increment in the velocity slip parameter (L) and porous medium parameter (k_1) lead to a decay in the velocity field. For higher values of unsteadiness parameter (U_P), a decline in velocity profile is observed.
(iii) For the positive variation in thermal radiation parameter (N), heat source parameter (B_1) and Eckert number (Ec) temperature profile is observed rising. Meanwhile, with the similar pattern of increasing Prandtl number (Pr) and heat sink parameter (A_1) thermal profile shows a decline.

(iv) The concentration profile is influenced by the temperature difference parameter (δ), resulting in a reduction in the concentration.

(v) Chemical reaction parameter (Cr) and Schmidt number (Sc), lead to a decrease in the nanoparticle concentration.

Bibliography

[1] S. U. Choi, "Enhancing thermal conductivity of fluids with nanoparticles," in *ASME international mechanical engineering congress and exposition*, vol. 17421, pp. 99–105, American Society of Mechanical Engineers, 1995.

[2] J. A. Eastman, U. Choi, S. Li, L. Thompson, and S. Lee, "Enhanced thermal conductivity through the development of nanofluids," *MRS Online Proceedings Library (OPL)*, vol. 457, p. 3, 1996.

[3] Y. Xuan and Q. Li, "Heat transfer enhancement of nanofluids," *International Journal of Heat and Fluid Flow*, vol. 21, no. 1, pp. 58–64, 2000.

[4] S. Yang, J. Lin, Z. Zhang, C. Zhang, X. Zheng, W. Xie, L. Wang, S. Chen, and X. Liu, "Advanced engineering materials for enhancing thermal management and thermal safety of lithium-ion batteries: A review," *Frontiers in Energy Research*, vol. 10, p. 949760, 2022.

[5] Q. Tao, F. Zhong, Y. Deng, Y. Wang, and C. Su, "A review of nanofluids as coolants for thermal management systems in fuel cell vehicles," *Nanomaterials*, vol. 13, no. 21, p. 2861, 2023.

[6] M. A. Rahman, S. M. Hasnain, S. Pandey, A. Tapalova, N. Akylbekov, and R. Zairov, "Review on nanofluids: preparation, properties, stability, and thermal performance augmentation in heat transfer applications," *ACS Omega*, vol. 9, no. 30, pp. 32328–32349, 2024.

[7] S. Zhang, L. Lu, T. Wen, and C. Dong, "Turbulent heat transfer and flow analysis of hybrid $Al_2O_3 - CuO$/water nanofluid: An experiment and CFD simulation study," *Applied Thermal Engineering*, vol. 188, p. 116589, 2021.

[8] S. Alabdulhadi, I. Waini, S. E. Ahmed, and A. Ishak, "Hybrid nanofluid flow and heat transfer past an inclined surface," *Mathematics*, vol. 9, no. 24, p. 3176, 2021.

[9] O. A. Alawi, H. M. Kamar, O. A. Hussein, A. Mallah, H. A. Mohammed, M. Khiadani, A. B. Roomi, S. Kazi, and Z. M. Yaseen, "Effects of binary hybrid nanofluid on heat transfer and fluid flow in a triangular-corrugated channel: An experimental and numerical study," *Powder Technology*, vol. 395, pp. 267–279, 2022.

[10] J. Wohld, J. Beck, K. Inman, M. Palmer, M. Cummings, R. Fulmer, and S. Vafaei, "Hybrid nanofluid thermal conductivity and optimization: Original approach and background. nanomaterials 2022, 12, 2847," 2022.

[11] A. M. Alqahtani, B. Ullah, B. Ahmad, U. Khan, H. A. Wahab, and R. Alroobaea, "Thermal analysis of micropolar hybrid nanofluid inspired by 3D stretchable surface in porous media," *Nanoscale Advances*, vol. 5, no. 22, pp. 6216–6227, 2023.

[12] K. R. Kumar and A. H. Shaik, "Synthesis, thermophysical characterization and thermal performance analysis of novel Cu-MXene hybrid nanofluids for efficient coolant applications," *RSC advances*, vol. 13, no. 42, pp. 29536–29560, 2023.

[13] R. Al Mezrakchi, "Investigation of various hybrid nanofluids to enhance the performance of a shell and tube heat exchanger.," *AIMS Energy*, vol. 12, no. 1, 2024.

[14] P. K. Das, A. K. Santra, R. Ganguly, S. K. Dash, S. Muthusamy, M. Sha, and K. K. Sadasivuni, "An extensive review of preparation, stabilization, and application of single and hybrid nanofluids," *Journal of Thermal Analysis and Calorimetry*, vol. 149, no. 17, pp. 9523–9557, 2024.

[15] B. Ali, R. A. Naqvi, Y. Nie, S. A. Khan, M. T. Sadiq, A. U. Rehman, and S. Abdal, "Variable viscosity effects on unsteady MHD an axisymmetric nanofluid flow over a stretching surface with thermo-diffusion: Fem approach," *Symmetry*, vol. 12, no. 2, p. 234, 2020.

[16] A. M. Sedki, S. Abo-Dahab, J. Bouslimi, and K. Mahmoud, "Thermal radiation effect on unsteady mixed convection boundary layer flow and heat transfer of nanofluid over permeable stretching surface through porous medium in the presence of heat generation," *Science Progress*, vol. 104, no. 3, p. 00368504211042261, 2021.

[17] P. Kumar, B. Nagaraja, F. Almeida, A. R. A.Kumar, Q. Al-Mdallal, and F. Jarad, "Magnetic dipole effects on unsteady flow of Casson-Williamson nanofluid propelled by stretching slippery curved melting sheet with buoyancy force," *Scientific Reports*, vol. 13, no. 1, p. 12770, 2023.

[18] N. Abbas, W. Shatanawi, K. Abodayeh, and T. A. Shatnawi, "Comparative analysis of unsteady flow of induced MHD radiative sutterby fluid flow at nonlinear stretching cylinder/sheet: Variable thermal conductivity," *Alexandria Engineering Journal*, vol. 72, pp. 451–461, 2023.

[19] A. A. Naseer, M. Safdar, S. Taj, M. U. Ali, A. Zafar, K. S. Kim, and J. H. Byun, "Analytical solutions for unsteady thin film flow with internal heating and radiation," *Journal of Mathematics*, vol. 2023, no. 1, p. 5612023, 2023.

[20] M. Diwate, J. V. Tawade, P. G. Janthe, M. Garayev, M. El-Meligy, N. Kulkarni, M. Gupta, and M. I. Khan, "Numerical solutions for unsteady laminar boundary layer flow and heat transfer over a horizontal sheet with radiation and nonuniform heat source/sink," *Journal of Radiation Research and Applied Sciences*, vol. 17, no. 4, p. 101196, 2024.

[21] T. Hayat, S. Amjad, Z. Nisar, and A. Alsaedi, "Thermal conductivity analysis for peristalsis of hybrid nanofluid with Darcy–Forchheimer law," *The European Physical Journal Plus*, vol. 139, no. 2, p. 140, 2024.

[22] M. I. Afridi, M. S. Khan, M. Qasim, and A. J. Chamkha, "Computational analysis of unsteady oscillatory flow of nanofluid with variable electric conductivity: gear-generalized differential quadrature approach," *Journal of Computational Design and Engineering*, vol. 11, no. 6, pp. 20–35, 2024.

[23] S. Dero, H. Shaikh, G. H. Talpur, I. Khan, S. O. Alharbim, and M. Andualem, "Influence of a Darcy-Forchheimer porous medium on the flow of a radiative magnetized rotating hybrid nanofluid over a shrinking surface," *Scientific Reports*, vol. 11, no. 1, p. 24257, 2021.

[24] H. A. Nabwey, T. Armaghani, B. Azizimehr, A. M. Rashad, and A. J. Chamkha, "A comprehensive review of nanofluid heat transfer in porous media," *Nanomaterials*, vol. 13, no. 5, p. 937, 2023.

[25] F. Mebarek-Oudina, I. Chabani, H. Vaidya, and A. A. I. Ismail, "Hybrid-nanofluid magneto-convective flow and porous media contribution to entropy generation," *International Journal of Numerical Methods for Heat & Fluid Flow*, vol. 34, no. 2, pp. 809–836, 2024.

[26] B. Venkateswarlu, S. Chavan, S. W. Joo, and S. C. Kim, "Irreversibility analysis of radiative $TiO_2 + Al_2O_3 + Cu/H_2O$ ternary nanofluid flow over a bidirectional stretching sheet with Cattaneo-Christov heat flux: Nanotechnology Applications," *Physica Scripta*, vol. 99, no. 11, p. 115264, 2024.

[27] S. Harsha, C. Shekara, and H. Kumar, "Stability analysis of the mixed convective flow of Jeffrey nanofluid through a porous medium," *Journal of Thermal Engineering*, vol. 11, no. 2, pp. 448–463, 2021.

[28] M. Khazayinejad, M. Hafezi, and B. Dabir, "Peristaltic transport of biological graphene-blood nanofluid considering inclined magnetic field and thermal radiation in a porous media," *Powder Technology*, vol. 384, pp. 452–465, 2021.

[29] N. Sarwar, M. I. Asjad, S. Hussain, M. N. Alam, and M. Inc, "Inclined magnetic field and variable viscosity effects on bioconvection of Casson nanofluid slip flow over non linearly stretching sheet," *Propulsion and Power Research*, vol. 11, no. 4, pp. 565–574, 2022.

[30] M. Arshad, F. M. Alharbi, A. Hassan, Q. Haider, A. Alhushaybari, S. M. Eldin, Z. Ahmad, L. A. Al-Essa, and A. M. Galal, "Effect of inclined magnetic field on radiative heat and mass transfer in chemically reactive hybrid nanofluid flow due to dual stretching," *Scientific Reports*, vol. 13, no. 1, p. 7828, 2023.

[31] Y. Elmhedy, A. Abd-Alla, S. Abo-Dahab, F. Alharbi, and M. Abdelhafez, "Influence of inclined magnetic field and heat transfer on the peristaltic flow of Rabinowitsch fluid model in an inclined channel," *Scientific Reports*, vol. 14, no. 1, p. 4735, 2024.

[32] G. A. Adem and A. G. Chanie, "Inclined magnetic field on mixed convection Darcy-Forchheimer Maxwell nanofluid flow over a permeable stretching sheet with variable thermal conductivity: The numerical approach," *Journal of Applied Mathematics*, vol. 2024, no. 1, p. 6750201, 2024.

[33] S. Zafar, A. Alfaleh, A. Zaib, F. Ali, M. Faizan, A. M. Abed, S. Elattar, and M. I. Khan, "Simulation of Prandtl nanofluid in the mixed convective flow of activation energy with gyrotactic microorganisms: numerical outlook features of micro-machines," *Micromachines*, vol. 14, no. 3, p. 559, 2023.

[34] Z. Ullah, M. M. Alam, A. A. Khan, A. Malik, S. Alkarni, Q. Khan, and F. E. Merga, "Thermally and chemically reactive boundary layer flow past a wedge moving in a nanofluid with activation energy and thermophoretic diffusion effects," *AIP Advances*, vol. 14, no. 10, 2024.

[35] K. Vijayalakshmi, A. Chandulal, H. Alhazmi, A. Aljohani, and I. Khan, "Effect of chemical reaction and activation energy on Riga plate embedded in a permeable medium over a Maxwell fluid flow," *Case Studies in Thermal Engineering*, vol. 59, p. 104457, 2024.

[36] K. M. Nihaal, U. S. Mahabaleshwar, N. Swaminathan, D. Laroze, and I. V. Shevchuk, "A numerical investigation of activation energy impact on MHD water-based $Fe_3\ O_4$ and $CO\ Fe_2\ O_4$ flow between the rotating cone and expanding disc," *Mathematics*, vol. 12, no. 16, p. 2530, 2024.

[37] C. A. Reddy, T. Thumma, J. S. Goud, and S. Panda, "Thermal and sensitivity analysis on hydromagnetic $CuO - Ag - H_2O$ nanofluid radiative flow over an elongating convective thermal surface: RSM-CCD Model," *Journal of Thermal Analysis and Calorimetry*, vol. 148, no. 21, pp. 12195–12210, 2023.